

WAVENUMBER FILTERING BY MECHANICAL STRUCTURES

by

Nathan Clay Martin II

B.E.E., General Motors Institute  
(1969)

S.M., Massachusetts Institute of Technology  
(1969)

Submitted in partial fulfillment  
of the requirements for the  
degree of

*Sc.D.*  
(Doctor of Philosophy)

at the

Massachusetts Institute of Technology

January, 1976

Signature of Author .....  
Department of Mechanical Engineering, Jan. 15, 1976

Certified by .....  
Thesis Supervisor

Accepted by .....  
Chairman, Department Committee on Graduate Students



WAVENUMBER FILTERING BY MECHANICAL STRUCTURES

by

Nathan C. Martin II

Submitted to the Department of Mechanical Engineering on January 15, 1976 in partial fulfillment of the requirements for the Degree of Doctor of Philosophy.

ABSTRACT

The response of membranes and plates to a random pressure field is interpreted to reveal the inherent wavenumber filtering characteristics of such structures. These spatial filtering characteristics are described by defining wavenumber filter shape functions which are obtained from spatial transforms of the normal mode shapes. Numerical calculations of the wavenumber filter shapes  $|A_m(k)|^2$  of typical beam modes are presented for a variety of boundary conditions. Detailed measurements of selected mode shapes were made for a rectangular membrane and two rectangular plates with different edge conditions. This mode shape data was then transformed numerically to obtain typical wavenumber filter shapes for the structures. These measured wavenumber filter shapes compare favorably with theoretical predictions; however, the presence of small amounts of non-resonant response in the measured mode shapes obscures the true high wavenumber behavior of the resulting wavenumber filter shapes.

These spatial filtering concepts were applied to the measurement of the low wavenumber components of wall pressure fluctuations under a turbulent boundary layer. The resonance characteristics of the membrane and plates were determined experimentally, and structural response measurements were made with the structures mounted in a test section wall of a low turbulence subsonic wind tunnel. Special quieting measures were taken to reduce acoustic contamination of the data. Estimates of both acoustic and convective ridge contamination were made and used to correct the data. Data was obtained for momentum thickness Reynolds number from 5000 to 11,000 for a smooth wall at zero pressure gradient. In the non-dimensional wavenumber-frequency range described by  $k_3\delta^* \approx 0$ ,  $0.18 < k_1\delta^* < .88$  and  $0.8 < \omega\delta^*/U_\infty < 5.1$ , typical low wavenumber spectrum levels were about 36 dB below convective ridge levels at the same reduced frequency. The data levels are shown to be about 10 dB higher than measurements obtained by Jameson; however, both sets of data do exhibit a similar dependence on  $\omega\delta^*/U_\infty$ .

Thesis Supervisor: Patrick Leehey

Title: Professor of Applied Mechanics

ACKNOWLEDGEMENTS

Many individuals have made significant contributions to this thesis effort and deserve a special word of appreciation. By no means the least of this group are the author's wife, Carol, and children, Mark, Mona, and Matthew. Their sacrifice and patience during the last three years has made this work possible.

The guidance and technical insights provided by Professor Patrick Leehey have been of invaluable assistance in the course of this research and are deeply appreciated. The author also wishes to thank the members of the Acoustics and Vibrations Laboratory for their cooperation and helpful discussions during the course of this research program. A special vote of thanks in this regard is extended to Dr. James A. Moore.

Another special word of appreciation is due to Miss Cheryl Gibson for her efficient typing of this thesis to meet a difficult time deadline. The financial support for much of this work was provided by the Sensor Technology Program, Office of Naval Research.

TABLE OF CONTENTS

	<u>Page</u>
ABSTRACT	2
LIST OF SYMBOLS	12
1. INTRODUCTION	16
2. ANALYSIS OF THE WAVENUMBER FILTERING BEHAVIOR OF MECHANICAL STRUCTURES	21
2.1 Response of Membranes and Plates to a Random Pressure Field	21
2.2 The Wavenumber Filter Shape	30
3. WAVENUMBER FILTER SHAPES FOR SOME IDEALIZED STRUCTURES	34
3.1 Analytical Evaluation of Wavenumber Filter Shapes	34
3.2 Analytical Evaluation of High Wavenumber Behavior	38
3.3 Numerical Evaluation of Wavenumber Filter Shapes	40
3.4 $ \bar{A}_m(\bar{k}) ^2$ for Beams With Various Boundary Conditions	43
3.5 Summary	47
4. EXPERIMENTAL METHODS FOR WAVENUMBER FILTER SHAPE DETERMINATION	48
4.1 Equipment and Procedures for Mode Shape Measurement	48
4.2 Membrane and Plate Construction	52
4.3 Measured Mode Shapes of Membranes and Plates	56

	<u>Page</u>
4.4 Wavenumber Filter Shapes from Measured Mode Shapes	59
5. THE APPLICATION OF SPATIAL FILTERING TO TURBULENT BOUNDARY LAYER WALL PRESSURE MEASUREMENT	68
5.1 The Experimental Sources of Excitation	68
5.2 Structural Response to Low Wavenumber Excitation	70
5.3 Structural Response to Acoustic Excitation	72
5.4 Structural Response to Convective Excitation	75
6. THE EXPERIMENTAL PROGRAM FOR LOW WAVENUMBER MEASUREMENTS	82
6.1 Determination of Resonance Characteristics	82
6.2 The Wind Tunnel Facility	86
6.3 The Structural Response Measurements	87
7. EVALUATION OF LOW WAVENUMBER DATA	93
7.1 Comparison with the Estimated Acoustic Response	93
7.2 Comparison with the Estimated Convective Response	97
7.3 The Measured Low Wavenumber Levels of $P(k_1, 0, \omega)$	99
7.4 Analysis of the Low Wavenumber Behavior of $P(k_1, 0, \omega)$	101
7.5 Comparison with Previous Measurements	105
8. CONCLUSIONS AND RECOMMENDATIONS	108
8.1 Conclusions Regarding Wavenumber Filtering	108
8.2 Conclusions Regarding Low Wavenumber Measurements	110

	<u>Page</u>
8.3 Guidelines for the Design of Wavenumber Filters	112
TABLES	115
FIGURES	127
REFERENCES	179
APPENDICES	181
A. Mode Shapes and Eigenvalues for Beams with Various Boundary Conditions	181
B. Convective Ridge Model of the Wavenumber- Frequency Spectrum of Wall Pressure	184

LIST OF TABLES

Table Number

4.1	Characteristics of the Measured Mode Shapes
4.2	Major Lobe Characteristics of $ \bar{A}_m(\bar{k}) ^2$
6.1	Experimentally Determined Characteristics of the Standard Membrane
6.2	Experimentally Determined Characteristics of the Modified Membrane
6.3	Experimentally Determined Characteristics of the Plates
6.4	Mean Properties of the Boundary Layers
6.5	Measured Membrane Displacement Levels
6.6	Measured Plate Acceleration Levels
7.1	Measured and Calculated Sensitivity to Acoustic Excitation
7.2	Measured Low Wavenumber Levels of $P(k_1, 0, \omega)$ from Standard Membrane Data
7.3	Measured Low Wavenumber Levels of $P(k_1, 0, \omega)$ from Modified Membrane Data
7.4	Measured Low Wavenumber Levels of $P(k_1, 0, \omega)$ from Plate Data

LIST OF FIGURES

Figure No.

- 2.1 Geometrical Considerations for Rectangular Structures
- 3.1 Wavenumber Filter Shapes for Sinusoidal Mode Shapes
- 3.2 Wavenumber Filter Shape for a Clamped Beam ( $m=9$ )
- 3.3 Wavenumber Filter Shape for a Free-Free Beam ( $m=5$ )
- 3.4 Wavenumber Filter Shape for a Clamped-Free Beam ( $m=5$ )
- 3.5 Wavenumber Filter Shape for a Simply Supported Beam ( $m=5$ )
- 3.6 Wavenumber Filter Shape for a Clamped-Simple Beam ( $m=5$ )
- 3.7 Wavenumber Filter Shape for a Clamped Beam ( $m=5$ )
- 3.8 A Comparison of the Decay of Side Lobe Peak Levels for Beams with Various End Supports ( $m=5$ )
- 4.1 Experimental Setup for Mode Shape Measurements
- 4.2 Apparatus for Mode Shape Measurements
- 4.3 Small Area Acoustic Drive
- 4.4 Membrane Construction Details
- 4.5 Detailed Membrane Mode Shapes Near the Boundaries
- 4.6 Plate Construction Details
- 4.7 Detailed Plate Mode Shapes Near the Boundaries



Figure No.

- 4.8 Measured Mode Shape: (11,1) Mode of Standard Membrane
- 4.9 Measured Mode Shape: (9,1) Mode of Modified Membrane
- 4.10 Measured Mode Shape: (15,1) Mode of Modified Membrane
- 4.11 Measured Mode Shape: (9,1) Mode of Clamped Plate
- 4.12 Measured Mode Shape: (15,1) Mode of Clamped Plate
- 4.13 Measured Mode Shape: (9,1) Mode of S-C-S-C Plate
- 4.14 Measured Mode Shape: (15,1) Mode of S-C-S-C Plate
- 4.15 Measured  $|\bar{A}_m(\bar{k})|^2$ : (11,1) Mode of Standard Membrane
- 4.16 Measured  $|\bar{A}_m(\bar{k})|^2$ : (9,1) Mode of Modified Membrane
- 4.17 Measured  $|\bar{A}_m(\bar{k})|^2$ : (15,1) Mode of Modified Membrane
- 4.18 Measured  $|\bar{A}_m(\bar{k})|^2$ : (9,1) Mode of Clamped Plate
- 4.19 Measured  $|\bar{A}_m(\bar{k})|^2$ : (15,1) Mode of Clamped Plate
- 4.20 Measured  $|\bar{A}_m(\bar{k})|^2$ : (9,1) Mode of S-C-S-C Plate
- 4.21 Measured  $|\bar{A}_m(\bar{k})|^2$ : (15,1) Mode of S-C-S-C Plate
- 5.1 Wavenumber-Frequency Location of Various Excitations

Figure No.

- 5.2 The Normal Distribution Model of the Convective Spectrum
- 5.3 Geometrical Considerations for Acoustic Response Estimates
- 6.1 Membrane Wave Speed Data, Standard Membrane
- 6.2 Experimental Set-up for Decay Rate Measurements and Typical rms Decay Record
- 6.3 The M.I.T. Low-Noise, Low-Turbulence Wind Tunnel
- 6.4 The Test Section Configuration
- 6.5 Typical Mean Velocity Profile:  $U_{\infty} = 29$  m/sec
- 6.6 The Law of the Wall:  $U_{\infty} = 29$  m/sec
- 6.7 Standard Membrane Displacement Spectrum:  
 $U_{\infty} = 40$  m/sec
- 6.8 Modified Membrane Displacement Spectrum:  
 $U_{\infty} = 40$  m/sec
- 6.9 Clamped Plate Acceleration Spectrum:  
 $U_{\infty} = 40$  m/sec
- 6.10 S-C-S-C Plate Acceleration Spectrum:  
 $U_{\infty} = 40$  m/sec
- 7.1 Typical Acoustic Background Spectrum:  
 $U_{\infty} = 40$  m/sec
- 7.2 Comparison of Measured Membrane Response with Predicted Acoustic and Convective Responses
- 7.3 Comparison of Measured Clamped Plate Response with Predicted Acoustic and Convective Responses

Figure No.

- 7.4 Wall Pressure Spectra
- 7.5 Location of Low Wavenumber Data in Wavenumber Frequency Space
- 7.6 Contours of  $10 \log \{ \Phi_p(k_1, 0, \omega) / (q^2 \delta^{*3} / U_\infty) \}$  Obtained by Transforming Blake's Data
- 7.7 Comparison of Convective and Measured Low Wavenumber Levels of  $\Phi_p(k_1, 0, \omega)$ .
- 7.8 Comparison of the Measured Low Wavenumber Spectra with Jameson's Data

LIST OF SYMBOLS

$A_m(k_1)$	Longitudinal (streamwise) shape factor	} for the (m,n) mode
$A_n(k_3)$	Lateral shape factor	
$\bar{A}_m(\bar{k})$	Non-dimensional shape factor, $\bar{A}_m(\bar{k}) = A_m(k)/[L]^{1/2}$	
$ A_m(k_1) ^2$	Longitudinal (streamwise) wavenumber filter shape function	
$ A_n(k_3) ^2$	Lateral wavenumber filter shape function	
$ \bar{A}_m(\bar{k}) ^2$	Non-dimensional wavenumber filter shape function	
$a_{mn}(\omega)$	Modal response amplitude, (m,n) mode	
$c$	In vacuo membrane wavespeed, $c = [T/\sigma]^{1/2}$	
$c_{mn}$	Effective membrane wavespeed	
$c_o$	Velocity of sound in air	
$C_m$	Mode shape normalizing constant	
$D$	Flexural rigidity	
$E[X, Y]$	Joint mathematical expectation of the random variables X and Y	
$f_{mn}(x, z)$	Two-dimensional normal mode shape, (m,n) mode	
$f_{mn}$	Natural frequency (hz) of (m,n) mode	
$\Delta f_{mn}$	Equivalent rectangular bandwidth (hz) of the (m,n) mode	
$ F_{mn}(k_1, k_3) ^2$	Two-dimensional wavenumber filter shape function	
$f_N$	Nyquist frequency, $f_N = 1/2\Delta t$	
$g_m(x)$	Longitudinal mode shape	
$G_m(\bar{x})$	Non-dimensional longitudinal mode shape, $G_m(\bar{x}) = [L]^{1/2} g_m(x)$	

$h_n(\underline{z})$	Lateral mode shape
H	Boundary layer shape factor, $H = \delta^*/\theta$
$H_{mn}(\omega)$	Frequency response of (m,n) mode
$I_m(\bar{k})$	Imaginary part of $\bar{A}_m(\bar{k})$
$k =  \vec{K} $	Wavenumber: $k_1$ , longitudinal; $k_3$ , lateral
$k_A$	Acoustic wavenumber, $k_A = \omega/c_0$
$k_C$	Convective wavenumber, $k_C = \omega/U_C$
$k_T$	Trace wavenumber
$\bar{k}$	Non-dimensional wavenumber, $\bar{k} = kL$
$\bar{k}_m$	Characteristic wavenumber of $ \bar{A}_m(\bar{k}) ^2$
$\bar{k}_N$	Nyquist wavenumber, $\bar{k}_N = N\pi$
$k^*$	Non-dimensional wavenumber, $k^* = k\delta^*$
$\Delta\bar{k}_e$	Equivalent rectangular wavenumber bandwidth of $ \bar{A}_m(\bar{k}) ^2$
L	Structural dimension: $L_1$ , longitudinal; $L_3$ , lateral
$L_p$	Level in dB of $10 \log \{P(k_1, 0, \omega) / (q^2 \delta^{*3} / U_\infty)\}$
N	Number of sample intervals
$p(x, z, t)$	Instantaneous wall pressure fluctuation at position (x,z) and time t
$P_{mn}(\omega)$	Modal pressure, (m,n) mode
$P(k_1, k_3, \omega)$	Measured wavenumber-frequency spectral density of wall pressure
q	free stream dynamic head, $q = \rho U_\infty^2 / 2$
r	Measurement separation distance $r_1$ , longitudinal (streamwise); $r_3$ , lateral

R	Notch ratio for S-C-S-C plate
$R_a(\omega)$	Acoustic sensitivity of acceleration response
$R_w(\omega)$	Acoustic sensitivity of displacement response
$R_m(\bar{k})$	Real part of $\bar{A}_m(\bar{k})$
$S_w(x, z, \omega)$	Theoretical displacement spectral density, $-\infty < \omega < \infty$
$\hat{S}_w(x, z, f)$	Experimental displacement spectral density, $0 < f < \infty$ $\hat{S}_w(x, z, f) = 4\pi S_w(x, z, \omega)$
$S_a(x, z, \omega)$	Theoretical acceleration spectral density, $-\infty < \omega < \infty$
$\hat{S}_a(x, z, f)$	Experimental acceleration spectral density, $0 < f < \infty$
T	Uniform membrane tension
$U_c$	Convection velocity
$U_\tau$	Friction velocity
$U_\infty$	Free stream velocity
$w(x, z, t)$	Instantaneous structural displacement at position (x,z)
x	Longitudinal (streamwise) distance variable
$\bar{x}$	Non-dimensional distance variable, $\bar{x} = x/L$
z	Lateral distance
$\alpha$	Velocity ratio, $\alpha = U_c/U_\infty$
$\beta_{mn}$	Modal bandwidth of (m,n) mode
$\delta^*$	Boundary layer displacement thickness
$\eta$	Damping loss factor, equivalent to twice the fraction of critical damping
$\theta$	Boundary layer momentum thickness
$\kappa$	Non-dimensional wavenumber variable, $\kappa = (k_1/k_c) - 1$

$\lambda$	Wavelength, $\lambda = 2\pi/k$
$\rho$	Fluid density
$\sigma$	Structural surface density
$\sigma_{mn}$	Effective surface density of (m,n) mode
$\Phi_a(\omega)$	Theoretical spectral density of acoustic pressure fluctuations, $-\infty < \omega < \infty$
$\hat{\Phi}_a(f)$	Experimental spectral density of acoustic pressure fluctuations, $0 < f < \infty$ , $\hat{\Phi}_a(f) = 4\pi \Phi_a(\omega)$
$\Phi_p(\omega)$	Theoretical spectral density of wall pressure fluctuations, $-\infty < \omega < \infty$
$\Phi_p(k_1, k_3, \omega)$	Theoretical wavenumber-frequency spectral density of wall pressure, $-\infty < \omega, k_1, k_3 < \infty$
$\Phi_p(\vec{k}, \omega)$	
$\Phi_c(k_1, k_3, \omega)$	Convective model of $\Phi_p(k_1, k_3, \omega)$
$\Phi_p(r_1, r_3, \omega)$	Theoretical cross spectral density of wall pressure
$\omega$	Radian frequency
$\omega_{mn}$	Resonant frequency of (m,n) mode
$\omega^*$	Non-dimensional frequency, $\omega^* = \omega\delta^*/U_\infty$

## 1. INTRODUCTION

The primary impetus for investigating the wavenumber filtering characteristics of mechanical structures is the need to better understand the vibratory response of such structures to wall pressure fluctuations created by the turbulent boundary layer. Problems dealing with such turbulence induced vibrations are encountered both in high speed aircraft and marine applications. However, the main thrust of this research has been in areas more closely related to marine applications. Some of the more critical marine applications are those dealing with the vibratory response of sonar related structures. In many practical sonar applications there are operating ranges over which turbulent boundary layer wall pressure fluctuations are important contributors to system noise levels.

The need to make more reliable estimates of structural response has made it necessary to better understand the characteristics of the wall pressure fluctuations. This has led several investigators, including Blake [1] and Burton [2], working in the M.I.T. low turbulence wind tunnel, to measure wall pressure statistics for various wall conditions and pressure gradients. Such measurements have typically been made by using pairs of small flush-mounted pressure transducers and have adequately defined the dominant components of the wall pressure fluctuations. These dominant components are the pressure disturbances which are convected downstream at a major fraction of the free stream velocity.



However, in most marine applications the free stream velocity is low, and the frequencies of interest are often comparatively high. For such situations, the characteristic spatial scales ( $\lambda = U_c/f$ ) of the convecting pressure disturbances are much smaller than the corresponding wavelengths of free bending waves in typical marine structures. As a result, the convective excitation is very inefficient at producing a vibratory structural response. A more efficient excitation would be wall pressure fluctuations whose characteristic spatial scales were long enough to match the structural wavelengths. Thus, the need to more accurately predict and analyze structural response to turbulent boundary layer wall pressure fluctuations has led investigators to attempt to measure the low wavenumber (i.e.: long wavelength) components of the wall pressure fluctuations. Unfortunately, these low wavenumber components do not contribute significantly to total wall pressure spectra. Thus, the existing experimental data is inadequate for accurate determination of these low wavenumber components.

To overcome these difficulties it has been necessary to construct spatial (wavenumber) filters which respond well at low wavenumbers while rejecting convective components at higher wavenumbers. Several approaches have been utilized. Maidanik and Jorgensen [3] have shown that an array of flush-mounted pressure transducers could be used as a spatial filter. Blake and Chase [4] and then Jameson [5] used this approach to measure the low

wavenumber spectrum beneath a plane turbulent boundary layer. Other investigators have chosen to utilize the dynamic characteristics of continuous mechanical systems to obtain spatial filtering. Aupperle and Lambert [6] described analytically the wavenumber filtering action of beams, and they have also applied similar approaches to the prediction of acoustic radiation from plates excited by turbulence [7]. In a more recent experiment, Jameson [8] has used a rectangular plate with clamped edges as a wavenumber filter.

The measurement of these low wavenumber wall pressure components is a very difficult task. The spectral levels of these components are so low that the possibility of contamination of the data by acoustic or convective ridge excitation must always be carefully evaluated. Such evaluations require a knowledge of the way in which the structure responds to excitations at different wavenumbers (i.e.: the wavenumber filtering characteristics of the structure). It is certainly possible to estimate analytically the response of the structure to high and low wavenumbers. Chase [9] has discussed appropriate techniques as applied to transducer response, and Jameson [8] estimated the convective response of his clamped plate.

Such analytic estimates are certainly useful; however, for the experimental situation it is equally important to verify

that the physical structures utilized in the experiment perform in a manner consistent with the analysis. Thus, one of the major objectives of this research program has been to determine experimentally the wavenumber filtering characteristics of real mechanical structures. These same structures are then used to measure the low wavenumber wall pressure spectrum beneath a plane turbulent boundary layer.

The presentation of the research divides itself naturally into two major parts. Chapters two, three and four deal in detail with the wavenumber filtering behavior of mechanical systems. The concept of the wavenumber filter shape,  $|A_m(k)|^2$ , is shown to come from a normal mode analysis of structural response to random pressure excitations. Both analytical and numerical techniques for evaluating  $|A_m(k)|^2$  are discussed and results are presented for several ideal structures. The utility of  $|A_m(k)|^2$  in predicting structural response to acoustic, convective, and low wavenumber excitations is also demonstrated. Finally, experimental techniques for measuring  $|A_m(k)|^2$  via mode shape measurements are discussed and typical results are presented.

Chapter five, six and seven represent the application of these spatial filtering characteristics to the measurement of the low wavenumber components of the turbulent boundary layer wall pressure fluctuations. The nature of the experimental program is

outlined, and the low wavenumber results are discussed. Estimates of acoustic and convective response levels are made based on the results of the first phase of the research.

## 2. ANALYSIS OF THE WAVENUMBER FILTERING BEHAVIOR OF MECHANICAL STRUCTURES

The objective of this discussion is to present several analytic results which are helpful in understanding the wavenumber filtering behavior of typical mechanical structures. Much of the discussion deals with the wavenumber filter shape function,  $|A_m(k)|^2$ . From a modal analysis of structural response to random pressure excitation, it will be shown that  $|A_m(k)|^2$  describes the spatial filtering characteristics of the structural modes just as the frequency response function  $|H(\omega)|^2$  describes the frequency filtering characteristics. Several analytical techniques will be used to explore the behavior of  $|A_m(k)|^2$  in various wavenumber domains.

### 2.1 Response of Membranes or Plates to a Random Pressure Field

This analysis considers the response of two dimensional, rectangular structures (plates and membranes) to excitation by a random pressure field. This pressure field is assumed to be stationary in time and homogeneous in space. The following assumption regarding the dynamics of the structures will also be used:

(1) Damping: The modal damping factor ( $\eta_{mn}$ ) used in the analysis represents the total damping of the structure. It thus includes radiation damping as well as structural damping. This total damping is assumed to be sufficiently small so that modal overlap is negligible.

(2) Fluid Loading: Modal coupling effects due to fluid loading are assumed to be negligible. However, the added mass effect of the fluid loading can easily be considered by including the modal added mass in the total modal mass density. In the experiments considered later this correction is significant only for the membrane.

The geometric configurations of the membrane and plate structures are shown in Figure 2.1. Both structures are characterized by dimensions  $L_1$  and  $L_3$  as well as a uniform mass per unit area  $\sigma$ . In addition the membrane is characterized by a uniform tensile force per unit length  $T$ , and the plate is characterized by its flexural rigidity  $D$ . The transverse displacement  $w(x,z,t)$  represents the response of the structure when excited by a normal random pressure field  $p(x,z,t)$  and subjected to a uniform damping force per unit mass  $\beta \partial w / \partial t$ . The governing dynamic equation is

$$\frac{\partial^2 w}{\partial t^2} + \beta \frac{\partial w}{\partial t} + \frac{1}{\sigma} \Lambda w(x,z,t) = \frac{1}{\sigma} p(x,z,t) \quad (2.1)$$

where  $\Lambda$  is a linear differential operator in the spatial variables such that  $\Lambda w(x,z,t) = -T \nabla^2 w(x,z,t)$  for membranes, (2.2)

and  $\Lambda w(x,z,t) = D \nabla^4 w(x,z,t)$  for plates. (2.3)

Since  $p(x,z,t)$  is considered to be a random process with zero mean which is both time stationary and homogeneous in space,

its Fourier transform  $p(x, z, \omega)$  is a random process defined by the quadratic mean integral,

$$p(x, z, t) = \int_{-\infty}^{\infty} p(x, z, \omega) e^{i\omega t} d\omega.$$

Similarly,  $w(x, z, t) = \int_{-\infty}^{\infty} w(x, z, \omega) e^{i\omega t} d\omega.$

Thus in the frequency domain, the membrane version of equation (2.1) becomes

$$\{\nabla^2 + k^2\} w(x, z, \omega) = \frac{1}{\sigma c} p(x, z, \omega), \quad (2.4)$$

where  $c = [T/\sigma]^{1/2}$  is the membrane wave speed, and  $k$  is defined for complex  $\omega$  by

$$k = \frac{1}{c} [\omega^2 - i\beta\omega]^{1/2}, \quad (k \rightarrow \frac{|\omega|}{c} \text{ as } |\omega| \rightarrow \infty)$$

with a branch cut for  $\text{Re}(\omega) = 0, 0 < \text{Im}(\omega) < \beta$ . Similarly the plate version of equation (2.1) now becomes

$$\{\nabla^4 - k^4\} w(x, z, \omega) = -\frac{1}{D} p(x, z, \omega), \quad (2.5)$$

where  $k$  is defined for complex  $\omega$  by

$$k = \sqrt{\frac{\sigma}{D}} [\omega^2 - i\beta\omega]^{1/4}, \quad (k \rightarrow \sqrt{\frac{|\omega|\sigma}{D}} \text{ as } |\omega| \rightarrow \infty),$$

with a branch cut for  $\text{Re}(\omega) = 0, 0 < \text{Im}(\omega) < \beta$ .

For the undamped free vibration of such a structure there exists a set of normal modes  $f_{mn}(x, z)$  and eigenvalues  $\omega_{mn}$  which

together satisfy the boundary conditions and the equation

$$\{\Lambda - \sigma\omega_{mn}^2\} f_{mn}(x,z) = 0 \quad (2.6)$$

An appropriate normalization for the orthogonal functions  $f_{mn}(x,z)$  is to require

$$\int_0^{L_1} \int_0^{L_3} f_{mn}(x,z) f_{jk}(x,z) dx dz = \delta_{mj} \delta_{nk}, \quad (2.7)$$

where  $\delta_{mj}$  is the Kronecker Delta Function. For example, the solution of this eigenvalue problem for the membrane with zero displacement at the boundaries yields

$$f_{mn}(x,z) = 2[L_1 L_3]^{-1/2} \sin \frac{m\pi x}{L_1} \sin \frac{n\pi z}{L_3}, \quad (2.8)$$

$$\omega_{mn}^2 = \frac{T}{\sigma} \left[ \left( \frac{m\pi}{L_1} \right)^2 + \left( \frac{n\pi}{L_3} \right)^2 \right]. \quad (2.9)$$

For the situation of small damping and negligible modal coupling it is reasonable to express the solution to equation (2.4) or (2.5) as an infinite sum of these same normal modes. Thus,

$$w(x,z,\omega) = \sum_{m=1}^{\infty} \sum_{n=1}^{\infty} a_{mn}(\omega) f_{mn}(x,z) \quad (2.10)$$

When equation (2.10) is substituted into equation (2.4) and (2.5), the orthogonality of the normal modes can be used to yield

$$a_{mn}(\omega) = \frac{1}{\sigma[\omega^2 - \omega_{mn}^2 - i\beta\omega]} P_{mn}(\omega), \quad (2.11)$$

where the modal pressure  $P_{mn}(\omega)$  is defined by



$$P_{mn}(\omega) = \int_0^{L_1} \int_0^{L_3} p(x, z, \omega) f_{mn}(x, z) dx dz. \quad (2.12)$$

Equation (2.10) and (2.12) can now be combined to give

$$w(x, z, \omega) = \sum_{m=1}^{\infty} \sum_{n=1}^{\infty} \frac{1}{\sigma[\omega^2 - \omega_{mn}^2 - i\beta\omega]} P_{mn}(\omega) f_{mn}(x, z). \quad (2.13)$$

This displacement response spectral density can therefore be determined from

$$\begin{aligned} S_w(x, z, \omega) &= E[w(x, z, \omega)w^*(x, z, \omega)] (d\omega) \\ &= \sum_{j,k=1}^{\infty} \sum_{m,n=1}^{\infty} \frac{f_{jk}(x, z) f_{mn}(x, z)}{\sigma^2(\omega^2 - \omega_{jk}^2 - i\beta\omega)(\omega^2 - \omega_{mn}^2 + i\beta\omega)} E[P_{jk}(\omega)P_{mn}^*(\omega)] (d\omega), \end{aligned} \quad (2.14)$$

where  $E[ \ ]$  denotes an expectation and  $P_{mn}^*$  denotes the complex conjugate of  $P_{mn}$ .

The notation of equation (2.14) results from considerations of the definition and existence of spectral representations of random processes. For example, Cramer and Leadbetter [20] have shown that for a stationary random process  $\xi(t)$ , a spectral representation of the form

$$\xi(t) = \int_{-\infty}^{\infty} e^{it\omega} d\zeta(\omega)$$

exists in the quadratic mean sense. Also the process  $\xi(t)$  has a spectral distribution function  $F(\omega)$  and a spectral density  $f(\omega)$  related by

$$F(\omega) = E[|\zeta(\omega)|^2],$$

and

$$dF(\omega) = f(\omega)d\omega = E[|d\zeta(\omega)|^2].$$

It is assumed that a similar generalized density function for  $d\zeta(\omega)$  exists for infinitesimal  $d\omega$ , in which case  $d\zeta(\omega) = g(\omega)d\omega$  so that

$$f(\omega) = E[|g(\omega)|^2] (d\omega).$$

The modal pressure term in equation (2.14) depends upon the degree of spatial matching between the pressure field and the normal modes of the structure. To more clearly reveal this effect, equation (2.12) is used to obtain

$$\begin{aligned} & E[P_{jk}(\omega)P_{mn}^*(\omega)] (d\omega) = \\ & = \int_0^{L_1} \int_0^{L_3} f_{jk}(x_1, z_1) \int_0^{L_1} \int_0^{L_3} f_{mn}(x_2, z_2) E[\rho(x_1, z_1, \omega)\rho^*(x_2, z_2, \omega)] (d\omega) dx_1 dz_1 dx_2 dz_2. \end{aligned} \quad (2.15)$$

Since the pressure field is assumed to be homogeneous in space,

$$E[p(x_1, z_1, \omega)p^*(x_2, z_2, \omega)] (d\omega) = \Phi_p(r_1, r_3, \omega)$$

where  $r_1 = x_1 - x_2$  and  $r_3 = z_1 - z_2$ .

The cross-spectral density of the wall pressure  $\Phi_p(r_1, r_3, \omega)$  is the Fourier transform of the wavenumber-frequency spectrum  $\Phi_p(k_1, k_3, \omega)$ .

That is,

$$\Phi_p(r_1, r_3, \omega) = \int_{-\infty}^{\infty} \int_{-\infty}^{\infty} \Phi_p(k_1, k_3, \omega) e^{-i(k_1 r_1 + k_3 r_3)} dk_1 dk_3. \quad (2.16)$$

Thus equation (2.15) can be expressed as

$$E[P_{jk}(\omega)P_{mn}^*(\omega)](d\omega) = \iint_{-\infty}^{\infty} F_{mn}(k_1, k_3) F_{jk}^*(k_1, k_3) \Phi_p(k_1, k_3, \omega) dk_1 dk_3, \quad (2.17)$$

where  $F_{mn}(k_1, k_3)$  is a two-dimensional spatial transform of the normal mode shape and is defined by

$$F_{mn}(k_1, k_3) = \int_0^{L_1} \int_0^{L_3} f_{mn}(x, z) e^{i(k_1 x + k_3 z)} dx dz. \quad (2.18)$$

Equation (2.17) can now be used in equation (2.14) to yield

$$S_w(x, z, \omega) = \sum_{j,k=1}^{\infty} \sum_{m,n=1}^{\infty} \frac{f_{jk}(x, z) f_{mn}(x, z)}{\sigma^2 [\omega^2 - \omega_{jk}^2 - i\beta\omega] [\omega^2 - \omega_{mn}^2 + i\beta\omega]} \times \iint_{-\infty}^{\infty} F_{mn}(k_1, k_3) F_{jk}^*(k_1, k_3) \Phi_p(k_1, k_3, \omega) dk_1 dk_3. \quad (2.19)$$

Equation (2.19) includes the effects of modal coupling as well as the direct modal responses. In a significant number of practical applications it is possible to neglect the modal coupling terms. For example, Dyer's criterion [10] suggests that the coupling terms can be neglected if the correlation lengths of the pressure field are significantly less than the corresponding dimensions of the structure. This situation implies that  $\Phi_p(k_1, k_3, \omega)$  is approximately

constant in  $k_1$  and  $k_3$ , and therefore the  $k_1$  and  $k_3$  integrals in equation (2.19) vanish due to the orthogonality of the mode shapes unless  $(j,k) = (m,n)$ . Even when Dyer's criterion is not applicable, it is often possible to neglect the modal coupling terms if we restrict our consideration to resonant response. In this case, the requirement is that the damping must be sufficiently small so that modal overlap is negligible. When this is true, the frequency dependent terms in equation (2.19) render the coupling terms negligible.

It is perhaps of interest to note that in the turbulent boundary layer experiments described later in this thesis both the membranes and plates are long thin structures. As a result, Dyer's criterion can only strictly be applied to the  $k_1$  integration. However, the experimental work is concerned only with measurements at resonance, and the modal spacing is sufficiently greater than the modal bandwidth so that modal overlap is negligible. Thus it is appropriate to ignore coupling terms and express the displacement spectral response as

$$S_w(x,z,\omega) = \sum_{m=1}^{\infty} \sum_{n=1}^{\infty} \frac{f_{mn}^2(x,z)}{\sigma^2 [(\omega^2 - \omega_{mn}^2)^2 + (\beta\omega)^2]} \iint_{-\infty}^{\infty} |F_{mn}(k_1, k_3)|^2 \phi_p(k_1, k_3, \omega) dk_1 dk_3. \quad (2.20)$$

It should be noted that the frequency dependent portion of this equation is just the modal frequency response  $|H_{mn}(\omega)|^2$ . That is,

$$|H_{mn}(\omega)|^2 = \frac{1}{\sigma^2 [(\omega^2 - \omega_{mn}^2)^2 + (\beta\omega)^2]} \quad (2.21)$$

Equation (2.20) can be interpreted as the basic input-output relationship describing the response of a rectangular plate or membrane to a random pressure field. It indicates that the modal displacement response of the structure at a given point depends on the frequency response  $|H_{mn}(\omega)|^2$ , the degree of matching between the response point  $(x,z)$  and the mode shape  $f_{mn}(x,z)$ , and the spatial (wavenumber) matching between the pressure field and the 2-dimensional wavenumber filter shape  $|F_{mn}(k_1, k_3)|^2$ . The total response is then the sum of the individual modal responses. However, if only the resonant frequencies of the structure  $(\omega_{mn})$  are to be considered, then the resonant mode response dominates and equation (2.20) becomes

$$S_w(x, z, \omega_{mn}) = f_{mn}^2(x, z) |H_{mn}(\omega_{mn})|^2 \iint_{-\infty}^{\infty} |F_{mn}(k_1, k_3)|^2 \Phi_p(k_1, k_3, \omega_{mn}) dk_1 dk_3 \quad (2.22)$$

In an experimental sense equation (2.22) can be used to relate the pressure excitation to the vibratory response if the modal characteristics  $|H_{mn}(\omega_{mn})|^2$  and  $|F_{mn}(k_1, k_3)|^2$  can be determined accurately. Since at resonance

$$|H_{mn}(\omega_{mn})|^2 = \frac{1}{(\sigma\beta\omega_{mn})^2} = \frac{1}{(\sigma\eta\omega_{mn}^2)} \quad (2.23)$$

the evaluation of  $|H_{mn}(\omega_{mn})|^2$  requires only a determination of the total damping and surface density associated with the modes under consideration. One of the major goals of the thesis effort has been to explore analytical and experimental methods for evaluating the wavenumber filter shape  $|F_{mn}(k_1, k_3)|^2$ . The next discussion will explore the basic analytic behavior of this wavenumber filter shape function.

## 2.2 The Wavenumber Filter Shape

The two-dimensional wavenumber filter shape function  $|F_{mn}(k_1, k_3)|^2$  is the squared magnitude of the two-dimensional spatial transform of the normal mode shape as indicated in equation (2.17). This implies that  $|F_{mn}(k_1, k_3)|^2$  is a modal characteristic; that is, the exact variation of  $|F_{mn}(k_1, k_3)|^2$  in  $(k_1, k_3)$  should be somewhat different for each mode just as the mode shape is different for each mode. Also since the details of the mode shape  $f_{mn}(x, z)$  are dependent on the boundary conditions, it is reasonable to expect that the behavior of the wavenumber filter shape will also depend to some extent on the boundary conditions.

In many cases the normal mode shape  $f_{mn}(x, z)$  is easily separated into an x-dependent term and a z-dependent term. This is certainly true for the membrane mode shapes of equation (2.8). This separation of variables is also analytically exact for plates having any two opposite sides simply supported. Even for the case of the fully clamped plate, a separation of variables technique using

clamped beam functions is often used as a reasonable approximation to the mode shape since an exact solution is unobtainable in closed form [11]. To take advantage of this separation of variables, let

$$f_{mn}(x, z) = g_m(x)h_n(z). \quad (2.24)$$

Substitution of equation (2.24) into equation (2.18) yields

$$F_{mn}(k_1, k_3) = \int_0^{L_1} g_m(x) e^{ik_1 x} dx \int_0^{L_3} h_n(z) e^{ik_3 z} dz. \quad (2.25)$$

It is now convenient to define

$$A_m(k_1) = \int_0^{L_1} g_m(x) e^{ik_1 x} dx$$
$$A_n(k_3) = \int_0^{L_3} h_n(z) e^{ik_3 z} dz. \quad (2.26)$$

With these definitions the two-dimensional wavenumber filter shape  $|F_{mn}(k_1, k_3)|^2$  can be expressed in terms of one dimensional filter shapes as

$$|F_{mn}(k_1, k_3)|^2 = |A_m(k_1)|^2 |A_n(k_3)|^2. \quad (2.27)$$

For simplicity, the remaining analysis will focus on the behavior of the one dimensional wavenumber filter shape functions. Once the one dimensional filter shapes are determined, the two-dimensional behavior is given by equation (2.27).

Some basic insight into the behavior of the wavenumber filter shape  $|A_m(k)|^2$  can be obtained easily by making some analytic

observations based on the defining equations (2.26). For example, from equation (2.24) and the orthogonality relationship of equation (2.7) it is apparent that

$$\int_0^{L_1} g_m^2(x) dx = 1 \quad \text{and} \quad \int_0^{L_3} h_n^2(z) dz = 1 \quad (2.28)$$

If we now consider the integral,  $\int_{-\infty}^{\infty} |A_m(k)|^2 dk$ , we can apply

Parseval's formula for integrals to obtain

$$\int_{-\infty}^{\infty} |A_m(k)|^2 dk = 2\pi \int_0^{L_1} g_m^2(x) dx = 2\pi$$

Thus the total area under a curve of  $|A_m(k)|^2$  vs.  $k$  is the same for all modes. It also follows from equation (2.26) that  $|A_m(k)|^2 = |A_m(-k)|^2$ . Since the wavenumber filter shape is thus an even function of  $k$ ,

$$\int_0^{\infty} |A_m(k)|^2 dk = \pi. \quad (2.29)$$

At very low wavenumbers ( $k \rightarrow 0$ ) equation (2.26) can be expanded in powers of  $k$  to give

$$A_m(k) = \int_0^L g_m(x) dx + ik \int_0^L x g_m(x) dx - \frac{1}{2} k^2 \int_0^L x^2 g_m(x) dx + O(k^3). \quad (2.30)$$



This expansion indicates that the very low wavenumber behavior of  $|A_m(k)|^2$  is governed by the "average" or large scale behavior of the entire mode shape.

To determine the high wavenumber behavior ( $k \rightarrow \infty$ ) of  $|A_m(k)|^2$  we can apply the well known technique of repeated integration by parts to equation (2.26)

$$A_m(k) = \frac{1}{ik} \left[ g_m(x) e^{ikx} \right]_0^L - \frac{1}{(ik)^2} \left[ g'_m(x) e^{ikx} \right]_0^L + \frac{1}{(ik)^3} \left[ g''_m(x) e^{ikx} \right]_0^L + O \left( \frac{1}{[ik]^4} \right) \quad (2.31)$$

The implication of equation (2.31) is that the high wavenumber behavior of  $|A_m(k)|^2$  is governed by the lowest order derivative of the mode shape which is non-zero at the boundary. This is directly analogous to Chase's result [9] for the high wavenumber response of a rectangular pressure transducer.

### 3. WAVENUMBER FILTER SHAPES FOR SOME IDEALIZED STRUCTURES

In this chapter analytical and numerical approaches for evaluating the one-dimensional wavenumber filter shape  $|A_m(k)|^2$  are discussed. These techniques are then applied to the determination of  $|A_m(k)|^2$  for beams with various boundary conditions.

#### 3.1 Analytical Evaluation of Wavenumber Filter Shapes

When a closed form solution for the mode shape  $g_m(x)$  is known, it is possible to obtain the wavenumber filter shape  $|A_m(k)|^2$  by performing the integration of equation (2.26). The difficulty of such an approach naturally depends upon the complexity of the mode shape. It is helpful to nondimensionalize the spatial variables on the length of the structure so that

$$\bar{k} = kL \quad \text{and} \quad \bar{x} = x/L. \quad (3.1)$$

As a result of the mode shape normalization of equation (2.28), the one-dimensional mode shape  $g_m(x)$  has dimensions of  $[L]^{-1/2}$ , and its spatial transform  $A_m(k)$  therefore has dimensions of  $[L]^{1/2}$ . The corresponding non-dimensional mode shape  $G_m(\bar{x})$  and non-dimensional transform  $\bar{A}_m(\bar{k})$  are

$$G_m(\bar{x}) = [L]^{1/2} g_m(x) \quad \text{and} \quad \bar{A}_m(\bar{k}) = A_m(k)/[L]^{1/2}. \quad (3.2)$$

In terms of these non-dimensional variables, equation (2.26) becomes

$$\bar{A}_m(\bar{k}) = \int_0^1 G_m(\bar{x}) e^{i\bar{k}\bar{x}} d\bar{x}. \quad (3.3)$$

The definition of the non-dimensional wavenumber filter shape function  $|\bar{A}_m(\bar{k})|^2$  follows from equation (3.2) as

$$|\bar{A}_m(\bar{k})|^2 = |A_m(k)|^2/L. \quad (3.4)$$

Several different idealized structures have sinusoidal mode shapes of the form

$$G_m(\bar{x}) = 2 \sin \bar{k}_m \bar{x}, \quad 0 \leq \bar{x} \leq 1 \quad (3.5)$$

where  $\bar{k}_m = m\pi$ . This one-dimensional mode shape is valid for strings with fixed ends and for simply supported beams. It is also valid as the separable non-dimensional component of the mode shape for membranes and simply supported plates. The integral obtained by substituting equation (3.5) into equation (3.3) is well known and yields

$$\bar{A}_m(\bar{k}) = \frac{\sqrt{2} \bar{k}_m}{\bar{k}_m^2 - \bar{k}^2} \left[ 1 - (-1)^m e^{i\bar{k}} \right]. \quad (3.6)$$

Thus the non-dimensional wavenumber filter shape  $|\bar{A}_m(\bar{k})|^2$  for such a sinusoidal mode shape is

$$|\bar{A}_m(\bar{k})|^2 = \frac{4 \bar{k}_m^2}{(\bar{k}_m^2 - \bar{k}^2)^2} [1 - (-1)^m \cos \bar{k}]. \quad (3.7)$$

Figure 3.1 shows typical plots of  $|\bar{A}_m(\bar{k})|^2$  for  $m = 1$  and  $m = 11$  which for convenience have been plotted for  $kL > 0$  only. These wavenumber filter shape plots are characterized by a strong major

lobe near the characteristic wavenumber  $\bar{k}_m$  with side lobes of gradually decreasing amplitude away from  $\bar{k}_m$ . For the  $m = 1$  mode the major lobe of  $|\bar{A}_1(\bar{k})|^2$  is centered about  $\bar{k} = 0$  with a peak value of  $|\bar{A}_1(0)|^2 = 8/\pi^2$ , and the equivalent rectangular bandwidth is  $\Delta\bar{k}_e = \pi^3/4$ . For the  $m = 11$  mode and indeed for all modes with  $m > 1$ , the two major lobes of  $|\bar{A}_m(\bar{k})|^2$  are located at  $\bar{k} = \pm m\pi$  with a peak value of  $|\bar{A}_m(m\pi)|^2 = 1/2$  so that the equivalent rectangular bandwidth of  $|\bar{A}_m(\bar{k})|^2$  is  $\Delta\bar{k}_e = 2\pi$  (Figure 3.1).

Another frequently encountered set of mode shape representations are the beam mode shapes.

$$G_m(\bar{x}) = A_m \sin \bar{k}_m \bar{x} + B_m \cos \bar{k}_m \bar{x} + C_m \sinh \bar{k}_m \bar{x} + D_m \cosh \bar{k}_m \bar{x}, \quad (3.8)$$

where the subscripted coefficients are evaluated by considering the boundary conditions and the normalization of equation (2.28). For plates with two opposite sides simply supported the classical mode shape solution [11] is similar to equation (3.8) in the direction between the two non-simply-supported ends. In principle, it is possible to evaluate the wavenumber filter shapes for such structures by performing the integration indicated by equation (3.3). However, even though the necessary integrals are well known, the resulting expressions for  $|\bar{A}_m(\bar{k})|^2$  are quite complicated and require a great deal of algebraic manipulation to achieve a compact form. In most cases it is probably easier to evaluate  $|\bar{A}_m(\bar{k})|^2$  numerically.

Aupperle and Lambert [6] have succeeded in obtaining an expression for the wavenumber filter shape  $|\bar{A}_m(\bar{k})|^2$  for a beam clamped at both ends. Their result is valid for  $m > 3$  and has the following form when the variables are nondimensionalized according to equations (3.1) and (3.4).

$$|\bar{A}_m(\bar{k})|^2 = \frac{8}{[1 - \bar{k}_m^{-1}]} \left[ \frac{\bar{k}_m^2}{\bar{k}_m^2 + \bar{k}^2} \right]^2 \times \left[ \frac{\sin(\bar{k}_m - \bar{k})/2}{(\bar{k}_m - \bar{k})} + \frac{\sin(\bar{k}_m + \bar{k})/2}{(\bar{k}_m + \bar{k})} \right]^2, \quad (3.9)$$

where  $\bar{k}_m \approx (m + 1/2)\pi$  for  $m > 3$ . Figure 3.2 shows a typical plot for  $\bar{k} > 0$  of this clamped beam wavenumber filter shape for  $m = 9$ . The major lobes are located at  $\bar{k} = \pm \bar{k}_m \approx \pm (m + 1/2)\pi$  with a peak value of

$$|\bar{A}_m(\bar{k}_m)|^2 = \frac{1}{2} [1 + (-1)^m / \bar{k}_m]^2 / [1 - 1/\bar{k}_m]. \quad (3.10)$$

Thus the equivalent rectangular bandwidth of the entire wavenumber filter shape is

$$\Delta \bar{k}_e = 2\pi \left[ 1 - \frac{1}{\bar{k}_m} \right] / \left[ 1 + \frac{(-1)^m}{\bar{k}_m} \right]^2. \quad (3.11)$$

For large  $\bar{k}_m$  both the peak and bandwidth values for the clamped beam wavenumber filter shape approach the corresponding values for the wavenumber filter shape of a sinusoidal mode shape as given by

equation (3.7). This means that for the higher order modes, the major lobe characteristics for wavenumber filter shapes  $|\bar{A}_m(\bar{k})|^2$  due to either sinusoidal or clamped beam mode shapes are essentially equivalent.

### 3.2 Analytical Evaluation of High Wavenumber Behavior

When it is possible to obtain  $|\bar{A}_m(\bar{k})|^2$  by performing the integration of equation (3.3), the resulting expressions can be used to evaluate  $|\bar{A}_m(\bar{k})|^2$  for all  $\bar{k}$ . In some situations only the high wavenumber behavior of  $|\bar{A}_m(\bar{k})|^2$  may be needed, and for such cases another analytic approach is useful. In chapter 2 a series expansion for  $A_m(k)$  was obtained (equation (2.31)) which is valid for large  $k$ . By evaluating the first non-zero derivative of the mode shape  $g_m(x)$  at the boundaries, it is possible to use equation (2.31) to obtain an approximate expression for  $|A_m(k)|^2$  which is accurate for  $k \gg k_m$ .

As an example consider the beam clamped at both ends. The boundary conditions are  $g_m(0) = g_m(L) = g'_m(0) = g'_m(L) = 0$ , and the non-dimensional mode shape is

$$G_m(\bar{x}) = [(\cosh \bar{k}_m \bar{x} - \cos \bar{k}_m \bar{x}) - \epsilon_m (\sinh \bar{k}_m \bar{x} - \sin \bar{k}_m \bar{x})], \quad (3.12)$$

where for  $m > 3$ ,  $\bar{k}_m \approx (m + 1/2)\pi$  and  $\epsilon_m \approx 1$ . From this equation we obtain

$$G''_m(0) = (-1)^{m+1} G''_m(1) = 2\bar{k}_m^2 \quad (3.13)$$

If equation (2.31) is non-dimensionalized on L and the above values for the various derivatives are applied, the resulting approximation for  $\bar{A}_m(\bar{k})$  is

$$\bar{A}_m(\bar{k}) \sim \frac{-i 2 \bar{k}_m^2}{\bar{k}^3} \left[ 1 + (-1)^m e^{i\bar{k}} \right] + O\left(\frac{1}{\bar{k}^4}\right). \quad (3.14)$$

Thus, the high wavenumber approximation for the wavenumber filter shape of a clamped beam is given by

$$|\bar{A}_m(\bar{k})|^2 \sim \frac{8 \bar{k}_m^4}{\bar{k}^6} \left[ 1 + (-1)^m \cos \bar{k} \right]. \quad (3.15)$$

In order to compare this result to the exact expression of equation (3.9), it is helpful to apply appropriate trigonometric identities to equation (3.9) to obtain

$$\begin{aligned} & |\bar{A}_m(\bar{k})|^2 = \\ & \frac{8}{(1 - \bar{k}_m^{-1})} \left[ \frac{\bar{k}_m^2}{\bar{k}_m^4 - \bar{k}^4} \right]^2 \left[ \bar{k}^2 (1 - \cos \bar{k}) - (-1)^m \bar{k} \bar{k}_m \sin \bar{k} + \bar{k}_m^2 (1 + \cos \bar{k}) \right], \end{aligned} \quad (3.16)$$

for  $m > 3$  and  $\bar{k}_m \approx (m + 1/2)\pi$ . The approximate result certainly matches the leading order behavior of equation (3.16) for large  $\bar{k}$ . The envelope of peak values of the side lobes of  $|\bar{A}_m(\bar{k})|^2$  which are predicted by equation (3.15) have been plotted on the actual  $m = 9$  mode shape in Figure 3.2. Such comparisons indicate that for  $m > 5$  and  $\bar{k}_m/\bar{k} > 3$  values of  $10 \log |\bar{A}_m(\bar{k})|^2$  computed from equation (3.15) will fall within 0.5 dB of the exact level. Thus

it is possible to obtain an accurate analytic approximation for the high wavenumber behavior of  $|\bar{A}_m(\bar{k})|^2$  without performing the laborious integrations and algebraic manipulations required to obtain the complete analytic representation.

### 3.3 Numerical Evaluation of Wavenumber Filter Shapes

If the non-dimensionalized mode shape  $G_m(\bar{x})$  is known analytically or available as a set of measured data, it is possible to determine the non-dimensionalized wavenumber filter shape  $|\bar{A}_m(\bar{k})|^2$  for a given value of  $\bar{k}$  by numerically integrating equation (3.3). Equation (3.3) can be rewritten as

$$\bar{A}_m(\bar{k}) = \int_0^1 G_m(\bar{x}) \cos \bar{k}\bar{x} d\bar{x} + i \int_0^1 G_m(\bar{x}) \sin \bar{k}\bar{x} d\bar{x}, \quad (3.17)$$

where  $\bar{k} = kL$  and  $\bar{x} = x/L$ . It is now convenient to define

$$\begin{aligned} R_m(\bar{k}) &\equiv \int_0^1 G_m(\bar{x}) \cos \bar{k}\bar{x} d\bar{x}, \\ I_m(\bar{k}) &\equiv \int_0^1 G_m(\bar{x}) \sin \bar{k}\bar{x} d\bar{x}. \end{aligned} \quad (3.18)$$

Once these two integrals are evaluated, the value of  $|\bar{A}_m(\bar{k})|^2$  is easily obtained as

$$|\bar{A}_m(\bar{k})|^2 = R_m(\bar{k})^2 + I_m(\bar{k})^2. \quad (3.19)$$

Since it is often desirable to evaluate the wavenumber filter shape  $|\bar{A}_m(\bar{k})|^2$  for large values of  $\bar{k}$ , the numerical techniques used to evaluate  $R_m(\bar{k})$  and  $I_m(\bar{k})$  must be capable of handling rapidly oscillating integrands in an efficient manner. One excellent technique



for such situations is the Filon quadrature [12]. This quadrature is based on Simpson's rule, and therefore requires that the interval be divided into an even number  $2n$  of equal parts of length  $h$ . The applicable formulas are obtained from Filon's results [12] as

$$\begin{aligned}
 R_m(\bar{k}) &= h [\alpha G_m(1) \sin \bar{k} + \beta S_2 + \gamma S_1], \\
 I_m(\bar{k}) &= h \{ \alpha [G_m(0) - G_m(1) \cos \bar{k}] + \beta S_4 + \gamma S_3 \},
 \end{aligned}
 \tag{3.20}$$

where  $\alpha$ ,  $\beta$ , and  $\gamma$  are functions of  $\theta = \bar{k}h$  given by

$$\begin{aligned}
 \alpha &= \frac{1}{\theta} + \frac{1}{\theta^2} \cos \theta \sin \theta - \frac{2}{\theta^3} \sin^2 \theta, \\
 \beta &= 2[(1 + \cos^2 \theta)/\theta^2 - \frac{2}{\theta^3} \sin \theta \cos \theta], \\
 \gamma &= 4(\frac{1}{\theta^3} \sin \theta - \frac{1}{\theta^2} \cos \theta),
 \end{aligned}
 \tag{3.21}$$

and the partial sums  $S_1, S_2, S_3, S_4$  are

$$\begin{aligned}
 S_1 &= \sum_{r=1}^n G_r(\bar{x}_{2r-1}) \cos \bar{k} \bar{x}_{2r-1}, \\
 S_3 &= \sum_{r=1}^n G_r(\bar{x}_{2r-1}) \sin \bar{k} \bar{x}_{2r-1}, \\
 S_2 &= \sum_{r=0}^n G_r(x_{2r}) \cos \bar{k} \bar{x}_{2r} - \frac{1}{2} [G_r(0) + G_r(1) \cos \bar{k}], \\
 S_4 &= \sum_{r=0}^n G_r(x_{2r}) \sin \bar{k} \bar{x}_{2r} - \frac{1}{2} G_r(1) \sin \bar{k},
 \end{aligned}
 \tag{3.22}$$

where  $x_r = rh$ . It should be noted that for small  $\theta$  ( $\theta < .1$ ) the formulas of equation (3.21) become numerically inaccurate and the following series expansions are useful:

$$\begin{aligned} \alpha &= \frac{2\theta^3}{45} - \frac{2\theta^5}{315} + \frac{2\theta^7}{4725} - \dots, \\ \beta &= \frac{2}{3} + \frac{2\theta^2}{15} - \frac{2\theta^4}{105} + \frac{2\theta^6}{567} - \frac{4\theta^8}{22275} + \dots, \\ \gamma &= \frac{4}{3} - \frac{2\theta^2}{15} + \frac{\theta^4}{270} - \frac{\theta^6}{11340} + \frac{\theta^8}{997920} + \dots \end{aligned} \tag{3.23}$$

The formulas of equations (3.20) thru (3.23) are easily programmed to permit computer evaluation of  $|\overline{A}_m(\overline{k})|^2$  from either experimental mode shape data or closed form analytic mode shapes. The principal advantage of this method is that it is accurate even at large  $\overline{k}$  since the limitations on accuracy due to sampling considerations apply only to the mode shape  $G_m(\overline{x})$  and not to the entire integrand of equation (3.18). Numerical evaluations of  $10 \log |A_m(k)|^2$  for sinusoidal mode shapes can be compared to the exact result of equation (3.7) to check the accuracy of the numerical methods. Such evaluations indicate that the accuracy of the Filon-Simpson method is still within 0.5 dB at wavenumbers  $\overline{k}$  up to  $\overline{k} \approx 3N$  where  $N$  is the total number of sample intervals for the mode shape  $G_m(\overline{x})$ . If, on the other hand, a standard Simpson's rule method is used to calculate the integrals, the error in  $10 \log |A_m(k)|^2$  reaches 0.5 dB at  $\overline{k} \approx N$ .

### 3.4 $|\bar{A}_m(\bar{k})|^2$ for Beams with Various Boundary Conditions

As an example of the utility of numerical techniques for evaluating wavenumber filter shapes,  $|\bar{A}_m(\bar{k})|^2$  will be evaluated for beams with various combinations of free, simply-supported, and clamped boundary conditions. The following five combinations will be considered:

1. F-F beam, ends free at both  $x = 0$  and  $x = L$ .
2. C-F beam, clamped at  $x = 0$  and free at  $x = L$ .
3. S-S beam, simply supported at both  $x = 0$  and  $x = L$ .
4. C-S beam, clamped at  $x = 0$  and simply supported at  $x = L$ .
5. C-C beam, clamped at both  $x = 0$  and  $x = L$ .

Expressions for both mode shapes and eigenvalues are available in various references [11, 13] for these five conditions and are listed in Appendix A. For higher order modes the computation of the mode shapes as listed in Appendix A becomes inaccurate near  $\bar{x} = 1$  due to the very large values of the hyperbolic terms. It is therefore necessary to manipulate the mode shape equations into forms more suitable for computation. For example, the clamped beam mode shape of equation (A8) can be rearranged as

$$G_m(\bar{x}) = \left( 1 - \frac{\sin \bar{k}_m}{\sinh \bar{k}_m} \right)^{-1} \left[ \frac{\sinh \bar{k}_m (1-\bar{x})}{\sinh \bar{k}_m} + \frac{\sin \bar{k}_m (1-x)}{\sinh \bar{k}_m} - \right. \\ \left. \cos \bar{k}_m \bar{x} - \sin \bar{k}_m \left( \frac{\cosh \bar{k}_m \bar{x}}{\sinh \bar{k}_m} \right) + \cos \bar{k}_m \left( \frac{\sinh \bar{k}_m \bar{x}}{\sinh \bar{k}_m} \right) + \frac{\sin \bar{k}_m \bar{x}}{\tanh \bar{k}_m} \right] \quad (3.24)$$

In this form, none of the terms have values larger than 1 even for very large  $\bar{k}_m$ . With the mode shapes manipulated into forms similar to equation (3.24) it is possible to obtain double precision mode shape values accurate to four decimal places even for modes as high as  $m = 30$ .

Typical numerical results for the wavenumber filter shapes for these 5 boundary conditions and  $m = 5$  are plotted in Figures 3.3 thru 3.7. These values were calculated using the numerical techniques described in Section 3.3. Since  $|\bar{A}_m(\bar{k})|^2 = |\bar{A}_m(-\bar{k})|^2$ , only the levels for  $\bar{k} > 0$  have been plotted. As can be seen from these plots, all five cases exhibit major lobes at their characteristic wavenumbers  $\bar{k}_m$ . These major lobes are all nearly identical with peak values of  $10 \log |\bar{A}_m(\bar{k})|^2$  ranging from -3.0 to -3.4 dB and wavenumber bandwidths between nulls of approximately  $4\pi$ . In all five cases the wavenumber filter shapes also exhibit a side lobe structure. However, when the boundary conditions are not the same at each end, the nulls between the side lobes are not as deep. The peak amplitudes of the side lobes decrease with increasing separation of  $\bar{k}$  from the characteristic non-dimensional wavenumber  $\bar{k}_m$ . However, the exact behavior of this side lobe decay is different for each set of boundary conditions.

In Figure 3.8 the decay in the amplitudes of the side lobes is compared for all five sets of boundary conditions. To simplify this comparison only the envelope of the side lobe peaks has been

plotted for each case. As can be seen from Figure 3.8, the high wavenumber decay of the side lobes is greatest for the clamped-clamped beam and least for the free-free beam. Although the differences in the low wavenumber decay of the side lobes are not as dramatic as the high wavenumber decay, it is interesting to note that the trend is reversed. For example, at  $\bar{k} = 0$  the fully clamped beam has the highest level of  $10 \log |\bar{A}_m(\bar{k})|^2$  of -12.7 dB, the simply-supported beam is slightly lower at -14.9 dB, and the clamped-free beam is lower still at -18.7 dB.

Although the above comparisons have been made for a particular mode (i.e.:  $m = 5$ ), the same behavior is also characteristic of the higher modes. In fact the high wavenumber behavior can be described analytically using the techniques of Section 3.2. From equation (3.15) it is apparent that for  $\bar{k} \gg \bar{k}_m$  the envelope of the side lobe peaks of  $|\bar{A}_m(\bar{k})|^2$  for a clamped beam should be given by

$$|\bar{A}_m(\bar{k})|_{\text{peak}}^2 \sim 16 \bar{k}_m^4 / \bar{k}^6, \quad \bar{k} \gg \bar{k}_m. \quad (3.25)$$

Similarly obtained expressions for the other four sets of boundary conditions are:

a) Free-Free Beam

$$|\bar{A}_m(\bar{k})|_{\text{peak}}^2 \sim 16/\bar{k}^2, \quad \bar{k} \gg \bar{k}_m \quad (3.26)$$

b) Clamped-Free Beam

$$|\bar{A}_m(\bar{k})|_{\text{peak}}^2 \sim 4/\bar{k}^2, \quad \bar{k} \gg \bar{k}_m \quad (3.27)$$

c) Simply-Supported Beam

$$|\bar{A}_m(\bar{k})|_{\text{peak}}^2 \sim 8\bar{k}_m^2/\bar{k}^4, \quad \bar{k} \gg \bar{k}_m \quad (3.28)$$

d) Clamped-Simple Beams

$$|\bar{A}_m(\bar{k})|_{\text{peak}}^2 \sim 2\bar{k}_m^2 [1 + 2\sqrt{2} \bar{k}_m/\bar{k}]/\bar{k}^4, \quad \bar{k} \gg \bar{k}_m \quad (3.29)$$

For  $\bar{k} > 4\bar{k}_m$ , the asymptotic limits given by equation (3.25) to (3.29) agree with the curves of Figure 3.8 to within 0.6 dB.

The numerically obtained wavenumber filter shapes thus agree well with the analytic estimates of high wavenumber behavior. They have again shown the importance of boundary conditions in determining the behavior of  $|\bar{A}_m(\bar{k})|^2$  at high wavenumbers ( $\bar{k} > \bar{k}_m$ ). In addition, the numerical results indicate that the major lobe behavior of  $|\bar{A}_m(\bar{k})|^2$  is relatively independent of the boundary conditions. The primary effect of boundary conditions upon the major lobe is to shift the characteristic wavenumber  $\bar{k}_m$  about which the major lobe is centered. It is also observed that the low wavenumber behavior of  $|\bar{A}_m(\bar{k})|^2$  is moderately dependent upon the boundary conditions.

### 3.5 Summary

In this chapter several techniques have been examined for determining the wavenumber filter shapes of idealized structures. All techniques require that at least some aspects of the mode shape be known. A closed form result for  $|\bar{A}_m(\bar{k})|^2$  is possible in some cases by direct integration of equation (3.3); however, such an approach is often laborious, and numerical integration techniques may be more helpful. When only the high wavenumber behavior of  $|\bar{A}_m(\bar{k})|^2$  is desired, a simple asymptotic analysis can be used. All three techniques show excellent agreement.

#### 4. EXPERIMENTAL METHODS FOR WAVENUMBER FILTER SHAPE DETERMINATION

In the last chapter it was demonstrated that it is possible to determine analytically or numerically the wavenumber filter shapes of an idealized structure once the normal mode shapes are known. Now this chapter will deal with the problem of experimentally determining the non-dimensional wavenumber filter shapes  $|\bar{A}_m(\bar{k})|^2$  of real structures. The basic approach remains that of first determining the normal mode shape  $g_m(x)$  and then non-dimensionalizing to obtain  $G_m(\bar{x})$ . Finally the non-dimensional mode shape is integrated to obtain the wavenumber filter shape  $|\bar{A}_m(\bar{k})|^2$  for the desired values of  $\bar{k}$ .

##### 4.1 Equipment and Procedures for Mode Shape Measurements

The Filon-Simpson technique for numerically determining the wavenumber filter shape was discussed in Section 3.3. This method requires that the mode shape  $G_m(\bar{x})$  be known at an even number of equally spaced points along the length of the structure. The measurement of the sampled mode shape  $G_m(\bar{x}_i)$ ,  $i = 0, 1, 2, \dots, N$  and the subsequent transformation to obtain the wavenumber filter shape  $|\bar{A}_m(\bar{k})|^2$  is directly analogous to the more common time-domain process of sampling a temporal signal  $f(t)$  and subsequently transforming to obtain the frequency spectrum  $F(\omega)$ . As a result of the close analogy it is possible to apply directly many of the results of modern digital sampling theory to this problem.

In time domain sampling the Nyquist frequency is an important parameter which is related to the sampling interval  $\Delta t$  by  $f_N = 1/2\Delta t$ . In the process of digitization, frequency components in the data



which lie above  $f_N$  are reflected about  $f_N$  and hopelessly confounded with the frequency components below  $f_N$  [14]. To prevent this phenomenon, called aliasing, from occurring it is desirable to choose  $\Delta t$  sufficiently small so that it is physically unreasonable for data to exist above the corresponding cutoff frequency  $f_N$ . This usually means selecting  $f_N$  to be about 1.5 to 2 times the highest frequency of interest.

To consider the analagous space domain situation we must apply the following rules of correspondence:

	<u>Time Domain</u>		<u>Space Domain</u>
a)	t, time	→	x, distance
b)	T, period	→	$\lambda$ , wavelength
c)	$\omega$ , radian freq.	→	k, wavenumber

Proper consideration of these rules leads to the analagous Nyquist wavenumber  $k_N$  defined by

$$k_N = \pi/\Delta x, \quad (4.1)$$

where  $\Delta x$  is the sampling interval. If there are N equally spaced intervals in the total length L of the structure, then  $\Delta x = L/N$  and the nondimensional Nyquist wavenumber  $\bar{k}_N = k_N L$  is given by

$$\bar{k}_N = \pi N. \quad (4.2)$$

For best results N should be chosen so that  $\bar{k}_N$  is about twice the maximum wavenumber of interest. Thus, for a fixed number of sample intervals N, the desired range of wavenumber analysis would extend as high as  $\bar{k} = N\pi/2$ . The Filon-Simpson technique discussed in Section 3.3 is compatible with this requirement since it retains accuracy as high as  $\bar{k} \approx 3N$ .

The experimental setup used in the measurement of structural mode shapes is diagrammed in Figure 4.1. The traversing mechanism is a lathe bed with a screw-driven platform. The lead screw allows positioning of the platform over an 11.5 inch range in increments of 0.001 inch. The traversing range was extended to 22.5 inches by attaching a two-position mounting fixture to the platform. This fixture accurately located two transducer mounting positions with an  $11.000 \pm .001$  inch separation. Figure 4.2 shows the positioning of sensors for measuring a membrane mode shape. Only the longitudinal mode shapes were measured, and the traverse was aligned so that the mode shape was measured along the longitudinal centerline of the structure.

The value of the mode shape  $g_m(x_i)$  at a given point  $x_i$  on the structure is determined from the ratio of the RMS response at  $x_i$  to the RMS response at a fixed point on the structure. Since only odd modes were measured, the fixed sensor was positioned at the center of the structure. Both transducers were non-contacting optical displacement sensors manufactured by Mechanical Technology Inc. The model KD-45A Fotonic Sensor was used for the fixed sensor because it has superior set point stability. The model KD-38 Fotonic Sensor was used as the traversing sensor. Both units were used with standard .109 inch diameter probes. As shown in Figure 4.1, the two displacement signals are amplified with Ithaco low-noise preamplifiers and bandpass filtered before being digitized and

processed by an Interdata Digital Computer. The bandpass cutoff frequencies were set one octave above and below the excitation frequency in order to reduce the influence of extraneous acoustic excitation (room background noise, etc.) on the measurement. The computer was used to calculate the RMS signal level of each channel over a 0.5 second interval and then to compute the ratio. At the end of the test the data was punched on a paper tape to facilitate further processing.

As indicated in Figure 4.1, the structures were acoustically excited at a constant frequency. This level of excitation was regulated to maintain a constant RMS displacement amplitude at the fixed sensor. The exact nature of the excitation plays a critical part in determining the quality of the measured mode shape. It is important to maximize the response of the mode to be measured while minimizing the response of all other modes. The first step in this process is to drive the system at the resonant frequency of the mode under consideration. The second step is to insure that the excitation is spatially matched with the desired mode and less well matched with the other modes.

Some initial mode shape measurements yielded poor results because the structure was driven with essentially plane wave excitation from a speaker suspended above the structure. This plane wave excitation was much better coupled to the (1,1) mode of the structure than to the (9,1) mode which was being measured.

Thus, even though the (1,1) mode was non-resonant, its response level was high enough to distort the measured mode shape. In all later tests the structures were driven with the small area acoustic drive shown in Figure 4.3. The drive opening was placed within 1/2 inch of the surface of the structure at a location corresponding to an antinode of the desired mode (Figure 4.3). With this arrangement certain other modes will also be spatially well coupled to the excitation, but no other mode will be better coupled than the desired mode.

Once the equipment was set up and all adjustments were made, the actual data acquisition time was approximately 3 to 4 hours for a 200 point mode shape. During the length of the test it was often necessary to readjust slightly the excitation frequency in order to keep the resonant response at its maximum possible level. This was especially important for the plate mode shapes since the resonance peaks were very narrow.

#### 4.2 Membrane and Plate Construction

The membrane and plate structures that are described here have been designed for the purpose of measuring the low wavenumber components of turbulent boundary layer wall pressure spectra. Two of the prime design requirements for this application are separation of resonant modes and attenuation of the convective wall pressure fluctuations. The combination of these two requirements naturally suggests a long narrow structure. The length of the structure in

the streamwise direction is an important factor in reducing the response to convective excitation, and the large aspect ratio increases the modal separation of the lower order modes.

The standard rectangular membrane was previously constructed by another investigator from a 28 inch diameter mylar bass drum head which was uniformly tensioned on a special bass drum frame. The uniformity of tension was checked by exciting the circular membrane acoustically with pure tones at its resonant frequencies. The Chladni patterns were then observed by using a light dusting of fine sand to identify nodes. The tension was considered sufficiently uniform when the experimental Chladni patterns approximated the symmetrical patterns predicted by theory. Once this state of tension was achieved, a 3/4 inch thick plywood backing plate was cemented to the lower surface of the membrane. This backing plate contained a rectangular shaped cut-out which was lined with plexiglas (Figure 4.4). The plexiglas edges were used to insure a sharply defined boundary for the resulting rectangular membrane. The result of these preparations was a rectangular membrane with the following physical characteristics:

- a. Surface dimensions:  $L_1 = 0.553 \text{ m}$ ,  $L_3 = 0.051 \text{ m}$
- b. Thickness:  $2.16 \times 10^{-4} \text{ m}$
- c. Surface Density:  $0.292 \text{ kg/m}^2$

The standard membrane was later modified in an attempt to reduce its response to convective (i.e.: high wavenumber) turbulent boundary layer excitation. The modification was quite simple,

requiring only the addition of plasticene fillets along the two short edges of the membrane (Figure 4.4). These fillets were of 0.5 inch radius and were intended to reduce the slope of the mode shape near the upstream and downstream boundaries of the membrane. The high wavenumber analysis presented in Section 2.2 indicates that such modifications should reduce the levels of  $|\bar{A}_m(\bar{k})|^2$  for  $\bar{k} \gg \bar{k}_m$ . In Figure 4.5 experimental data is compared for the mode shapes near the boundaries for the standard and modified membranes. This data indicates that the modified membrane has a significant reduction in the slope of the mode shape near the boundaries. The presence of the plasticene also resulted in a slight increase in damping for the modes of the modified membrane.

The basic designs of the two plate structures are shown in Figure 4.6. The rectangular boundaries of each of the plates was defined by a heavy steel frame. Since both plate designs required clamped boundary conditions on at least two sides, the frame design was chosen to provide a heavy, rigid support upon which the plates could be mounted. The frames were constructed from 3/4" thick by 3" wide steel members which were machined to the required lengths and bolted together (Figure 4.6). The total weight of each frame was about 30 lbs., and the ratio of frame mass to plate mass was nearly 200:1.

The plates were made from .034" thick aluminum sheet stock. One plate design called for clamped edges on all four sides. This

was achieved by epoxying the aluminum plate directly to the heavy frame with a rigid formulation of Eccobond 45 epoxy. The second design (designated the S-C-S-C plate) called for clamped boundary conditions along the two long sides of the plate and simply-supported conditions at the other two sides. To approximate simple supports, two vee-shaped notches were milled into the plate as shown in Figure 4.6. The depth of each notch was about .024" so that the ratio R of notch depth to plate thickness was .7. The selection of  $R = .7$  to approximate simple supports was based on the experimental results of Hoppmann and Greenspon [11, 15]. Their investigation of elastic edge restraints included measurements of the effect of the notch ratio R on the fundamental frequency of a square plate. This data indicates that for  $R > .7$  the fundamental frequency is within 5% of the value for simple supports.

In order to achieve the clamped boundary conditions on the other two sides, the notched plate was epoxied to its frame in the same manner as the clamped plate. The effectiveness of the notches in approximating simple supports is demonstrated in Figure 4.7. This figure compares the experimentally determined behavior of the plate mode shapes near the boundaries for the (9,1) modes of both plates. Another indication of the effectiveness of the boundary conditions is given by the location of the resonances. For both plates the measured resonance frequencies of the (5,1) modes were only about 10% lower than calculated values based on

data for ideal boundary conditions given by Leissa [11]. The slight reduction in frequencies is most likely due to the difficulty in achieving a true clamped boundary condition along the lateral sides. Except for the stated differences in boundary conditions, the plates had identical physical characteristics:

- a) Surface Dimensions:  $L_1 = .508 \text{ m}$ ,  $L_3 = .0762 \text{ m}$
- b) Thickness:  $8.64 \times 10^{-4} \text{ m}$
- c) Surface Density:  $2.37 \text{ kg/m}^2$

#### 4.3 Measured Mode Shapes of Membranes and Plates

Mode shape measurements were made on selected modes of all four of the structures described in the previous section. Both the membranes and the plates had sufficiently high aspect ratios to insure that a large number of low order modes were well separated in frequency. The modes of interest are the 1st order lateral modes which have odd mode numbers for the longitudinal direction (i.e.: the 5,1 mode, 7,1 mode, etc.). It is the longitudinal mode shape which is critically important to the low-wavenumber measurement program; thus, only the longitudinal mode shapes of the structures have been measured.

The membrane mode shapes that were measured are shown in Figures 4.8 to 4.10. The important characteristics of these measured mode shapes are listed in Table 4.1. For ease of plotting, all mode shape plots have been scaled so that their maximum absolute



values are 1.0. The mode shape of the 11,1 mode of the standard membrane is shown in Figure 4.8. The small scale spatial fluctuations which are evident in this mode shape are due primarily to the response of higher order non-resonant modes. Repeated measurements at selected points of the mode shape indicate that the mode shape measurement is repeatable to within 1%, while many of the mode shape variations of Figure 4.8 range from 5 to 8%. Thus the observed variations cannot be due merely to experimental variability. Another indication of the presence of other modes in the measured response is the relatively high response levels (10 to 20%) at what should be the nodes of the 11,1 mode being measured.

The reason for this noticeable presence of other modes is the moderate level of damping ( $\eta = .01$ ) characteristic of this (11,1) mode. This can be seen by considering the relative response of two modes of a structure when excited at the resonant frequency  $\omega_L$  of the lower order mode. The modal displacement response is given by equation (2.13). If we limit consideration to modes which are equally well coupled to the excitation, then the modal pressure  $P_{mn}(\omega)$  is the same for each of the two modes. For purposes of comparison, the displacement response  $w_R$  of the resonant mode is given by

$$w_R \propto \frac{1}{\sigma \eta_L \omega_L^2},$$

while the response  $w_H$  of the higher order mode is stiffness controlled so that

$$w_H \propto \frac{1}{\sigma(\omega_H^2 - \omega_L^2)}$$

where  $\omega_L$  and  $\omega_H$  are the resonant frequencies of the resonant mode and higher order mode, respectively. The relative response is

$$\frac{w_H}{w_R} \propto \frac{\eta_L}{(\omega_H/\omega_L)^2 - 1} . \quad (4.3)$$

Equation (4.3) shows that the relative influence of a higher order non-resonant mode on the total response depends directly upon the damping factor of the resonant mode. This means that the degree of contamination of the measured mode shapes by non-resonant modes increases as the damping increases. This can be observed qualitatively from the mode shape data by comparing the (9,1) mode of the modified membrane (Figure 4.9) to the (9,1) mode of the clamped plate (Figure 4.11). The (9,1) mode of the modified membrane has the damping factor  $\eta = .012$ , and the mode shape exhibits the small scale variations typical of non-resonant contributions. On the other hand, the (9,1) mode of the clamped plate has a significantly smaller damping factor of  $\eta = .0031$ , and its mode shape is virtually free of small scale variations.

The preceding comparison is typical of the measured mode shape data in general. The membranes had higher damping (Table 4.1),

and thus the measured mode shapes exhibited non-resonant contributions and poorly defined nodes. The plates (Figure 4.11 to 4.14) had much less damping, and their mode shapes exhibited well defined nodes and much less small scale spatial variation.

The measured modes as plotted in Figures 4.8 to 4.14 have not yet been properly normalized for purposes of wavenumber filter shape calculation. These measured mode shapes have been presented in a non-dimensional form and scaled in magnitude so that their maximum absolute values are all unity. However, the accurate calculation of  $|\bar{A}_m(\bar{k})|^2$  for these measured mode shapes requires that the mode shapes be normalized according to equation (2.28). The appropriate normalizing constant  $C_m$  for each mode shape was determined by integrating equation (2.28) numerically for each set of data. These values are listed in Table 4.1.

#### 4.4 Wavenumber Filter Shapes from Measured Mode Shapes

After being properly normalized as discussed above, the measured mode shapes of Figure 4.8 to 4.14 can be transformed numerically as discussed in Section 3.3 to obtain the wavenumber filter shapes  $|\bar{A}_m(\bar{k})|^2$  of the measured modes. These measured filter shapes can then be compared with theoretical predictions for idealized structures. The results of these comparisons will be used to predict the behavior of the remaining modes which were not measured.

Figures 4.15 through 4.21 show the wavenumber filter shapes calculated from the measured mode shapes. In these figures the calculated levels of  $10 \log |\bar{A}_m(\bar{k})|^2$  have been plotted for  $\bar{k} > 0$ . As expected, the plots are characterized by a major lobe which peaks near the characteristic wavenumber  $\bar{k}_m$  of the mode and a series of side lobes at higher and lower wavenumbers. It will be helpful to compare these measured wavenumber filter shapes to those for the corresponding idealized structures. Both the standard membrane and the S-C-S-C plate filter shapes will be compared to  $|\bar{A}_m(\bar{k})|^2$  for sinusoidal mode shapes as given by equation (3.7). Also the filter shape for the clamped plate will be compared to the clamped beam filter shape of equation (3.9). Although the modified membrane has no corresponding idealized structures, its wavenumber filtering characteristics can reasonably be expected to lie between those of the sinusoidal and clamped beam mode shapes.

The major lobe characteristics of the measured wavenumber filter shapes are nearly identical with those of their idealized counterparts. The peak levels and bandwidths of these major lobes are listed in Table 4.2. The peak levels of the measured filter shapes agree with the corresponding ideal filter shapes to within 0.2 dB, and the equivalent bandwidths agree to within a  $\Delta\bar{k}$  of 0.08. The major lobe characteristics of the modified membrane seem to more closely follow the clamped beam characteristics than the sinusoidal mode shape characteristics.

The high wavenumber behavior of the measured wavenumber filter shapes requires a careful interpretation. For example,  $|\bar{A}_m(\bar{k})|^2$  for the (9,1) mode of the clamped plate as shown in Figure 4.18. At wavenumbers just above the major lobe, this wavenumber filter shape exhibits the expected pattern of side lobes. The peak amplitudes of these side lobes decrease in amplitude as  $\bar{k}$  increases. Superimposed on the measured filter shape is the envelope of side lobe peaks for an ideal (9,1) mode of a clamped beam (Figure 4.18). The measured filter shape shows excellent agreement with the clamped beam model for wavenumbers up to  $\bar{k} \approx 135$ . At higher wavenumbers the side lobe structure changes, and the peak side lobe levels fluctuate randomly about the -60 dB level.

The behavior of  $|\bar{A}_m(\bar{k})|^2$  in this high wavenumber region is of crucial importance to later estimates of response to convective turbulent boundary layer excitation. Thus it is essential to determine whether this observed high wavenumber behavior is truly characteristic of the measured mode shape or is merely an artifact due to other experimental factors. Detailed examinations of the experimental mode shapes near the boundaries (Figures 4.5 and 4.6) show reasonable agreement with theoretical behavior. For uniform structures this implies that the high wavenumber behavior of the measured  $|\bar{A}_m(\bar{k})|^2$  should also agree with theoretical predictions. To investigate the effects of structural non-uniformities

on the behavior of  $|\bar{A}_m(\bar{k})|^2$ , a W. K. B. technique was used to determine the mode shapes of a string with non-uniform density. It was observed from this analysis that the behavior of the wavenumber filter shape was not significantly altered unless the degree of nonuniformity was made quite large. While this does not represent an exhaustive study of possible structural variations, it does imply that small structural non-uniformities are not likely to be important in determining the behavior of  $|\bar{A}_m(\bar{k})|^2$ . Since none of the structures in this investigation exhibited any significant non-uniformities, it is highly likely that the observed high wavenumber behavior is, in reality, an artifact due to experimental causes.

In Section 4.3 the effects of non-resonant modes upon the measured mode shape were shown to be dependent on the damping of the mode being measured. Since the non-resonant effects upon the mode shape are a factor of  $\eta$  smaller than the resonant mode response, we should expect that non-resonant effects upon the resulting  $|\bar{A}_m(\bar{k})|^2$  are a factor of  $\eta^2$  smaller than the major lobe levels characteristic of the desired resonant mode. This implies that at levels of  $10 \log |\bar{A}_m(\bar{k})|^2$  which are  $20 \log \eta$  down from the major lobe peak, it is possible that non-resonant effects are influencing the behavior of the wavenumber filter shape.

In each of the plots of the measured wavenumber filter shapes (Figures 4.15 to 4.21), the level corresponding to  $20 \log \eta$  below the major lobe peak has been marked with an arrow. In each case this level corresponds reasonably well with the level at which the side lobe structure begins to deteriorate. Thus the rather odd behavior of the measured filter shapes at high wavenumbers does not represent the true mode shape but is instead an artifact due to the contamination of the measured mode shape by non-resonant modes. The presence of this non-resonant effect represents an experimental limitation on the use of measured mode shapes for determining the high wavenumber behavior of  $|\overline{A}_m(\overline{k})|^2$  for the modes of real structures. However, in future experiments it may be possible to decrease the importance of this limitation by developing excitation techniques which are designed to spatially match the desired mode only.

Another potentially limiting effect is the inherent variance of the mode shape measurement. These random experimental variations can be appropriately modeled as a random spatial component of the mode shape. When the mode shape with its random component is transformed to obtain the wavenumber filter shape, this random component should yield a relatively flat "noise floor" distributed over a wide wavenumber range. However, as a result of the aliasing phenomenon discussed in Section 4.1, the

random component is, in effect, distributed only over the wavenumber range between the Nyquist wavenumbers  $\bar{k}_N = \pm \pi N$ , where  $N$  is the number of sample intervals. For the four plate experiments the magnitude of this random component was determined by making repeated measurements at selected points on the mode shape. In this way the RMS amplitude of the random component was found to be less than 1% of the amplitude of the mode shape. This implies a maximum noise floor for  $10 \log |\bar{A}_m(\bar{k})|^2$  of -71 dB. In both the plate and membrane experiments, such limitations posed by the experimental variance have proven to be less restrictive than the previously discussed limitations due to non-resonant response.

Now that the measurement limitations have been defined, it is possible to assess more reliably the side lobe behavior of the measured wavenumber filter shapes. Consider first of all the clamped plate filter shapes of Figures 4.18 and 4.19. In Figure 4.18 the side lobe peak levels of the measured  $|\bar{A}_m(\bar{k})|^2$  for the (9,1) mode differ from the ideal clamped beam result by no more than 1.5 dB until the non-resonant response region is reached. For the (15,1) mode result of Figure 4.19 the measured  $|\bar{A}_m(\bar{k})|^2$  is nearly identical with the clamped beam result for the side lobes below the major lobe. For the high wavenumber side lobes the difference between measured and idealized levels increases somewhat at higher wavenumbers but the average trend of



side lobe levels remains consistent until the level of non-resonant response is reached. This excellent agreement leaves little doubt that it is appropriate to approximate the spatial filtering characteristics of this clamped plate by using clamped beam mode shapes.

The measured wavenumber filter shapes for the S-C-S-C plate are shown in Figures 4.20 and 4.21. The side lobe levels of  $|\bar{A}_m(\bar{k})|^2$  for the (9,1) mode (Figure 4.20) lie about 2 dB above the sinusoidal mode shape model for the lower side lobes and about 2 dB below the sinusoidal result for the higher wavenumber side lobes. In both side lobe regions the average trend of the side lobe levels with changing  $\bar{k}$  matches the sinusoidal model quite well. For the (15,1) mode of Figure 4.21 the agreement between the measured levels of  $|\bar{A}_m(\bar{k})|^2$  and the result for the sinusoidal model is even better than for the (9,1) mode. It would thus appear that the machining techniques previously described have adequately approximated simply-supported boundary conditions along the two short edges of the plate, and the wavenumber filter shapes given by equation (3.7) can be used to approximate the actual spatial filtering characteristics of the S-C-S-C plate.

The wavenumber filter shapes for the two membrane structures are shown in Figures 4.15 to 4.17. Unfortunately, the higher membrane damping causes the region of non-resonant contamination

to occur at higher levels than in the plate data. This means that there are fewer uncontaminated side lobes available for comparison to the idealized model. This is especially unfortunate for the case of the modified membrane since its modifications were designed to reduce the side lobe levels at high wavenumbers. The levels of  $|\bar{A}_m(\bar{k})|^2$  for both membranes are compared to the wavenumber filter shapes due to sinusoidal mode shapes. The side lobe levels for the standard membrane (Figure 4.15) are reasonably well matched with the sinusoidal result out to  $\bar{k} \approx 125$ . Similarly, both of the modified membrane filter shapes (Figure 4.16 and 4.17) have side lobe levels which lie within about 2 dB of the sinusoidal mode shape model until the non-resonant response region is reached. It is not possible to determine from this data whether or not the high wavenumber behavior of the modified membrane lies significantly below the levels of the sinusoidal model. For later purposes of estimating the structural response due to convective turbulent boundary layer excitation, it is probably more advisable to model both membrane configurations as having sinusoidal mode shapes.

The preceding discussion of the measured wavenumber filter shapes has led to the general conclusion that it is appropriate to approximate the actual wavenumber filter shapes of these structures by their corresponding idealized models. The justification for this conclusion is based on the observed agreement between the measured and theoretical behavior of  $|\bar{A}_m(\bar{k})|^2$  in Figures 4.15

through 4.21. Although the effects of non-resonant response have made it impossible to determine the true behavior of the measured wavenumber filter shapes at the highest wavenumbers, the excellent agreement between the measured and theoretical behavior of  $|\bar{A}_m(\bar{k})|^2$  at lower wavenumbers strongly suggests that the high wavenumber behavior would also agree with theoretical predictions.

In this investigation the interest in the high wavenumber behavior of  $|\bar{A}_m(\bar{k})|^2$  resulted from the need to make accurate estimates of structural response to convective wall pressure fluctuations (Section 7.2). Such estimates require an accurate model of  $|\bar{A}_m(\bar{k})|^2$  near convective wavenumbers  $\bar{k}_c = \omega L_1 / U_c$ . Typical values of  $\bar{k}_c$  have been marked on the measured wavenumber filter shape plots for the plates (Figures 4.18 through 4.21). For the two modes of the S-C-S-C plate, the measured wavenumber filter shapes are well defined even at the convective wavenumber. For the clamped plate modes, non-resonant effects obscure the actual behavior of  $|\bar{A}_m(\bar{k})|^2$  near  $\bar{k}_c$ ; however, the general trend of the data still suggests that a removal of non-resonant effects would reveal good agreement between theoretical and measured wavenumber filter shapes near the convective wavenumber. These observations provide further support for the conclusions that the analytical models of  $|\bar{A}_m(\bar{k})|^2$  adequately represent the spatial filtering characteristics of the structures that were tested. Thus, it should be possible to use the appropriate analytical models for  $|\bar{A}_m(\bar{k})|^2$  with confidence to estimate structural response.

5. THE APPLICATION OF SPATIAL FILTERING TO TURBULENT  
BOUNDARY LAYER WALL PRESSURE MEASUREMENTS

The analytical results of Chapter 2 have shown that the resonant response of a structure excited by a random pressure field depends upon both its frequency and spatial filtering behavior. Chapters 3 and 4 have discussed in some detail the spatial filtering characteristics of real and idealized structures. The present discussion will deal with the application of these spatial filtering concepts to a specific experimental situation, the measurement of the low wavenumber components of turbulent boundary layer wall pressure fluctuations.

5.1 The Experimental Sources of Excitation

The objective of this phase of the experimental program is to determine the spectrum levels of the low wavenumber components of wall pressure fluctuations beneath a plane turbulent boundary layer. To clarify what is meant by low wavenumber components it is helpful to consider the distribution of wall pressure in both frequency and wavenumber. The wavenumber-frequency spectrum of wall pressure  $\Phi_p(k_1, k_3, \omega)$  was introduced in equation (2.16) as a Fourier transform of the cross spectral density  $\Phi_p(r_1, r_3, \omega)$ . The overall behavior of  $\Phi_p(k_1, k_3, \omega)$  is governed primarily by the convection and decay of eddies in the boundary layer. The convection process leads to high values of  $\Phi_p(k_1, k_3, \omega)$  along a convective ridge defined by

$$k_c = \omega / U_c(\omega) , \quad (5.1)$$

where  $U_c(\omega)$  is the convection velocity characteristic of the frequency

being considered.

Figure 5.1 illustrates the wavenumber-frequency location of the pressure fluctuations which are important to the low wavenumber measurements. The frequency and wavenumber scales in Figure 5.1 have been non-dimensionalized on the outer boundary-layer variables of displacement thickness  $\delta^*$  and free stream velocity  $U_\infty$  so that

$$\omega^* = \omega \delta^* / U_\infty \quad \text{and} \quad k_1^* = k_1 \delta^* . \quad (5.2)$$

The three excitations of interest for this study are acoustic, low-wavenumber and convective pressure fluctuations. For most marine applications the sound speed  $c_0$  is much larger than the free stream velocity  $U_\infty$  so that the acoustic region is well separated from the convective region (Figure 5.1). The low-wavenumber region of interest lies in a wavenumber range (Figure 5.1) which is well below the convective region ( $k_1 \sim \omega / U_c$  but above the acoustic region. Resonant modes lying in this region can be described as having natural frequencies which lie above hydrodynamic coincidence ( $\omega = k_m U_c$ ) but below acoustic coincidence ( $\omega = k_m c_0$ ).

The measured structural response at a given frequency  $\omega$  will be the result of all three components of excitation, acoustic, convective and low wavenumber. Since the goal is to measure the low wavenumber components, the spatial filtering characteristics of the structure must be designed to discriminate against both the acoustic and convective excitations. For the wavenumber filter shapes described in Chapter 4, this discrimination is achieved when the characteristic frequencies  $\omega_{mn}$

and streamwise wavenumbers  $k_m$  of the structural modes lie in the desired low wavenumber region. For example, the locations  $(\omega_m^*, k_m^*)$  of several modes of the S-C-S-C plate are indicated in Figure 5.1.

It is a reasonable physical assumption to model the total wavenumber-frequency wall pressure spectrum of the experimental situation as a sum of statistically independent convective, acoustic and low wavenumber components. Thus,

$$\Phi_p(\vec{K}, \omega) = \Phi_p(\vec{K}, \omega)_{\text{acoustic}} + \Phi_p(\vec{K}, \omega)_{\text{conv.}} + \Phi_p(\vec{K}, \omega)_{\text{low } k} . \quad (5.3)$$

Equation (5.3) can be used with equation (2.22) to obtain the total structural response as a sum of convective, acoustic and low wavenumber responses. To insure that the measured response is dominated by the low wavenumber contribution, it is important to estimate the magnitude of response due to acoustic and convective excitation. If the measured response exceeds the predicted contaminating levels by a sufficient amount, it is appropriate to use the measured data to determine the actual magnitude of  $\Phi_p(\vec{K}, \omega)_{\text{low } k}$ . The next three sections will develop the necessary analytical relations between the excitation and response for each type of excitation.

## 5.2 Structural Response to Low Wavenumber Excitation

In Chapter 2 the resonant response of a rectangular structure was related to the wavenumber-frequency spectrum of the pressure excitation by equation (2.22). Using equations (2.23) and (2.27), the relationship becomes

$$S_{\omega}(x, z, \omega_{mn}) = \frac{f_{mn}^2(x, z)}{(\sigma\eta\omega^2)_{mn}^2} \int_{-\infty}^{\infty} \int_{-\infty}^{\infty} |A_m(k_1)|^2 |A_n(k_3)|^2 \Phi_p(k_1, k_3, \omega_{mn}) dk_1 dk_3. \quad (5.4)$$

This equation forms the basis for evaluating the acoustic and convective response as well as the low wavenumber response.

If the excitation  $\Phi_p(\vec{K}, \omega)$  is reasonably constant in the low wavenumber region, the integral of equation (5.4) will be dominated by contributions from the major lobes of the wavenumber filter shapes,

$|A_m(k_1)|^2$  and  $|A_n(k_3)|^2$ . For the plates and membranes used in the low wavenumber experiments, the modes of interest are the 1st order lateral modes with odd longitudinal mode numbers (i.e.: the (7,1) mode, (11,1) mode, etc.). Thus the lateral filter shape  $|A_n(k_3)|^2$  is always evaluated for  $n=1$  and has its major lobe centered about  $k_3=0$ . The major lobes of the longitudinal mode shapes  $|A_m(k_1)|^2$  are located at the characteristic wavenumbers  $k_m$ . For the structures used, the wavenumber bandwidths are sufficiently narrow to allow the filter shapes to be approximated by Dirac delta functions at  $k = \pm k_m$ . Since  $\int_{-\infty}^{\infty} |A_m(k)|^2 dk = 2\pi$ , the approximations are

$$|A_n(k_3)|^2 = 2\pi\delta(k_3) \quad (5.5)$$

$$|A_m(k_1)|^2 = \pi[\delta(k_1 - k_m) + \delta(k_1 + k_m)].$$

The substitution of equations (5.5) into equation (5.4) yields

$$S_w(x, z, \omega_{mn}) = \frac{2\pi^2 f_{mn}^2(x, z)}{(\sigma\eta\omega^2)_{mn}^2} [\Phi_p(k_m, 0, \omega_{mn}) + \Phi_p(-k_m, 0, \omega_{mn})]. \quad (5.6)$$

For the plate experiments, it is the acceleration response which is measured. Since  $S_a(x, z, \omega_{mn}) = \omega_{mn}^4 S_w(x, z, \omega_{mn})$ , the acceleration spectral density at resonance is given by

$$S_a(x, z, \omega_{mn}) = \frac{2\pi^2 f_{mn}^2(x, z)}{(\sigma\eta)_{mn}^2} [\Phi_p(k_m, 0, \omega_{mn}) + \Phi_p(-k_m, 0, \omega_{mn})]. \quad (5.7)$$

Equations (5.6) and (5.7) provide the basis for the experimental measurements of  $\Phi_p(\vec{K}, \omega)$  in the low wavenumber region. Once the structure has been calibrated by determining its physical parameters and resonance characteristics, it is possible to determine the level of the excitation  $\Phi_p(\vec{K}, \omega)$  from displacement or acceleration measurements. As the equations indicate, there is no way to separate the component of excitation at  $k_1 = k_m$  from that at  $k_1 = -k_m$ . Although it is probable on physical grounds that  $\Phi_p(-k_1, 0, \omega) \ll \Phi_p(k_1, 0, \omega)$  for  $k_1 \delta^*$  sufficiently large, both will be retained by defining

$$P(k_1, 0, \omega) \equiv \Phi_p(k_1, 0, \omega) + \Phi_p(-k_1, 0, \omega). \quad (5.8)$$

In all experiments the response was measured at the center of the structure. From analytic mode shapes it was found that for the odd modes of a membrane

$$f_{mn}^2 \left( \frac{L_1}{2}, \frac{L_3}{2} \right) \sim \frac{4}{L_1 L_3}, \quad (5.9)$$



while for the (n=1, m odd) modes of the clamped and S-C-S-C plates

$$f_{mn}^2 \left( \frac{L_1}{2}, \frac{L_3}{2} \right) \approx \frac{5.044}{L_1 L_3} . \quad (5.10)$$

For the membrane experiment equations (5.6), (5.8), and (5.9) are combined to determine the low wavenumber spectrum  $P(k_1, 0, \omega)$  from the measured displacement spectra by

$$P(k_m, 0, \omega_{mn}) = \frac{L_1 L_3}{8\pi^2} (\sigma\eta\omega^2)_{mn}^2 S_w \left( \frac{L_1}{2}, \frac{L_3}{2}, \omega_{mn} \right) . \quad (5.11)$$

Similarly, equations (5.7), (5.8) and (5.10) relate  $P(k_1, 0, \omega)$  to measured plate acceleration spectra by

$$P(k_m, 0, \omega_{mn}) = \frac{L_1 L_3}{10.09\pi^2} (\sigma\eta)_{mn}^2 S_a \left( \frac{L_1}{2}, \frac{L_3}{2}, \omega_{mn} \right) . \quad (5.12)$$

### 5.3 Structural Response to Acoustic Excitation

The goal of this analysis is to provide a conservative (i.e.: high) estimate of the structural response to pressure excitations in the acoustic region (Figure 5.1). Available acoustic data will be in terms of an acoustic frequency spectrum  $\Phi_A(\omega)$  describing the acoustic background levels in the experimental facility. In order to use this information, an appropriate model for the acoustic wavenumber-frequency spectrum  $\Phi_A(k_1, k_3, \omega)$  must be developed for use in equation (5.4).

For the experimental situation, the test structure is influenced by acoustic waves propagating in the wind tunnel ducting (Figure 5.3). It is the trace wavenumber  $k_T$  of these acoustic waves onto the plane of

the structure which determines the spatial matching between the sound wave and the structure. As illustrated in Figure 5.3, the largest possible value of  $k_T$  is realized by a plane acoustic wave travelling at grazing incidence to the structure. In reality, several acoustic waves may be propagating in various directions so that the acoustic energy represented by  $\Phi_A(\omega)$  is distributed between  $k_T=0$  (normal incidence) and  $k_T = \frac{\omega}{c_0}$  (grazing incidence). The resonant modes of interest for both the membranes and plates are acoustically slow ( $k_m > \frac{\omega}{c_0}$ ), and therefore the acoustic levels contribute to the response via the lower side lobes of  $|A_m(k)|^2$ . Since the exact details of this wavenumber distribution are not known, the model of  $\Phi_A(k_1, k_3, \omega)$  will be chosen to maximize the acoustic response estimate for the  $n=1$  structural modes. The appropriate model is simply the plane wave at grazing incidence so that

$$\Phi_A(k_1, k_3, \omega) = \Phi_A(\omega) \delta(k_3) \delta(k_1 - \frac{\omega}{c_0}) \quad , \quad (5.13)$$

where the model has been scaled so that

$$\iint_{-\infty}^{\infty} \Phi_A(k_1, k_3, \omega) dk_1 dk_3 = \Phi_A(\omega) \quad . \quad (5.14)$$

The substitution of equation (5.13) into equation (5.4) yields

$$S_w(x, z, \omega)_{mn \text{ acoustic}} = \frac{f_{mn}^2(x, z)}{(\sigma \eta \omega^2)_{mn}^2} \Phi_A(\omega) |A_n(0)|^2 |A_m(\frac{\omega}{c_0})|^2 \quad . \quad (5.15)$$

Since  $n=1$  for all modes of interest,  $|A_n(0)|^2$  is at its maximum level which for the membrane is

$$|A_1(0)|^2 = \frac{8L_3}{\pi^2} \quad , \quad (5.16)$$

while for the plates

$$|A_1(0)|^2 \approx .692 L_3 \quad , \quad (5.17)$$

due to the clamped boundary condition in the lateral direction. It is also possible to evaluate the longitudinal filter shape at  $\frac{\omega}{c_0}$ . However, since the acoustic energy represented by  $\Phi_A(\omega)$  is, in reality, distributed over a range of wavenumbers, it is more reasonable to use an average value of  $|A_m(k_1)|^2$  in the vicinity of  $k_A = \frac{\omega}{c_0}$ . For the membranes and the S-C-S-C plate, this local average is easily approximated from equation (3.7) as

$$|A_m(k_1)|^2_{\text{avg.}} = L_1 |\bar{A}_m(\bar{k}_1)|^2_{\text{avg.}} = \frac{4\bar{k}_m^2 L_1}{(\bar{k}_m^2 - \bar{k}_1^2)^2} \quad (5.18)$$

For the clamped plate, the average value of the longitudinal filter shape is most readily obtained from the clamped beam representation of equation (3.16) as

$$|A_m(k_1)|^2_{\text{avg.}} = L_1 |\bar{A}_m(\bar{k}_1)|^2_{\text{avg.}} = \frac{8L_1}{(1 - \bar{k}_m^{-1})} \left[ \frac{\bar{k}_m^2}{\bar{k}_m^4 - \bar{k}_1^4} \right]^2 (\bar{k}_m^2 + \bar{k}_1^2). \quad (5.19)$$

Recalling that the experimental situation deals with measurements of the (n=1, m odd) modes at the point  $(x = \frac{L_1}{2}, z = \frac{L_3}{2})$ , the final estimates of acoustic response can be derived using equations (5.9), (5.10) and (5.15) through (5.19). The results are as follows:

(A) Membrane Displacement Response,

$$S_w \left( \frac{L_1}{2}, \frac{L_3}{2}, \omega_{mn} \right)_{\text{acoustic}} = 13.0 \frac{\bar{k}_m^2}{(\bar{k}_m^2 - \bar{k}_A^2)^2} \frac{\Phi_A(\omega_{mn})}{(\sigma\eta\omega^2)_{mn}^2} \quad , \quad (5.20)$$

with  $k_m = m\pi$  and  $\bar{k}_A = \omega_{mn} L_1 / c_0$ .

(B) S-C-S-C Plate Acceleration Response,

$$S_a \left( \frac{L_1}{2}, \frac{L_3}{2}, \omega_{mn} \right)_{\text{acoustic}} = 14.0 \frac{\bar{k}_m^2}{(\bar{k}_m^2 - \bar{k}_A^2)^2} \frac{\Phi_A(\omega_{mn})}{(\sigma\eta)_{mn}^2}, \quad (5.21)$$

with  $\bar{k}_m = m\pi$  and  $\bar{k}_A = \omega_{mn} L_1 / c_0$ .

(C) Clamped Plate Acceleration Response,

$$S_a \left( \frac{L_1}{2}, \frac{L_3}{2}, \omega_{mn} \right)_{\text{acoustic}} = 27.9 \frac{\bar{k}_m^2 + \bar{k}_A^2}{1 - \bar{k}_m^{-1}} \left[ \frac{\bar{k}_m^2}{\bar{k}_m^4 - \bar{k}_A^4} \right]^2 \frac{\Phi_A(\omega_{mn})}{(\sigma\eta)_{mn}^2}, \quad (5.22)$$

with  $\bar{k}_m = (m + 1/2)\pi$  and  $\bar{k}_A = \omega_{mn} L_1 / c_0$ .

These results can be used to obtain useful estimates of the portion of the structural response which is due to acoustic background levels in the test facility. The predictions of response for the actual tests are discussed in Section 7.1.

#### 5.4 Structural Response to Convective Excitation

In order to make a similar estimate of the structural response to the convective portion of the turbulent boundary layer wall pressure excitations, it is necessary to have an appropriate model of the convective wavenumber-frequency spectrum  $\Phi_c(k_1, k_3, \omega)$ . One such model is described in Appendix B. It is obtained by using the Corcos similarity form [16] for the cross-spectral density  $\Phi_p(r_1, r_3, \omega)$ . By using exponential fits to measured data, it is possible to transform analytically the model of  $\Phi_p(r_1, r_3, \omega)$  to obtain the form of  $\Phi_c(k_1, k_3, \omega)$  given by equation (B5). This model is considered quite accurate at wavenumbers

near the convective ridge ( $k_1 \approx \frac{\omega}{U_c}$ ). However, for reasons to be discussed in Section 7.4, this model overestimates the actual magnitude of  $\Phi_c(k_1, k_3, \omega)$  in the low wavenumber region. As a result, estimates of convective response based on this model would be unreasonably high. However, the model of equation (B5) is quite useful as a guide in determining both the maximum amplitude and wavenumber bandwidth of the new model for  $\Phi_c(k_1, k_3, \omega)$ .

The most important characteristic of the new model must be its variation in  $k_1$ . Willis [18] observed that the  $k_1$  variation of his wavenumber-frequency spectrum was reasonably approximated by a normal distribution of the form

$$F(\omega/k_1 U_c) = \exp[-(\frac{\omega}{k_1 U_c} - 1)^2 / 0.04] \quad .$$

A similar variation with  $k_1$  will be assumed for the new model of  $\Phi_c(k_1, k_3, \omega)$ . The exact details of the  $k_3$  variation are less important, and the  $k_3$  variation will be modeled simply as a constant value over a limited  $k_3$  bandwidth which is centered on  $k_3=0$ .

The transform result of equation (B5) indicates that  $\Phi_c(k_1, k_3, \omega)$  should have its maximum value at  $k_3=0$  and  $k_1 = \frac{\omega}{U_c}$ . This maximum value is given by

$$\Phi_c\left(\frac{\omega}{U_c}, 0, \omega\right) = .728 \Phi_p(\omega) \left[ \frac{U_c U_\infty}{\omega^2} \right] \quad (5.23)$$

If one continues to use equation (B5) as a guide in determining the  $k_3$  bandwidth and normalizes the model so that

$$\Phi_p(\omega) = \iint_{-\infty}^{\infty} \Phi_c(k_1, k_3, \omega) dk_1 dk_3, \quad (5.24)$$

then the following model is obtained:

$$\begin{aligned}
 & \text{A) For } |k_3| \leq \Delta k_3 = \frac{.6\pi\omega}{U_\infty} \\
 \Phi_c(\vec{K}, \omega) &= .728 \Phi_p(\omega) \left[ \frac{U_c U_\infty}{\omega^2} \right] \exp \left[ -23.7 \left( \frac{k_1 U_c}{\omega} - 1 \right)^2 \right] \quad (5.25)
 \end{aligned}$$

$$\begin{aligned}
 & \text{B) For } |k_3| > \Delta k_3 = \frac{.6\pi\omega}{U_\infty} \\
 \Phi_c(\vec{K}, \omega) &= 0 \quad .
 \end{aligned}$$

Figure (5.2) illustrates both the  $k_1$  and  $k_3$  variations of this model. Note that the amplitude of  $\Phi_c(\vec{K}, \omega)$  has virtually vanished before the low wavenumber region is reached.

To obtain an estimate of structural response, equation (5.25) is substituted into equation (5.4) to yield

$$S_w(x, z, \omega_{mn})_{\text{conv.}} = .728 \Phi_p(\omega_{mn}) \left[ \frac{\bar{U} U_\infty}{\omega_{mn}^2} \right] \left[ \frac{f_{mn}(x, z)}{\sigma \eta \omega^2} \right]_{mn}^2 I_1 I_3, \quad (5.26)$$

$$\text{where } I_1 = \int_{-\infty}^{\infty} |A_m(k_1)|^2 \exp \left[ -23.7 \left( \frac{k_1 U_c}{\omega} - 1 \right)^2 \right] dk_1, \quad (5.27)$$

$$\text{and } I_3 = \int_{-\Delta k_3}^{\Delta k_3} |A_n(k_3)|^2 dk_3.$$

In the experimental program, the observed resonant modes were those for which  $n=1$ , and  $|A_1(k_3)|^2$  is centered about  $k_3=0$  (i.e.: see Figure 3.1). Consideration of the experimental parameters ( $\omega$ ,  $U_\infty$  and  $l_3$ ) also reveals that the region of integration indicated for  $I_3$  includes at least the major lobe and the first side lobes of  $|A_1(k_3)|^2$ . This

permits the approximation

$$I_3 \approx \int_{-\infty}^{\infty} |A_1(k_3)|^2 dk_3 = 2\pi$$

which is valid for all the data obtained in this study.

The evaluation of  $I_1$  according to equation (5.27) can be simplified by using the asymptotic analysis discussed in Sections 2.2 and 3.2. According to this analysis the high wavenumber behavior of  $|A_m(k)|^2$  is governed by the first non-zero derivative of the mode shape at the boundaries. It is valid to use such high wavenumber results since the characteristic wavenumbers  $k_m$  of the actual modes lie well below the corresponding convective wavenumbers  $k_c = \frac{\omega}{U_c}$ . As a result, the major contributions to  $I_1$  occur in the wavenumber region ( $k_1 > 3k_m$ ) where the asymptotic analysis is quite accurate.

As was discussed in Section 4.4, the measured mode shapes indicate that the streamwise wavenumber filter shapes  $|A_m(k_1)|^2$  of the actual membrane and plate structures are reasonably approximated by ideal beam mode shapes. It is therefore appropriate to use the available analytic results for ideal clamped and simply supported beams to evaluate  $I_1$ .

Equation (3.15) gives the high wavenumber approximation for the non-dimensional wavenumber filter shapes  $|\bar{A}_m(\bar{k}_1)|^2$  of a clamped beam. Since the exponential term in  $I_1$  varies slowly compared to the  $(1 \pm \cos k_1 L_1)$  variation in  $|\bar{A}_m(\bar{k}_1)|^2$ , it is possible to approximate the  $(1 \pm \cos k_1 L_1)$  term by its average value of unity. Thus for purposes of integration the following approximation will be used for the

clamped plate case:

$$|\bar{A}_m(\bar{k}_1)|^2 \approx \frac{8\bar{k}_m^4}{\bar{k}^6} . \quad (5.28)$$

For the S-C-S-C plate and the membranes, a sinusoidal mode shape result is similarly used to yield

$$|\bar{A}_m(\bar{k}_1)|^2 \approx \frac{4\bar{k}_m^2}{\bar{k}^4} . \quad (5.29)$$

Consideration of the exponential term in  $I_1$  indicates that it should be sufficient to integrate only over the range for which

$|\frac{k_1 U_c}{\omega} - 1| < 0.58$ . To perform the integration it is useful to introduce a new variable defined by

$$\kappa = \frac{k_1 U_c}{\omega} - 1 = \frac{\bar{k}_1 U_c}{\omega L_1} - 1 . \quad (5.30)$$

With this change of variable the form of  $I_1$  for the clamped plate is now

$$I_{1\text{clamped}} = 8\bar{k}_m^4 \left( \frac{\omega L_1}{U_c} \right)^{-5} \int_{-0.58}^{+0.58} (\kappa+1)^{-6} \exp[-23.7\kappa^2] d\kappa , \quad (5.31)$$

while for the other structures

$$I_{1\text{simple}} = 4\bar{k}_m^2 \left( \frac{\omega L_1}{U_c} \right)^{-3} \int_{-0.58}^{+0.58} (\kappa+1)^{-4} \exp[-23.7\kappa^2] d\kappa . \quad (5.32)$$

The integrals in equations (5.31) and (5.32) were evaluated numerically and found to be 0.626 for the clamped case and 0.464 for the simply supported case.

Using the above described results for  $I_1$  and  $I_3$ , it is now



possible to complete the estimates of convective response. For structural response at the point  $(x = \frac{L_1}{2}, z = \frac{L_3}{2})$  the mode shape factors are given by equation (5.9) or (5.10). The resulting estimates of convective response are

A) Membrane Displacement Response

$$S_w \left( \frac{L_1}{2}, \frac{L_3}{2}, \omega_{mn} \right)_{\text{conv.}} = 34.0 \left( \frac{U_\infty}{\omega_{mn} L_3} \right) \left( \frac{\bar{k}_m}{\bar{k}_c} \right)^{-2} \frac{\Phi_p(\omega_{mn})}{(\sigma\eta)_{mn}^2}, \quad (5.33)$$

with  $\bar{k}_m = m\pi$  and  $\bar{k}_c = \frac{\omega L_1}{U_c}$ .

B) S-C-S-C Plate Acceleration Response

$$S_a \left( \frac{L_1}{2}, \frac{L_3}{2}, \omega_{mn} \right)_{\text{conv.}} = 42.8 \left( \frac{U_\infty}{\omega_{mn} L_3} \right) \left( \frac{\bar{k}_m}{\bar{k}_c} \right)^{-2} \frac{\Phi_p(\omega_{mn})}{(\sigma\eta)_{mn}^2}, \quad (5.34)$$

with  $\bar{k}_m = m\pi$  and  $\bar{k}_c = \frac{\omega L_1}{U_c}$ .

C) Clamped Plate Acceleration Response

$$S_a \left( \frac{L_1}{2}, \frac{L_3}{2}, \omega_{mn} \right)_{\text{conv.}} = 115.5 \left( \frac{U_\infty}{\omega_{mn} L_3} \right) \left( \frac{\bar{k}_m}{\bar{k}_c} \right)^{-4} \frac{\Phi_p(\omega_{mn})}{(\sigma\eta)_{mn}^2}, \quad (5.35)$$

with  $\bar{k}_m = (m + 1/2)\pi$  and  $\bar{k}_c = \frac{\omega L_1}{U_c}$ .

As a result of their dependence on  $\bar{k}_c$ , all three of the response estimates are quite dependent upon the streamwise length ( $L_1$ ) of the structure. This supports the use of long structural elements in test programs where convective response is an undesirable contaminant. A comparison of equations (5.34) and (5.35) shows that for modes with similar characteristics the clamped plate will have less convective response by a factor of  $(\bar{k}_m/\bar{k}_c)^2$ . In the actual plate experiments  $\bar{k}_m/\bar{k}_c$  ranged from 0.07 to 0.25, and the clamped plate would therefore be expected to have significantly less convective response than the S-C-S-C plate. The predictions of convective response for the actual test situation are discussed in Section 7.2.

## 6. The Experimental Program for Low Wavenumber Measurements

The total measurement program involved the use of four different rectangular structures; a clamped plate, a S-C-S-C plate, a taut membrane, and a modified membrane. The construction details of these structures were described in Section 4.2. The structures were calibrated by determining the characteristics of the resonant modes, and then the response spectra were measured with the structures excited by a turbulent boundary layer.

### 6.1 Determination of Resonance Characteristics

In Section 5.2 the structural response was shown to be related in a simple way to the low wavenumber wall pressure excitation  $P(k_1, 0, \omega)$ . Equations (5.11) and (5.12) express this relationship for membranes and plates, respectively. In order to determine the levels of  $P(k_1, 0, \omega)$  from the measured response, these equations require a knowledge of the structural dimensions ( $L_1, L_3$ ) and modal resonance characteristics ( $\sigma_{mn}, \eta_{mn}, \omega_{mn}$ ). The surface mass density  $\sigma$  has been included as a modal parameter because fluid loading effects for the membranes cause the effective density  $\sigma_{mn}$  to increase for the lower order modes. The surface density of the plates was significantly greater than that of the membrane, and thus added mass effects were insignificant for the plate experiments.

The basic physical characteristics of the structures are given in Section 4.2. The remaining modal characteristics were experimentally determined and served to calibrate the structural modes. The first step in this calibration process was to identify the modal patterns and resonance frequencies of the modes of interest. To identify the modes, the structures were driven at a single frequency by the small area acoustic drive (Figure 4.3). When a resonant response was observed, the modal pattern was determined by lightly dusting the structure with sand to produce Chladni patterns. Using this technique it was possible to observe odd numbered modes on the membrane from the (5,1) mode at 1185 Hz to the (49,1) mode at 6005 Hz. For the plates the odd numbered modes from the (3,1) mode to the (23,1) mode were identified.

For an ideal membrane the "in vacuo" natural frequencies are related to the mode numbers by equation (2.9). However, the effective surface density ( $\sigma_{mn}$ ) of the membrane changes due to added mass effects. This change in density manifests itself as a change in the membrane wave speed ( $c_{mn}$ ). If this effective wave speed is defined as

$$c_{mn}^2 = T/\sigma_{mn}, \quad (6.1)$$

then equation (2.9) can be rearranged to yield

$$c_{mn} = 2f_{mn} \left[ \left( \frac{m}{L_1} \right)^2 + \left( \frac{n}{L_3} \right)^2 \right]^{-1/2}. \quad (6.2)$$

This equation allows the computation of values of  $c_{mn}$  from the measurements of resonance frequencies and modal patterns. Figure 6.1 shows a plot of the computed values of membrane wave speed ( $c_{mn}$ ) from the actual data for the standard membrane. At high frequencies this curve should approach asymptotically the "in vacuo" wavespeed ( $c = \sqrt{T/\sigma}$ ). By using Figure 6.1 to select this asymptotic value ( $c$ ), it is possible to first compute  $T$  and then use equation (6.1) to determine the effective surface density  $\sigma_{mn}$  for each mode. The results of this procedure are listed in Table 6.1 for several modes of the standard membrane and in Table 6.2 for the modified membrane.

The damping factors ( $\eta_{mn}$ ) for the structural modes of interest were determined experimentally from decay rate measurements. The experimental set-up for these tests is diagrammed in Figure 6.2. All damping tests were made with the structures mounted in the wind tunnel test section. The small area acoustic drive was used to excite the structure at its natural frequencies, and the vibratory response at the center of the structure was monitored. For the membranes the displacement response was monitored with an M.T.I. model KD-38 fotonic sensor, and for the plates the acceleration response was monitored with a Wilcoxon model 91 accelerometer.

After adjusting the drive level to achieve a reasonable response signal, the excitation was shut off, and the resulting decay transient was captured on a B & K model 7502 digital event recorder (Figure 6.2). The decay transient was then played back at a slower speed, and the decaying rms signal level was recorded on a B & K model 2305 graphic level recorder. A typical decay record is shown in Figure 6.2. The damping factor ( $\eta_{mn}$ ) is determined by the equation

$$\eta_{mn} = 1.833 R_1 \tan \alpha / f_{mn}, \quad (6.3)$$

where  $R_1$  = recording rate/playback rate,  $\alpha$  = decay angle, and  $f_{mn}$  = natural frequency (Hz). The equivalent rectangular bandwidth of the mode can also be determined from

$$\Delta f_{mn} = \frac{\pi}{2} \eta_{mn} f_{mn} = 2.88 R_1 \tan \alpha. \quad (6.4)$$

The experimentally determined values of  $\eta_{mn}$  and  $\Delta f_{mn}$  are listed in Tables 6.1 and 6.3.

Damping measurements were also made with varying flow velocities over the structures. No significant changes in damping were observed as the flow speed was changed. Therefore, the damping values that were determined under "no flow" conditions were used for all calculations.

## 6.2 The Wind Tunnel Facility

The experiments were carried out using the facilities and equipment of the Acoustics and Vibrations Laboratory at M.I.T. The low wavenumber measurements were made in the low-noise, low-turbulence wind tunnel shown in Figure 6.3. The basic construction characteristics of this tunnel have been described by Hanson [19], and the boundary layer characteristics have been determined by both Blake [1, 17] and Burton [2]. For the low wavenumber measurements several special steps were taken to reduce the background acoustic levels in the test section. These steps included applying absorption and damping treatments to the blower housing and opening the tunnel ducting behind the test section.

The final test section configuration is shown in Figure 6.4. To allow normal boundary layer development under zero pressure gradient conditions, the upstream tunnel ducting and the test section were left in the standard "closed duct" configuration. The downstream section of ducting was removed, however, and a foam-covered collector was installed at the entrance to the diffuser (Figure 6.4). The prime contributor to the acoustic background levels was thought to be sound generated by unsteady flow in the diffuser. Therefore, the downstream duct removal was designed to allow part of this "diffuser noise" to propagate into the surrounding room. The walls, ceiling and floor of this chamber were lined with fiberglass and acoustic foam in order to provide acoustic absorption.

With the tunnel configuration as described above, the free stream velocity could be adjusted from 10 to 50 m/sec. Using a .040 inch diameter total head tube, mean velocity profiles were measured at the center of the test section for free stream velocities of 20, 29, 40, and 50 m/sec. A typical mean velocity profile is shown in Figure 6.5. From these profiles, values of displacement thickness  $\delta^*$ , momentum thickness  $\theta$ , and shape factor H were computed (Table 6.4). By fitting this same data to a law-of-the-wall format (Figure 6.6), it was also possible to calculate the friction velocity  $U_\tau$ . The boundary layer properties thus determined (Table 6.4) are consistent with typical flat plate values obtained by other investigators.

Each of the test structures was mounted in a fixture which could be located as the bottom wall of the test section (Figure 6.4). Each structure was oriented so that its long dimension was parallel to the air flow, and the top surface of each membrane and plate was carefully positioned to be flush with the test section wall. Since each structure was centered in the test section, the measured boundary layer parameters are characteristic of the flow over the center of the structure.

### 6.3 The Structural Response Measurements

After each structure was mounted in the wind tunnel test section, the spectrum of displacement or acceleration response at the center of the structure was measured at flow velocities of



20, 29, 40 and 50 m/sec. For the membrane tests the displacement response was measured with an M.T.I. model KD-45A fotonic sensor using a .109 inch diameter probe. Since this device is an optical sensor which does not contact the vibrating surface, it did not cause loading problems on the membrane. For the plate measurements, however, the acceleration response was measured with a Wilcoxon model 91 accelerometer. This tiny device weighs only 0.2 grams when used with its mounting base, and its loading effects on the plate response were minimal. The actual loading corrections were experimentally determined to be less than 2.0 dB for all modes of interest, and these corrections were used to adjust the measured acceleration spectra.

The displacement or acceleration signal was first amplified with an Ithaco model 432 low-noise preamplifier and then filtered with an Ithaco model 4212 band pass filter. Next, the signal was analyzed on a Federal Scientific model UA-15A spectrum analyzer, and a Federal Scientific model 1015 spectrum averager was used to average 512 spectrum samples in order to minimize errors due to random fluctuations. Finally, the averaged spectra were recorded on a Mosely model 135C X-Y recorder.

Typical experimental acceleration or displacement spectra for the four structures are shown in Figures 6.7 to 6.10. Only the spectral levels at the resonant peaks are useful as measures

of  $P(k_1, 0, \omega)$  as determined from equations (5.11) and (5.12). The spectra shown in the figures were all obtained for a 0-5 kHz analysis range so that the effective noise bandwidth was 16 Hz. For most of the plate modes the modal bandwidths (Table 6.3) were less than this analyzer bandwidth. This means that the appropriate bandwidth correction for the spectral levels of the resonant peaks must be based on the corresponding modal bandwidths instead of the analyzer bandwidth. Additional plate spectra were obtained for 0-2 kHz and 0-10 kHz analysis ranges with effective noise bandwidths of 6.4 and 32 kHz, respectively. Spectral levels obtained from the three ranges generally differed by less than 2 dB after the appropriate bandwidth corrections were applied, and the levels were averaged to obtain the final values.

For the standard membrane spectrum (Figure 6.7) distinct resonant peaks can be observed which correspond to the odd numbered modes ranging from the (5,1) mode to the (31,1) mode. At frequencies below the (7,1) mode, frame interaction effects prohibit analysis of the response, while at frequencies above the (27,1) mode the response is too close to the instrumentation noise floor to be accurately evaluated. It is also interesting to note that the broad bump in the spectrum just below 4000 Hz is caused by the appearance of the 3 rd. order lateral modes (i.e.: the 1,3 mode; 3,3 mode; etc.) with resulting modal overlap situation. The modified membrane spectrum (Figure 6.8) exhibits similar

characteristics except that its higher damping levels have slightly reduced the spectrum levels of the resonant response so that more of the higher order modes are obscured by the instrumentation noise floor.

For both sets of membrane data the observed spectral levels between resonances are reasonably close to the peak levels (Figure 6.7 and 6.8). At high frequencies this background level is due to the noise floor of the Fotonic sensor, while the rise in the background level below 2000 Hz is consistent with predictions of non-resonant behavior for these membranes. The displacement spectrum used in equation (5.11) includes only the response of the resonant mode. Thus, it was necessary to correct the measured values of displacement spectra to compensate for the close proximity of either the non-resonant response or the instrumentation noise floor. These corrections ranged from 0.5 to 3 dB with the largest corrections occurring for the higher order modes and low flow speed tests. The corrected values of the experimental displacement spectral density  $\hat{S}_w(L_1/2, L_3/2, f_{mn}) = 4\pi S_w(L_1/2, L_3/2, \omega_{mn})$  for the membrane tests are listed in Table 6.5. Data from the 20 m/sec run is not included since all of the peak levels were too close to the instrumentation noise floor to yield reliable data.

The clamped plate acceleration spectrum (Figure 6.9) exhibits sharp resonances corresponding to the odd numbered modes ranging from the (3,1) mode to the (21,1) mode. The fundamental mode does not appear in a distinct form. Its response would be expected to be severely limited by radiation damping, and it is also quite likely that a modal overlap situation exists between the fundamental and the (3,1) mode. Above 4000 Hz the 3 rd. order lateral modes appear and create another modal overlap situation. The intermediate modes (i.e.: the 5,1 mode through the 21,1 mode) are not only well separated in frequency but have peak levels which are well above the observed background levels (Figure 6.9). The S-C-S-C plate acceleration spectrum (Figure 6.10) exhibits similar behavior. For the S-C-S-C plate the response of the fundamental is more clearly defined, and the 3 rd. order modes appear at a slightly lower frequency as would be expected from analytic predictions [11]. The useful modes, however, are still the (5,1) mode through the (21,1) mode.

It is perhaps worthwhile to observe that some of the interpretive problems associated with the membrane spectra have been reduced in the plate spectra. The plate resonances have less damping and are therefore better separated from the non-resonant background levels. Also the measurement of acceleration rather than displacement has an inherent advantage of greater signal levels

at higher frequencies. As a result it was possible to obtain useful plate data even at 20 m/sec flow speed, and background level corrections were typically insignificant. The measured levels of the experimental acceleration spectra

$\hat{S}_a(L_1/2, L_3/2, f_{mn}) = 4\pi S_a(L_1/2, L_3/2, \omega_{mn})$  from the two plates are listed in Table 6.6.

## 7. EVALUATION OF LOW WAVENUMBER DATA

The measured spectral levels discussed in Section 6.3 can now be manipulated to yield experimental values of the wavenumber-frequency spectrum of wall pressure  $P(k_1, 0, \omega_{mn})$ . First, however, it is prudent to compare the measured response levels to estimates of acoustic and convective response. Measured levels which lie very close to the acoustic or convective response estimates should be eliminated from the data. Also, data levels which only appear to be partially influenced by acoustic or convective response can be corrected to provide more realistic values. The corrected data values can then be used with increased confidence to determine the levels of  $P(k_1, 0, \omega)$ . These measured low wavenumber levels can finally be compared to corresponding convective ridge levels and measurements made by other investigators.

### 7.1 Comparison with the Estimated Acoustic Response

In order to estimate the acoustic response for each structural mode, it is necessary to measure the spectrum of background noise  $\Phi_A(\omega)$  in the test section. A direct measurement is virtually impossible since "pseudo-sound" effects would dominate the response of microphones placed directly in the flow. Instead, a microphone was located midway between the end of the test section and the collector (Figure 6.4) so that it was just out of the air flow.

A typical experimental spectrum of  $\hat{\Phi}_A(f) = 4\pi\Phi_A(\omega)$  measured at this point is shown in Figure 7.1. A comparison of acoustic levels for flow speeds ranging from 10 to 50 m/sec. indicates that the acoustic background levels are roughly proportional to the sixth power of the free stream velocity.

The dominant source of the acoustic background levels seems to be from the diffuser. Thus the test section acoustic levels should lie below the measured levels. With a speaker positioned at the inlet to the diffuser and the tunnel off, simultaneous acoustic measurements were made in the test section and at the previous measurement point. This data was used to correct the measured spectral levels of  $\Phi_A(\omega)$  in order to reflect more accurately the actual test section acoustic levels.

Once  $\Phi_A(\omega)$  is known, the remaining task is to determine the response of the structures to acoustic excitation. Two approaches are possible. The experimental approach consists of measuring the response of each structure when known acoustic levels are created in the wind tunnel test section. An analytical approach was previously presented in Section 5.3. In both cases the resulting sensitivity of the structure to acoustic excitation can be expressed as the ratio of the response spectrum to the acoustic spectrum. For convenience these ratios are defined by

$$R_w(\omega) \equiv S_w\left(\frac{L_1}{2}, \frac{L_3}{2}, \omega\right)_{\text{acoustic}} / \Phi_A(\omega) ,$$
$$R_a(\omega) = S_a\left(\frac{L_1}{2}, \frac{L_3}{2}, \omega\right)_{\text{acoustic}} / \Phi_A(\omega) .$$

(7.1)

The analytic results of equations (5.20) through (5.22) are easily rearranged to yield the following acoustic sensitivity ratios:

(A) Membranes,

$$R_w(\omega_{mn}) = \frac{13.0 \bar{k}_m^2}{(\bar{k}_m^2 - \bar{k}_A^2)^2 (\sigma \eta \omega^2)_{mn}^2} \quad (7.2)$$

(B) S-C-S-C Plate,

$$R_a(\omega_{mn}) = \frac{14.0 \bar{k}_m^2}{(\bar{k}_m^2 - \bar{k}_A^2)^2 (\sigma \eta)_{mn}^2} \quad (7.3)$$

(C) Clamped Plate,

$$R_a(\omega_{mn}) = \frac{27.9}{(\sigma \eta)_{mn}^2} \frac{\bar{k}_m^2 + \bar{k}_A^2}{1 - \bar{k}_m^{-1}} \left[ \frac{\bar{k}_m^2}{\bar{k}_m^4 - \bar{k}_A^4} \right]^2 \quad (7.4)$$

Once the resonance characteristics of the structures have been determined (Section 6.1), these ratios can be evaluated for each structural mode of interest. Table 7.1 lists the calculated values of  $R_a$  or  $R_w$  for the four structures used in this program.

In the experimental approach a speaker was placed at the inlet to the diffuser and was used to create a broadband sound field in the wind tunnel test section. The sensitivity of each structural mode to this acoustic excitation was then determined by measuring response spectra for a fixed level of acoustic excitation. A one-inch B&K microphone was flush mounted in the top of the test section in order to monitor the acoustic level. The experimentally determined values of  $R_a$  or  $R_w$  are compared to the corresponding analytic values in Table 7.1.



Most of the measured ratios in Table 7.1 fall within 6dB of the corresponding analytic estimates. Since several experimental difficulties were encountered while conducting the acoustic response experiment, it seems likely that much of the difference between the theoretical and measured acoustic sensitivities is due to experimental inaccuracies. However, for purposes of providing a conservative (i.e.: high) estimate of acoustic response, the higher of the two values will be used.

Predicted levels of the acoustic contributions to plate and membrane spectra were calculated using the acoustic sensitivities of Table 7.1 and the measured acoustic levels  $\Phi_A(\omega)$ . Figures 7.2 and 7.3 show typical comparisons between measured response spectral levels and the predicted acoustic contributions. It should be noted that each data point in these figures corresponds to a peak spectrum level at a given resonance. The lines drawn between data points serve only to help visualize trends in the data and do not imply a smooth spectrum shape between data points.

As shown in Figures 7.2 and 7.3, the estimates of acoustic response typically fall below but reasonably close to the measured levels. In order to preserve the integrity of the data, data points which fell within 4dB of the predicted acoustic levels were discarded. For example, the comparison between the measured and predicted response levels shown in Figure 7.2 indicates that the (9,1) mode data at 1480 Hz should be discarded from the data taken at 40 m/sec. The remaining data points are then corrected to eliminate the calculated acoustic or convective contribution. These corrections ranged from a few tenths of a

decibel to a maximum of about 2dB.

## 7.2 Comparison with the Estimated Convective Response

The response of membranes and plates to convective wall pressure fluctuations was discussed in Section 5.4. As a result of this analysis, equations (5.33) through (5.35) can now be used to estimate the convective response levels for the actual test situations.

All three of these response equations require that the single point wall pressure spectrum  $\Phi_p(\omega)$  be known. Previous measurements of wall pressure spectra in the same wind tunnel are shown in Figure 7.4. These results were also reconfirmed by data taken in an earlier low wave-number program using a test section configuration similar to the one used in these tests. Since Blake's data [1] lies slightly higher than Burton's [2] for the reduced frequencies of interest, the levels of  $\Phi_p(\omega)$  determined by Blake will be used for the response estimates. The higher levels have been chosen in order to provide a conservative (i.e.: high) estimate of convective response.

Using the data from Tables 6.1 through 6.3 and the known structural dimensions, levels of convective response were calculated for the four structures at each flow speed. At a fixed frequency the convective response for the membranes and the S-C-S-C plate exhibits a flow speed dependence of  $(U_\infty)^9$  while for the clamped plate the dependence is  $(U_\infty)^{11}$ . These same speed dependences can be predicted from equations (5.33) through (5.35) by using  $\Phi_p(\omega) \propto (U_\infty)^4$ . This means that, in general, the convective response will become increasingly significant at the higher flow speeds.

Typical predicted levels of convective response are compared with corresponding levels of acoustic response and the measured response in Figures 7.2 and 7.3. For the standard membrane data of Figure 7.2, the convective response is the more significant contaminant for the majority of modes. On the other hand, Figure 7.3 shows that the convective levels are relatively insignificant for the clamped plate data. Indeed, the convective estimates of clamped plate response ranged from 10 to 30 dB below the measured levels, and the significant contaminant was always the acoustic response.

As mentioned in the last section, the criterion for rejecting data was that any measured data levels falling within 4dB of either the corresponding estimate of acoustic or convective response were discarded. Based on this criterion, several data points for the S-C-S-C plate and a few data points for the modified membrane were discarded. As might have been suspected, most of the convectively contaminated data was from the 50 m/sec runs.

A consistent effort was made to insure that both the estimates of acoustic and convective response were biased toward higher levels. The philosophy of this somewhat conservative approach was that it was better to eliminate a few good data points than retain some doubtful ones. However, a second use of the acoustic and convective response estimates was to correct the measured data so as to eliminate the contributions from sources other than the low wavenumber pressure fluctuations. Since the acoustic and convective estimates were biased high, the downward correction of the data may be slightly larger than required. For this reason the data was only corrected for the closer of the two

potential contaminants. A double correction would most likely increase the error of the final result rather than decrease it.

As a result of this generally conservative approach, about one-third of the measured data was discarded. The bulk of the discarded data was from the S-C-S-C plate. The data that was retained was corrected based on the closer of the two estimates of acoustic or convective response. These corrections ranged from 0.3 to 2 dB. The corrected response levels were then used to predict the levels of the wavenumber-frequency spectrum  $P(k,0,\omega)$  as described in the following section.

### 7.3 The Measured Low Wavenumber Levels of $P(k_1,0,\omega)$

To obtain the values of the wavenumber-frequency spectrum of wall pressure  $P(k_1,0,\omega)$ , the corrected membrane and plate response levels were used according to either equation (5.11) or (5.12). The results of these computations are listed in Tables 7.2, 7.3 and 7.4. In order to facilitate data comparisons by removing dimensional considerations, this data has been non-dimensionalized on the outer variables of the boundary layer. Thus,  $P(k_1,0,\omega)$  is non-dimensionalized on  $q^2 \delta^{*3} / U_\infty$ ; where  $q$  is the free stream dynamic head,  $\delta^*$  is the displacement thickness, and  $U_\infty$  is the free stream velocity. Similarly, non-dimensional frequency  $\omega^*$  and wavenumber  $k_1^*$  are as defined by equation (5.2).

Each spectrum level in the Tables should be interpreted as an average level of  $P(k_1, k_3, \omega)$  which is averaged over the wavenumber-frequency domain that is characteristic of the corresponding resonant mode. The frequency domain of each measured level is defined by the

resonant frequency and equivalent bandwidth of its corresponding resonant mode (Tables 6.1, 6.2, and 6.3). The wavenumber domain is characterized by both a  $k_3$  and a  $k_1$  bandwidth. As discussed in Section 3.1 the  $k_1$  bandwidth for all four structures can be approximated as

$$\Delta k_1 \approx \frac{2\pi}{L_1} .$$

Similarly, the  $k_3$  bandwidth is analytically defined as  $\Delta k_3 = \frac{\pi^3}{4L_3}$  for the membranes while numerical results for the plates give  $\Delta k_3 \approx \frac{9.09}{L_3}$ . Thus the wavenumber bandwidths for the membranes are

$$\Delta k_1 \approx 11.4 \text{ (meters)}^{-1}, \quad k_3 \approx 152.6 \text{ (meters)}^{-1}$$

while for the plates they are

$$\Delta k_1 \approx 12.4 \text{ (meters)}^{-1}, \quad k_3 \approx 119.3 \text{ (meters)}^{-1} .$$

Since only the 1st. order lateral modes were considered, each wavenumber region is centered on  $k_3 = 0$  and  $k_1 = k_m$ . For the clamped plate, the characteristic streamwise wavenumber is  $k_m = \frac{(m + 1/2)\pi}{L_1}$ , while for the other structures it is  $k_m = \frac{m\pi}{L_1}$ . The values of  $k_m$  and  $\omega_{mn}$  locate the positions of each data point. Therefore, the non-dimensional values of these parameters have been included with the levels of  $L_p = 10 \log \{P(k_1, 0, \omega) / (q^2 \delta^*{}^3 / U_\infty)\}$  in Tables 7.2, 7.3 and 7.4.

A comparison of levels of  $P(k_1, 0, \omega)$  for the standard and modified membranes (Tables 7.2 and 7.3) reveals that most of the modified membrane data represents the same wavenumber-frequency domain as similar standard membrane data. Also the measured levels agree quite well for the corresponding data points. This should not come as a surprise. As discussed in Section 4.2 the purpose of the plasticene fillets added

to the modified membrane was only to reduce convective response. Indeed the measured membrane wavenumber filter shapes of Section 4.4 (Figures 4.15 to 4.17) show that the major lobe behavior of both membranes is very close to that of the sinusoidal model. Thus, the two membranes should yield similar results. In order to simplify the analysis and plotting of the data, spectrum levels for the two membranes which describe the same wavenumber-frequency region have been averaged to yield a common value.

The non-dimensional levels of  $P(k_1, 0, \omega)$  have been placed in their respective wavenumber-frequency positions in Figure 7.5. The wavenumber-frequency location of each piece of data is marked with an "X" for membrane data and with a dot for plate data. The adjacent number indicates the corresponding value of  $L_p = 10 \log \{P(k_1, 0, \omega) / (q^2 \delta^3 / U_\infty)\}$ . Although it is difficult to make quantitative statements about the data from Figure 7.5, some general observations are possible. First of all, the agreement between the plate and membrane data appears to be good. Both sets of data exhibit a strong decrease in  $L_p$  with increasing  $\omega^*$ . However, the trend of the data with changing wavenumber  $k_1^*$ , is much less clear. Any variation of the data with  $k_1^*$  is certainly small and is perhaps obscured by the overall variability of the data. The actual dependence of the data on frequency and wavenumber will be explored in greater detail in the following section.

#### 7.4 Analysis of the Low Wavenumber Behavior of $P(k_1, 0, \omega)$

The low wavenumber data presented in Figure 7.5 covers a reasonably wide range of reduced frequency  $\omega^*$  and wavenumber  $k_1^*$ . It

should therefore be possible to make quantitative estimates of the dependence of  $P(k_1, 0, \omega)$  on  $\omega^*$  and  $k_1^*$  in the measurement region. However, it may be helpful first to compare the data to levels of the wavenumber-frequency spectrum of wall pressure obtained from a convective ridge analysis.

In Appendix B a convective model for  $\Phi_p(k_1, k_3, \omega)$  is developed by Fourier transforming cross-spectral density data which has been adapted to a Corcos model for  $\Phi_p(r_1, r_3, \omega)$ . In terms of non-dimensional variables and spectra, the resulting model for  $\Phi_p(k_1^*, k_3^*, \omega^*) / (q^2 \delta^{*3} / U_\infty)$  is given by equation (B6) and the peak levels at the convective ridge can be determined from equation (B8). Figure 7.6 shows isocontours of  $\Phi_p(k_1^*, 0, \omega^*)$  which were calculated using equation (B6) with  $k_3^* = 0$ , and Blake's data [17] for  $\Phi_p(\omega)$  and  $U_c(\omega)$ . It should be noted that Blake's convection velocity measurements varied from  $U_c = .76 U_\infty$  at  $\omega^* = .25$  to  $U_c = .6 U_\infty$  at  $\omega^* = 2.5$ .

The dashed region superimposed on the contour plot in Figure 7.6 indicates the region in  $k_1^*$  and  $\omega^*$  for which the experimental data was obtained. If the -80 dB isocontour is extended into the measured data region, it predicts a level of -80 dB at  $\omega^* = 2$  and  $k_1^* = .5$ . However, the measured data levels (Figure 7.5) near this position are approximately -100 dB. Thus, the convective model represented by equation (B6) does not accurately describe the low wavenumber components of the wall pressure spectrum. It does, however, provide a good model for the convective ridge levels.

The poor performance of the convective model at low wavenumbers

may be due, at least in part, to a breakdown in the validity of the similarity form of  $\Phi_p(r_1, r_3, \omega)$  represented by equation (B2). Corcos [16] has argued that the similarity assumption is valid as long as the typical longitudinal wavelength is less than the thickness of the boundary layer. Thus, the similarity assumption is valid for  $8\delta^* > \lambda = \frac{2\pi}{k_1}$  or for  $k_1\delta^* > \frac{\pi}{4} \approx 0.79$ . The low wavenumber region of interest in this study lies principally below  $k_1\delta^* = .8$ . It is, therefore, reasonable to expect that a convective model based on the similarity form would be inaccurate in this region.

There are also experimental difficulties involved in obtaining cross-spectral density measurements which are representative of pressure fluctuations characterized by both low wavenumber and high frequency. Appropriate data requires relatively high frequency measurements taken with large transducer separations. Such experimental situations are often limited by either the dynamic range of the test equipment or the background noise levels in the wind tunnel. As a result, curve fitting techniques such as those which led to equations (B1) or even numerical transform techniques must rely on matching data which is more characteristic of convective fluctuations than low wavenumber fluctuations.

Of course the original purpose of the convective model of equation (B6) was to obtain convective ridge levels of  $\Phi_p(k_1, k_3, \omega)$  with which to compare the measured data. Equation (B2) was used to calculate convective ridge levels corresponding to the range of  $\omega^*$  for the measured data, and these convective ridge levels are compared to the measured data in Figure 7.7 where they are plotted as the solid line.



The measured low wavenumber levels are an average of 36 dB lower than the corresponding convective ridge levels when the values are compared at the same frequency  $\omega^*$ .

The measured data in Figure 7.7 appears to vary slightly more with frequency  $\omega^*$  than the  $(\omega^*)^{-2.75}$  dependence of the convective ridge levels. To quantify the behavior of the data, a least squares analysis was performed. Since the data plotted in Figure 7.7 indicates an approximate straight line behavior with  $\omega^*$ , the following least squares model was formulated:

$$L_p = C_1 [10 \log \omega^*] + C_2 [10 \log k_1^*] + C_3 \quad , \quad (7.6)$$

where  $L_p = 10 \log \{P(k_1, 0, \omega) / (q^2 \delta^{*3} / U_\infty)\}$ . Using standard least squares techniques, the three coefficients were evaluated as

$$C_1 = -3.65 \quad , \quad C_2 = 0.31 \quad , \quad C_3 = -86.5$$

Thus the frequency dependence of the data is  $(\omega^*)^{-3.65}$  while the wavenumber dependence is much less at  $(k_1^*)^{0.35}$ . In fact the calculated  $k_1^*$  dependence is so low that over the total range of  $k_1^*$  for the data only a 2 dB change in  $L_p$  due to wavenumber would be indicated. The standard deviation of the data from the calculated least squares fit was 1.8 dB; thus it is not surprising that it is difficult to ascertain a wavenumber trend in the data from the presentation of Figure 7.5. The average value of  $10 \log k_1^*$  for the data is -3.64. Using this value in Equation (7.6), an approximate fit to the measured data was obtained and plotted as a dashed line in Figure 7.7.

### 7.5 Comparison with Previous Measurements

There is very little published data to which these low wavenumber measurements can be compared. Blake and Chase [4] obtained data with a 4-microphone array, but their results were contaminated by the acoustic background levels in the wind tunnel facility. After making significant reductions in the acoustic levels and improving the 4-microphone array, Jameson [5] obtained low wavenumber data in the region  $k_1 \delta^* \approx .41$ ,  $5 < \frac{\omega \delta^*}{V_\infty} < 8$ . This data was not acoustically contaminated, but there was some uncertainty regarding possible convective contamination.

In a more recent test program, Jameson [8] has also made low wavenumber measurements using rectangular plates as spatial filters. Jameson's plates were .27 m by .18 m with the longer dimension aligned with the flow. The design of the boundary conditions was similar to that of the clamped plate described in Section 4.2. Jameson was able to identify several distinct modes and use them to make measurements of  $P(k_1, k_3, \omega)$ . Only one of these modes, the (7,1) mode, was centered on  $k_3 = 0$  as were the membrane and plate modes of the current data; however, since Jameson's data does not appear to show a strong  $k_3$  variation, it seems appropriate to compare all of Jameson's data to the current data.

For purposes of comparison it is important to notice that Jameson's definition [8] of  $\Phi_p(k_1, k_3, \omega)$  differs slightly from the one presented in equation (2.16). Proper comparison of data requires the conversion

$$P(k_1, k_3, \omega) = (2\pi)^3 \Phi(k_1, k_3, \omega)_{\text{Jameson}} \quad (7.7)$$

Also Jameson does not report the values of  $\delta^*$  which apply to his test situation. However, in earlier tests [5] in the same facility, a typical value of  $\delta^* = .139$  inches was reported. This value has been assumed valid for comparative purposes.

In Figure 7.8 the current data is compared with results obtained by Jameson using a 24 gauge steel plate. This data comparison (Figure 7.8) indicates that Jameson's data predicts low wavenumber levels of  $P(k_1, k_3, \omega)$  which average about 10 dB below the levels obtained in this investigation. However, his data does seem to suggest a dependence on  $\omega^*$  which is similar to the  $(\omega^*)^{-3.65}$  behavior exhibited by the current data. All attempts at reconciling the differences between these two sets of data have thus far been unsuccessful. The important questions of possible acoustic or convective contamination of the current data have been carefully evaluated. The measured response spectra do not appear to be dominated by either convective or acoustic response levels. Moreover, the analytic characterization of the wavenumber filters used by Jameson appears to agree with those of this investigation.

Both sets of data do exhibit a significant amount of scatter. This perhaps implies a need to find more appropriate sets of parameters upon which to normalize the data. It is also possible that differences in the nature of the boundary layers created by Jameson's wall jet experiment and the modified closed jet experiment of this study have contributed to the disagreement in the data. There were also other technical differences between the two experimental programs. For example, Jameson's acceleration response measurements were made using a heavier

accelerometer than the one used in this investigation, and thus loading effects might be more significant. However, it has not yet been possible to explain the difference in the data as resulting from any of the known experimental factors.

## 8. CONCLUSIONS AND RECOMMENDATIONS

Several general conclusions have been formulated during the course of this research. Some of these conclusions pertain to the wavenumber filtering behavior of mechanical structures while others are more closely related to the application of spatial filters to low wavenumber measurements. It has also been possible to formulate guidelines for the design of spatial filters for use in making low wavenumber measurements. These guidelines will be presented as an aid to future investigations.

### 8.1 Conclusions Regarding Wavenumber Filtering

The following conclusions concerning the wavenumber filtering behavior of both real and idealized structures have resulted from this investigation:

- 1) The wavenumber filter shapes  $|A_m(k)|^2$  of both real and idealized structures are dominated by a major response region near the characteristic wavenumber  $k_m$ . This major lobe is relatively insensitive to changes in boundary conditions.
- 2) The high wavenumber behavior of  $|A_m(k)|^2$  is largely determined by the nature of the boundary conditions. Simply asymptotic approximations can be used to predict accurately the high wavenumber behavior of  $|A_m(k)|^2$ . Typical numerical results for a variety of idealized

structures have shown that such asymptotic approximations for  $|A_m(k)|^2$  are accurate to within 0.6 dB for wavenumbers  $k$  such that  $k \geq 4k_m$ .

3) It is possible to determine experimentally the wavenumber filter shapes  $|A_m(k)|^2$  of the modes of an actual structure from detailed measurements of the normal mode shapes. The experimental procedure, however, is both tedious and lengthy and requires the attainment of both frequency and spatial matching of the excitation to the desired resonant mode.

4) The accuracy of the measured wavenumber filter shapes was limited by the presence of non-resonant response in the measured mode shape. The major lobe and low wavenumber side lobes of the measured  $|A_m(k)|^2$  were relatively unaffected; however, the high wavenumber behavior is drastically altered. Since the relative magnitude of the non-resonant response decreases when the modal damping is low, more accurate measurements of the high wavenumber behavior of  $|A_m(k)|^2$  are possible for modes with small damping factors  $\eta$ .

5) The measured wavenumber filter shapes for the standard membrane, S-C-S-C plate and clamped plate were in close agreement with the corresponding analytic predictions. As a result, the use of analytically

determined wavenumber filter shapes in response estimates should accurately predict the actual response of these structures.

6) The effects of non-resonant response made it impossible to determine whether or not the  $|A_m(k)|^2$  for the modified membrane possessed significantly reduced side lobe levels at high wavenumbers. The major lobe and low wavenumber behavior of  $|A_m(k)|^2$  agreed closely with that of an ideal sinusoidal mode shape.

## 8.2 Conclusions Regarding Low Wavenumber Measurements

The primary results of the experimental program of low wavenumber measurements are as follows:

- 1) In the non-dimensional frequency and wavenumber region defined by  $0.18 < k_1 \delta^* < .88$ ,  $k_3 \delta^* \approx 0$  and  $0.8 < \frac{\omega \delta^*}{U_\infty} < 5.1$ , the measured levels of the wavenumber-frequency spectrum of wall pressure  $P(k_1, 0, \omega)$  are an average of 36 dB below the corresponding convective ridge levels at the same frequency.
- 2) A least squares analysis of the behavior of the non-dimensional levels of  $P(k_1, 0, \omega)$  has indicated the following wavenumber-frequency behavior in the data region:

$$P(k_1, 0, \omega) / (q^2 \delta^{*3} / U_\infty) \propto \left( \frac{\omega \delta^*}{U_\infty} \right)^{-3.65} \cdot (k_1 \delta^*)^{0.31}.$$

3) Careful evaluation of the current data indicates that most of the measured response levels are too high to be explained as due merely to acoustic or convective ridge excitations. These contaminating levels were close enough to require some correction of the data, but only data with corrections of 2 dB or less was retained. Thus, the resulting response data would appear to represent directly the low wavenumber excitation.

4) For these experiments there are no significant differences between the levels of  $P(k_1, 0, \omega)$  determined from either membrane or plate data. Since the convective response characteristics of the clamped plate are significantly different from that of the membrane, the good agreement between the levels of  $P(k_1, 0, \omega)$  strongly supports the earlier conclusion that the data is not contaminated by convective response.

5) The technique of transforming cross-spectral density data using a Corcos model to obtain a measure of the wavenumber-frequency spectrum  $\vec{\Phi}_p(\vec{K}, \omega)$  yields inaccurate results in the wavenumber frequency domain of the measured low wavenumber data.

6) The levels of  $P(k_1, 0, \omega)$  of this investigation are approximately 10 dB higher than similar data obtained by Jameson. The reason for this difference is not known.



### 8.3 Guidelines for the Design of Wavenumber Filters

Future investigations of the low wavenumber levels of  $\Phi_p(k_1, k_3, \omega)$  may well require the construction and use of new structures as wavenumber filters. The purposes of this section are to relate insights gained from experience with such measurements and to suggest important steps in the design process.

Experience suggests that plates offer several advantages over the use of membranes for low wavenumber measurements. Design aids such as those collected by Leissa [11] can be used to determine the location of plate resonances, and the construction problems are minimal. Plates, as compared to membranes, also typically have less damping, longer stability of characteristics and greater independence of fluid loading effects. The use of small accelerometers for plate response measurements also eliminates the inherent displacement transducer problem of poor signal-to-noise ratios at higher frequencies. Because of its superior convective ridge rejection, the clamped plate is likely to be the best choice for future measurement situations.

The first step in the design process is to select the material and dimensions of the plate so that the resonant frequencies are well separated and properly located. To minimize convective response, the streamwise length  $L_1$  of the plate should be as long as possible. The width and thickness can then be

selected to obtain the desired resonant frequencies. For a given mode  $(m,n)$  with a characteristic streamwise wavenumber  $k_m$ , the resonant frequency  $\omega_{mn}$  should be high enough to insure that  $k_m \ll \omega_{mn}/U_c = k_c$  yet low enough so that  $|k| > \omega/c_o = k_A$ . The resonant frequencies of the lower order modes for the plates used in this investigation were only 10% lower than the values predicted using data compiled by Leissa [11]. This illustrates the feasibility of using such design data to locate the plate resonances in the desired wavenumber and frequency positions.

After the design of the wavenumber filter has been selected, it is possible to estimate the potential danger of acoustic or convective contamination. This evaluation requires estimates of the total wall pressure spectrum, the boundary layer properties, and background noise levels in the test facility. With this information, the analytic results of Sections 5.2, 5.3 and 5.4 can be used to determine "equivalent" levels of  $P(k_1, k_3, \omega)$  due to acoustic or convective contamination. These equivalent levels represent a sort of noise floor for the actual measurement of  $P(k_1, k_3, \omega)$ .

Consider, for example, a clamped plate. The acoustic response is given by equation (5.22). If this acoustic response is used in equation (5.12), the equivalent acoustic level of  $P(k_m, 0, \omega_{mn})$  is obtained as

$$P(k_m, 0, \omega_{mn})_{\text{acoustic}} = .28 L_1 L_3 \frac{\bar{k}_m^2 + \bar{k}_A^2}{1 - \bar{k}_m^{-1}} \left[ \frac{\bar{k}_m^2}{\bar{k}_m^4 - \bar{k}_A^4} \right]^2 \Phi_A(\omega_{mn}) \quad (8.1)$$

where  $\bar{k}_m = (m + 1/2)$  and  $\bar{k}_A = \frac{\omega_{mn} L_1}{c_o}$ . Similarly, the equivalent convective level is obtained by substituting equation (5.35) into equation (5.12) to yield

$$P(k_m, 0, \omega_{mn})_{\text{convective}} = \frac{1.16 L_1 U_\infty}{\omega_{mn}} \frac{\bar{k}_m^4}{\bar{k}_c^6} \Phi_P(\omega_{mn}), \quad (8.2)$$

where  $\bar{k}_c = \frac{\omega L_1}{U_c}$ . If the evaluation of  $P(k_m, 0, \omega_{mn})_{\text{acoustic}}$  and  $P(k_m, 0, \omega_{mn})_{\text{convective}}$  from these equations does not yield non-dimensional levels of  $P(k_1, 0, \omega)$  below the current measured levels plotted in Figure 7.7, then any experimental measurements using the design under consideration would be expected to be either acoustically or convectively contaminated. To allow an adequate margin of safety, the equivalent levels calculated from equations (8.1) and (8.2) should lie at least 10 dB below the data in Figure 7.7.

Similar expressions for other types of structures can be obtained from the results of Chapter 5. By evaluating the proposed design of a wavenumber filter in this manner, many experimental pitfalls can be avoided. Also if acoustic background level reductions are required, this will be discovered early in the program, and appropriate steps can be taken.

Structure	Mode (m,n)	$f_{m,n}$ (Hz)	Damping $\eta_{m,n}$	$\Delta x$ (inches)	No. of Intervals N	Normalizing Constant $C_m$
Standard Membrane	11,1	1730	.010	0.07	310	1.543
Modified Membrane	9,1	1590	.012	.110	198	1.524
	15,1	2156	.0085	.095	230	1.571
Clamped Plate	9,1	1327	.0031	0.10	200	1.484
	15,1	2430	.0017	0.10	200	1.504
S-C-S-C Plate	9,1	1290	.0038	0.10	200	1.583
	15,1	2410	.0020	0.10	200	1.517

TABLE 4.1 Characteristics of the Measured Mode Shapes

Mode No.	Source of the Wavenumber Filter Shape	Peak Wavenumber $\bar{k}_m$	Peak Level (dB)	Equivalent Wavenumber Bandwidth
9	Measured Clamped Plate	29.1	-3.2	5.88
	Ideal Clamped Beam	29.8	-3.2	5.80
	Measured Modified Membrane	28.4	-3.2	5.86
	Ideal Sinusoidal Mode	28.3	-3.0	5.69
	Measured S-C-S-C Plate	28.7	-3.2	5.69
11	Measured Standard Membrane	34.3	-3.1	5.73
	Ideal Sinusoidal Mode	34.6	-3.0	5.69
15	Measured Clamped Plate	48.1	-3.1	5.71
	Ideal Clamped Beam	48.7	-3.1	5.69
	Measured Modified Membrane	47.9	-3.2	5.81
	Ideal Sinusoidal Mode	47.1	-3.0	5.68
	Measured S-C-S-C Plate	47.4	-3.1	5.66

TABLE 4.2 Major Lobe Characteristics of  $|\bar{A}_m(\bar{k})|^2$

Mode (m,n)	Frequency (Hz)	Damping Factor ( $\eta$ )	Equivalent Bandwidth (Hz)	Effective Density (Kg/m <sup>2</sup> )
5,1	1185	.043	79.8	.439
7,1	1325	.020	40.9	.409
9,1	1480	.011	26.1	.390
11,1	1650	.010	26.7	.376
13,1	1840	.0081	23.6	.364
15,1	2030	.0077	24.7	.358
17,1	2240	.0083	29.5	.348
19,1	2440	.0065	25.2	.345
21,1	2655	.0059	25.0	.341
23,1	2870	.0051	23.0	.337
25,1	3095	.0047	23.2	.333
27,1	3320	.0048	25.0	.329
29,1	3550	.0045	25.0	.326

TABLE 6.1 Experimentally Determined Characteristics  
of the Standard Membrane

Mode (m,n)	Frequency (Hz)	Damping Factor ( $\eta$ )	Equivalent Bandwidth (Hz)	Effective Density (Kg/m <sup>2</sup> )
5,1	1200	.039	74.4	.426
7,1	1345	.019	40.4	.396
9,1	1510	.012	27.6	.375
11,1	1680	.011	28.5	.363
13,1	1880	.0095	26.7	.349
15,1	2075	.0085	27.6	.342
17,1	2285	.0089	32.0	.334
19,1	2495	.0081	31.6	.330
21,1	2720	.0066	28.3	.324
23,1	2935	.0067	31.1	.322
25,1	3170	.0063	31.4	.318
27,1	3370	.0064	34.1	.320
29,1	3605	.0061	34.3	.316
31,1	3840	.0054	32.7	.314

TABLE 6.2 Experimentally Determined Characteristics  
of the Modified Membrane

Plate Type	Mode (m,n)	Frequency (Hz)	Damping Factor ( $\eta$ )	Equivalent Bandwidth (Hz)
C-C-C-C Plate	3,1	805	.023	29.0
	5,1	910	.0082	11.7
	7,1	1070	.0089	14.9
	9,1	1290	.0031	6.3
	11,1	1585	.0049	12.2
	13,1	1960	.0019	5.8
	15,1	2405	.0017	6.4
	17,1	2920	.0018	8.3
	19,1	3500	.0019	10.4
	21,1	4150	.0014	9.1
S-C-S-C Plate	5,1	865	.022	29.4
	7,1	1020	.015	23.8
	9,1	1235	.0038	7.4
	11,1	1520	.0045	10.8
	13,1	1880	.0024	7.2
	15,1	2325	.0020	7.3
	17,1	2825	.0025	11.1
	19,1	3395	.0019	10.0
	21,1	4040	.0015	9.8

TABLE 6.3 Experimentally Determined Characteristics of the Plates



$U_\infty$ m/sec	$Re_\theta$	$\delta^*$ (inches)	$\theta$ (inches)	$H = \frac{\delta^*}{\theta}$	$U_T/U_\infty$
20	$5.1 \times 10^3$	.218	.160	1.36	.037
29	$7.0 \times 10^3$	.206	.151	1.36	.037
40	$9.3 \times 10^3$	.199	.144	1.38	.037
50	$1.1 \times 10^4$	.194	.143	1.36	.038

TABLE 6.4 Mean Properties of the Boundary Layers

Structure	Mode (m,n)	7,1	9,1	11,1	13,1	15,1	17,1	19,1	21,1	23,1	25,1	27,1	29,1	
$10 \log \hat{S}_w \left( \frac{L_1}{2}, \frac{L_3}{2}, f_{mn} \right)$	Standard Membrane	$f_{mn}$ (Hz)	1325	1480	1650	1840	2030	2240	2440	2655	2870	3095	3320	3550
		$U_\infty = 29$ m/sec	-190	-193	-193	-196	-197	--	--	--	--	--	--	--
		$U_\infty = 40$ m/sec	-181	-184	-184	-186	-190	-192	-193	-196	-196	-198	-200	--
		$U_\infty = 50$ m/sec	-174	-177	-176	-179	-182	-183	-185	-188	-189	-191	-194	-193
	Modified Membrane	$f_{mn}$ (Hz)	1345	1510	1680	1880	2075	2285	2495	2720	2935	3170	3370	3605
		$U_\infty = 29$ m/sec	-190	-192	-195	-196	-198	-201	--	--	--	--	--	--
		$U_\infty = 40$ m/sec	-180	-184	-183	-185	-190	-192	-193	-199	-195	--	--	--
		$U_\infty = 50$ m/sec	-174	-180	-178	-180	-184	-186	-188	-192	-191	-196	-197	--

TABLE 6.5 Measured Membrane Displacement Levels  
All Levels Are dB re 1m & 1 Hz

Structure		Mode (m, n)	5,1	7,1	9,1	11,1	13,1	15,1	17,1	19,1	21,1
10 log $\hat{S}_a(L_1/2, L_3/2, f_{mn})$ , dB	Clamped Plate	$f_{mn}$ (Hz)	910	1070	1290	1585	1960	2405	2920	3500	4150
		$U_\infty =$ 20 m/sec	-46	-51	-43	-53	-46	-49	-48	-51	-49
		$U_\infty =$ 29 m/sec	-38	-42	-34	-44	-35	-39	-37	-42	-39
		$U_\infty =$ 40 m/sec	-28	-33	-24	-32	-26	-31	-30	-34	-33
		$U_\infty =$ 50 m/sec	-21	-27	-17	-27	-17	-22	-25	-28	-26
	S-C-S-C Plate	$f_{mn}$ (Hz)	865	1020	1235	1520	1880	2325	2825	3395	4040
		$U_\infty =$ 20 m/sec	-54	-55	-50	-57	-51	-53	-58	-56	-56
		$U_\infty =$ 29 m/sec	-43	-46	-39	-46	-40	-43	-48	-45	-46
		$U_\infty =$ 40 m/sec	-32	-38	-29	-35	-31	-32	-38	-37	-38
		$U_\infty =$ 50 m/sec	-26	-31	-22	-28	-23	-25	-31	-30	-33

TABLE 6.6 Measured Plate Acceleration Spectral Levels  
All Levels Are dB re  $1m/sec^2$  and 1Hz

TYPE OF DATA	MODE (m,n)	STANDARD MEMBRANE		MODIFIED MEMBRANE	
		CALCULATED	MEASURED	CALCULATED	MEASURED
10 log R <sub>w</sub> dB re 1 m/(nt/m <sup>2</sup> )	7,1	-128	-132	-127	-129
	9,1	-127	-124	-127	-132
	11,1	-130	-126	-131	-130
	13,1	-131	-130	-132	-140
	15,1	-134	-132	-135	-143
	17,1	-137	-130	-138	-134
	19,1	-138	-132	-139	-148
	21,1	-139	-140	-140	-134
	23,1	-140	-139	-142	-150
	25,1	-141	-134	-144	-147
	27,1	-143	-139	-146	-145
	29,1	-144	-133	-147	-147
TYPE OF DATA	MODE (m,n)	CLAMPED PLATE		S-C-S-C PLATE	
		CALCULATED	MEASURED	CALCULATED	MEASURED
10 log R <sub>a</sub> dB re 1(m/sec <sup>2</sup> )/(nt/m <sup>2</sup> )	5,1	26	24	16	19
	7,1	22	18	15	18
	9,1	29	26	25	31
	11,1	23	23	22	22
	13,1	30	34	26	23
	15,1	30	31	27	36
	17,1	29	34	24	16
	19,1	27	31	26	32
	21,1	30	--	27	19

TABLE 7.1 Measured and Calculated Sensitivity to Acoustic Excitation

$U_\infty$	29 m/sec				40 m/sec			
$\omega^*$	1.50	1.87	2.08	2.30	1.05	1.31	1.46	1.61
$K_1^*$	.280	.327	.386	.446	.201	.316	.373	.430
$L_p$ (dB)	-93	-98	-100	-99	-87	-92	-95	-97

$U_\infty$	40 m/sec						50 m/sec	
$\omega^*$	1.78	1.93	2.10	2.28	2.45	2.63	.82	1.02
$K_1^*$	.488	.545	.603	.660	.717	.775	.196	.308
$L_p$ (dB)	-98	-98	-101	-99	-101	-101	-84	-86

$U_\infty$	50 m/sec							
$\omega^*$	1.14	1.26	1.39	1.51	1.64	1.78	1.92	2.06
$K_1^*$	.364	.420	.476	.532	.588	.644	.700	.756
$L_p$ (dB)	-90	-93	-91	-93	-97	-95	-97	-99

TABLE 7.2 Measured Low Wavenumber Levels of  $P(k_1, 0, \omega)$  From Standard Membrane Data,  
 $L_p = 10 \log \{P(k_1, 0, \omega) / q^2 \delta^{*3} / U_\infty\}$ .

$U_\infty$	29 m/sec						40 m/sec			
$\omega^*$	1.52	1.71	1.90	2.13	2.35	2.59	1.07	1.33	1.49	1.65
$K_1^*$	.208	.267	.327	.386	.446	.505	.201	.316	.373	.430
$L_p$ (dB)	-94	-98	-100	-100	-101	-103	-87	-92	-93	-98

$U_\infty$	40 m/sec			50 m/sec						
$\omega^*$	1.81	1.98	2.33	.83	1.04	1.16	1.42	1.55	1.82	2.38
$K_1^*$	.489	.545	.660	.196	.308	.364	.476	.532	.644	.868
$L_p$ (dB)	-98	-97	-99	-85	-89	-93	-95	-96	-99	-97

TABLE 7.3 Measured Low Wavenumber Levels of  $P(k_1, 0, \omega)$  From Modified Membrane Data,

$$L_p = 10 \log\{P(k_1, 0, \omega) / (q^2 \delta^{*3} / U_\infty)\}$$

$U_\infty$	20 m/sec										29 m/sec
$\omega^*$	1.78	3.28	4.92	1.58	1.86	2.25	2.76	3.41	4.18	5.08	2.13
$K_1^*$	.240	.445	.582	.188	.257	.325	.394	.463	.531	.600	.420
$L_p$ (dB)	-97	-108	-115	-94	-98	-98	-105	-105	-111	-110	-103

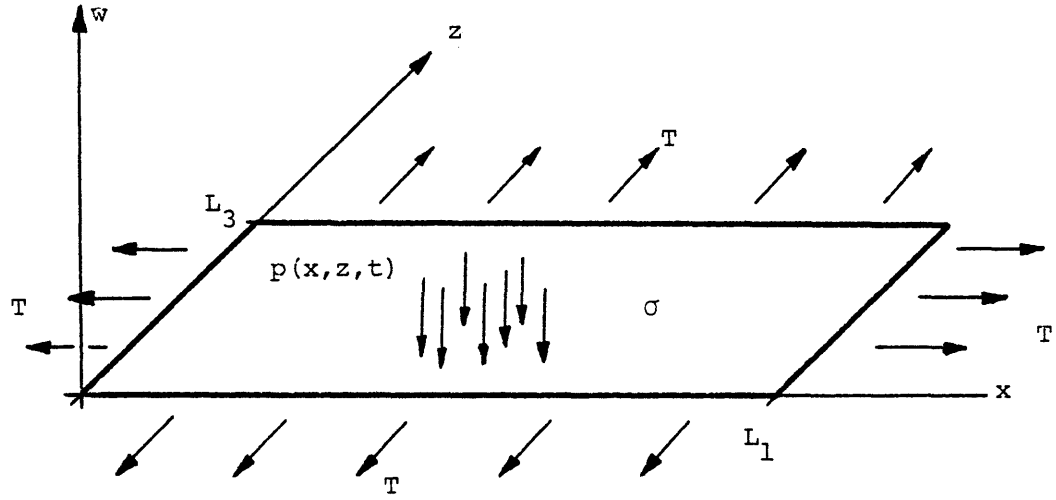
$U_\infty$	29 m/sec						40 m/sec				
$\omega^*$	3.20	1.21	1.46	1.80	2.22	2.72	3.96	2.24	.85	1.02	1.26
$K_1^*$	.55	.243	.307	.372	.437	.501	.631	.531	.234	.297	.359
$L_p$ (dB)	-111	-93	-94	-100	-99	-104	-107	-105	-88	-88	-92

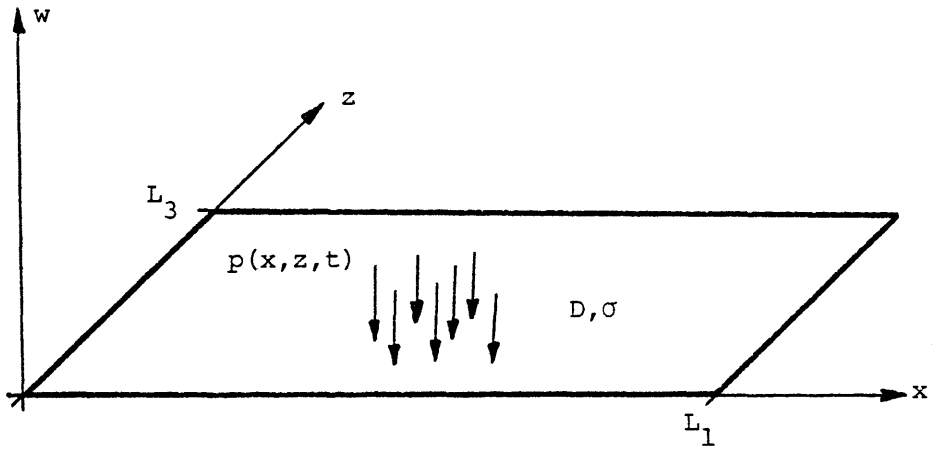
$U_\infty$	40 m/sec				50 m/sec						
$\omega^*$	1.55	1.91	2.31	2.78	.80	.98	1.21	1.49	1.81	2.17	2.57
$K_1^*$	.422	.484	.547	.609	.290	.351	.412	.473	.534	.595	.655
$L_p$ (dB)	-93	-100	-98	-103	-83	-89	-87	-94	-97	-98	-99

TABLE 7.4 Measured Low Wavenumber Levels of  $P(K_1, 0, \omega)$  From Plate Data,

$$L_p = 10 \log\{P(K_1, 0, \omega) / (q^2 \delta^{*3} / U_\infty)\}$$



A) Membrane Geometry



B) Plate Geometry

FIGURE 2.1 Geometrical Considerations for the Rectangular Structures



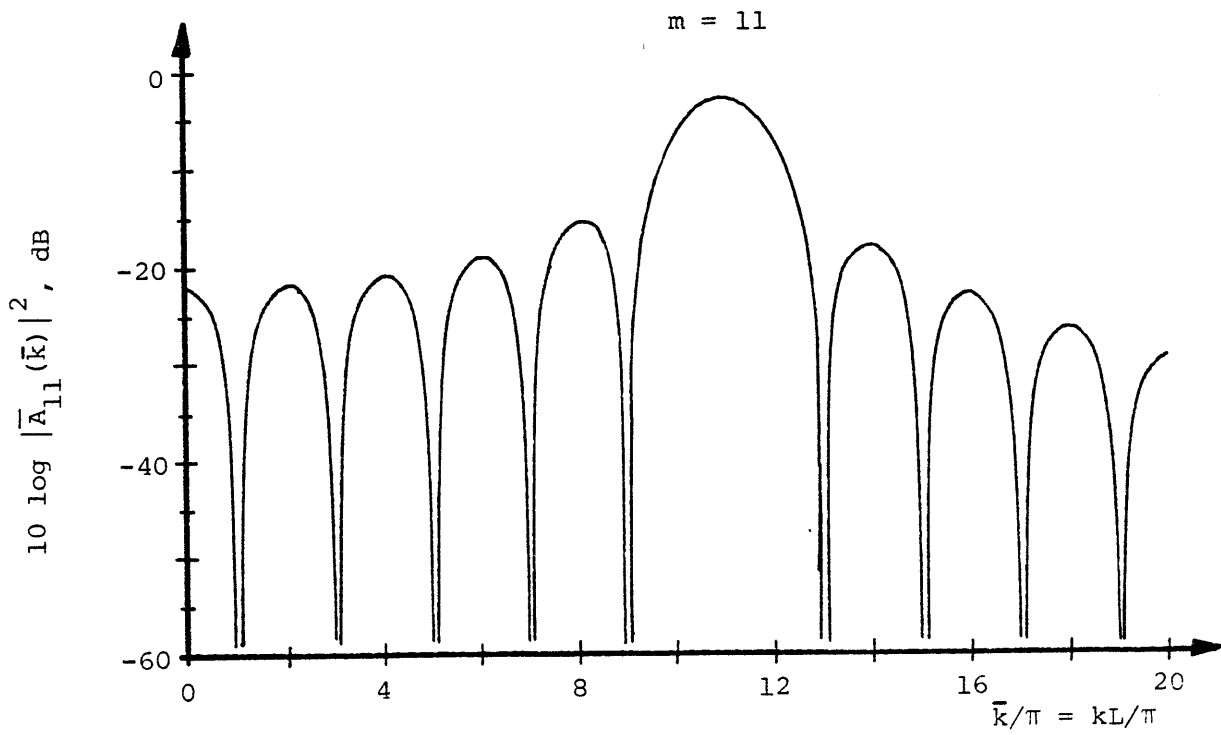
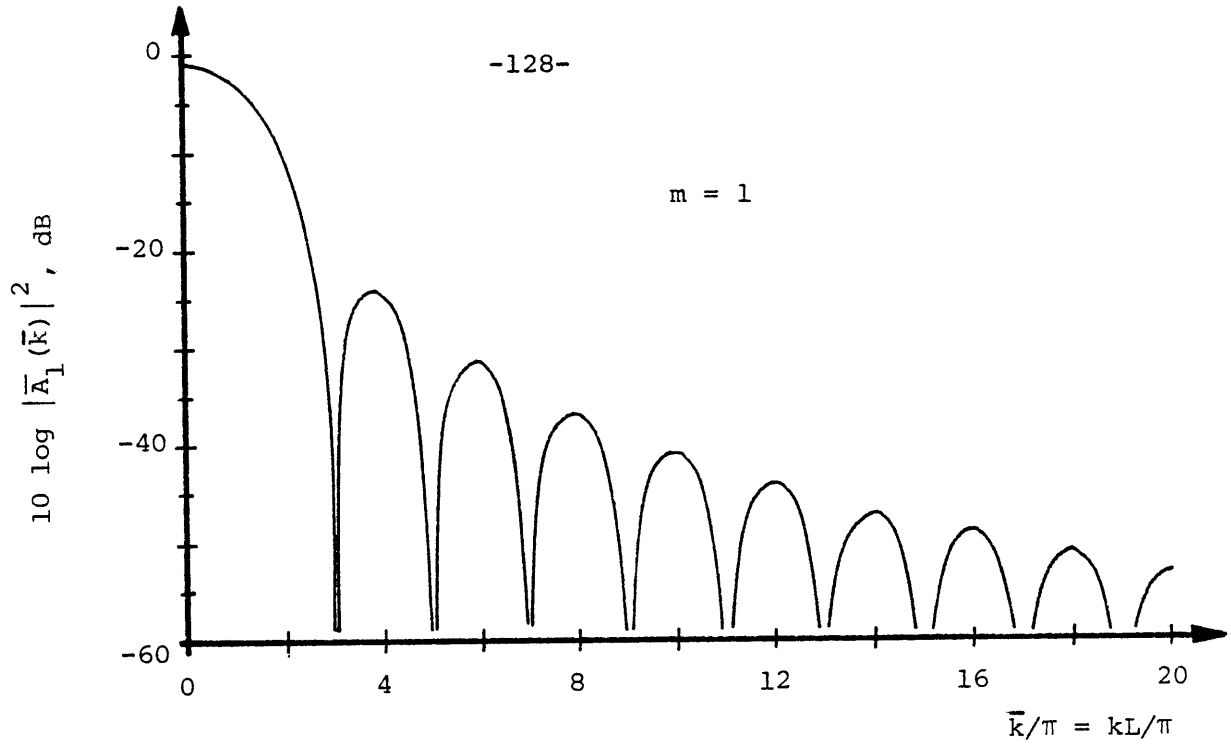


FIGURE 3.1 Wavenumber Filter Shapes for Sinusoidal Mode Shapes

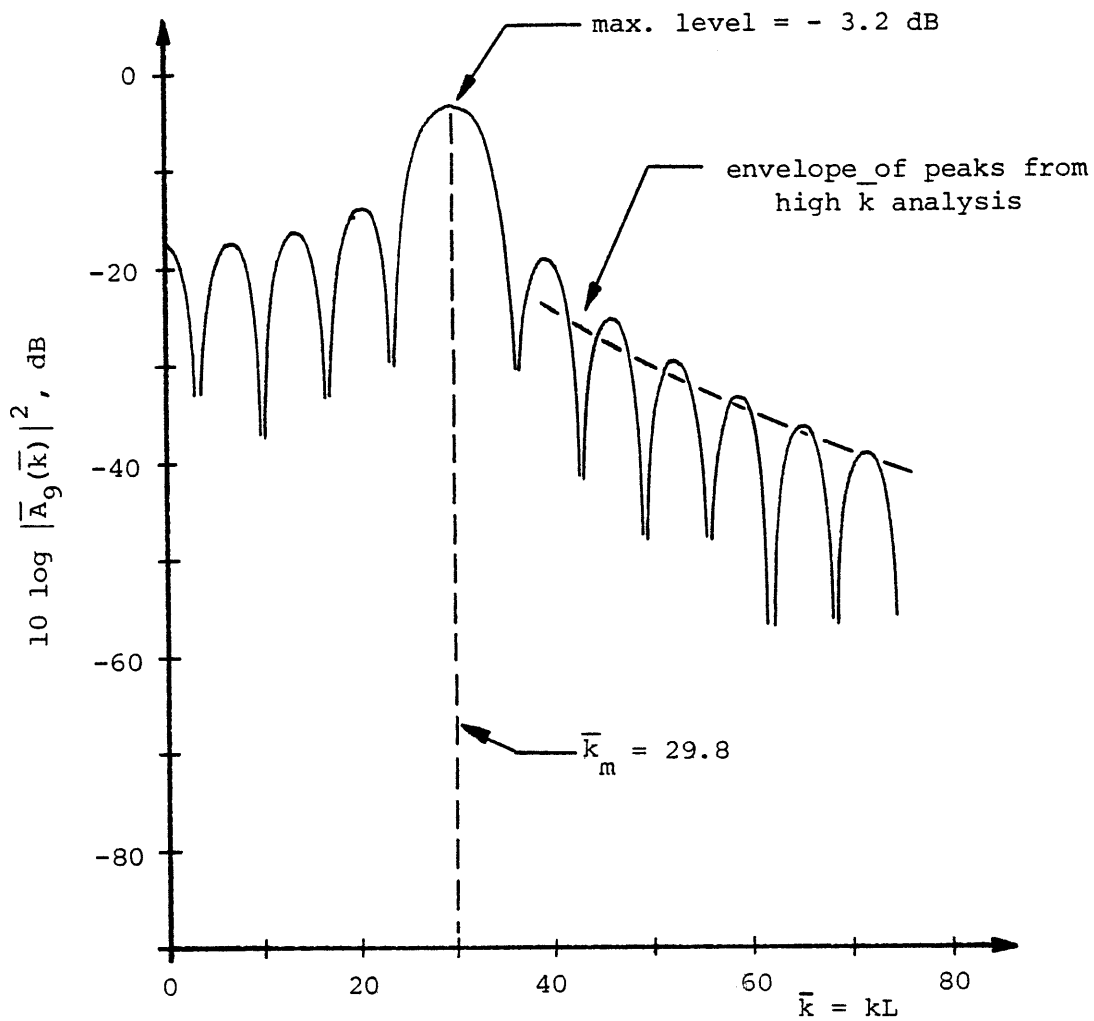


FIGURE 3.2 Wavenumber Filter Shape for a Clamped Beam ( $m = 9$ )

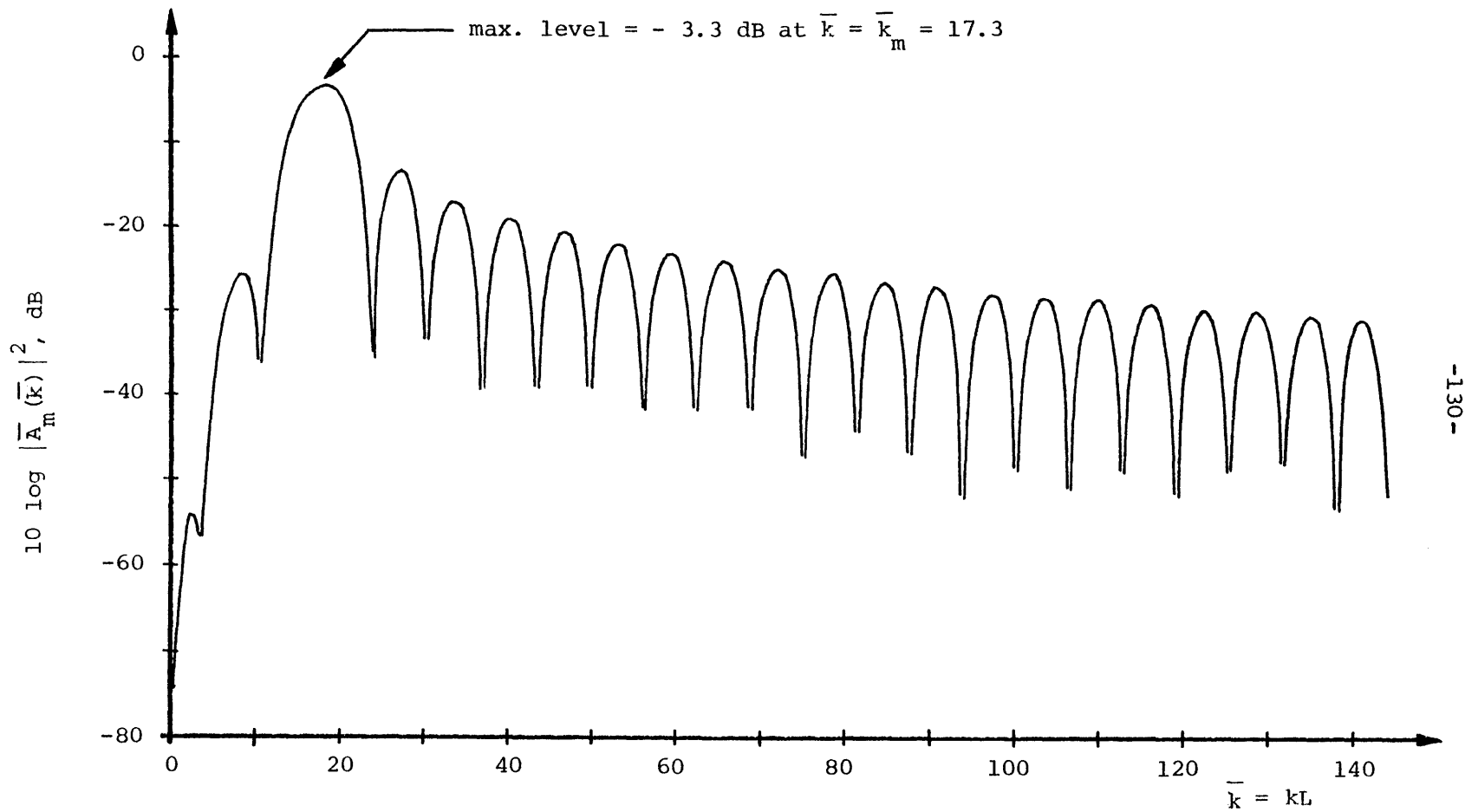
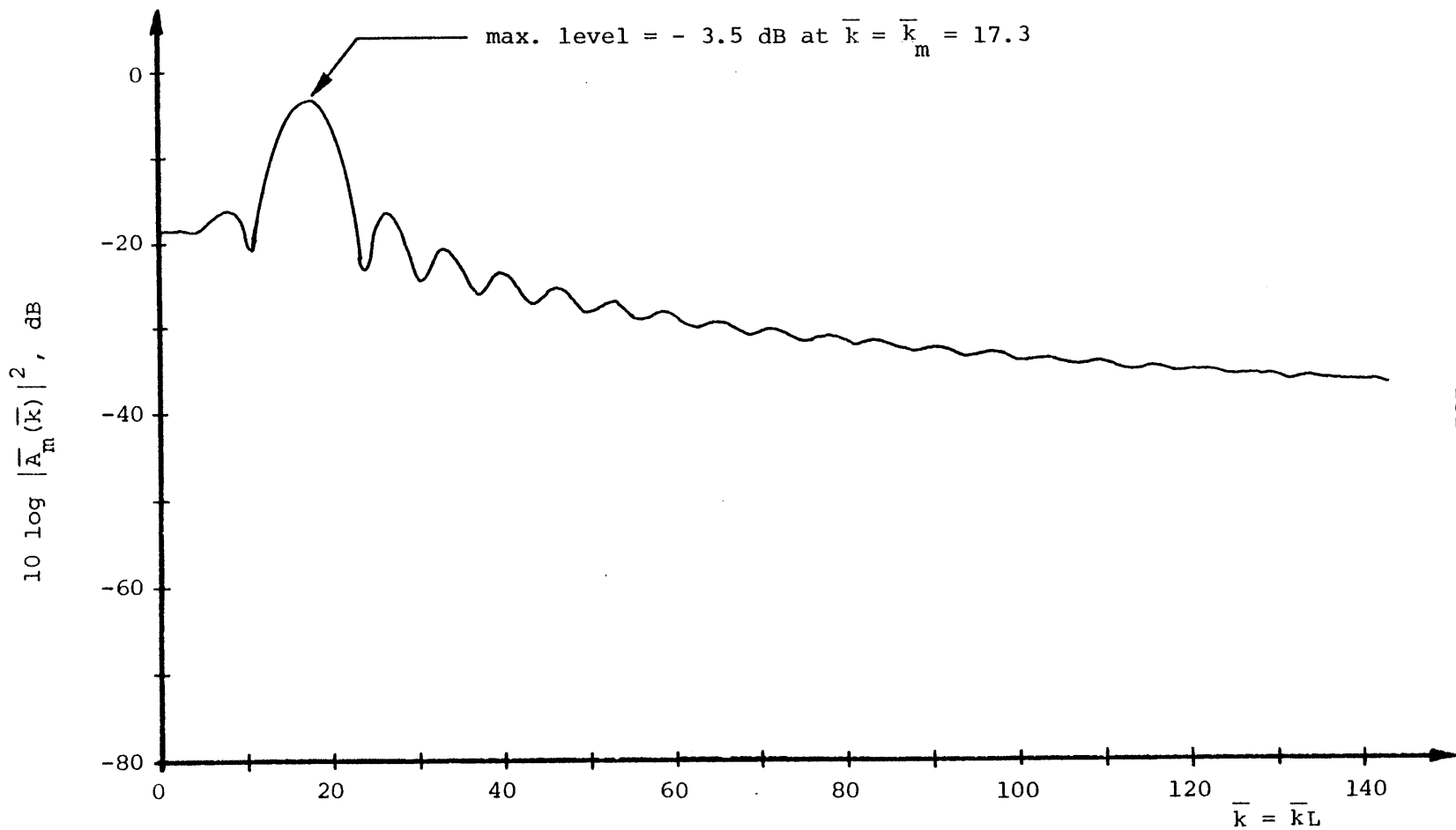


FIGURE 3.3 Wavenumber Filter Shape for a Free-Free Beam ( $m = 5$ )



-131-

FIGURE 3.4 Wavenumber Filter Shape for a Clamped Free-Beam (m=5)

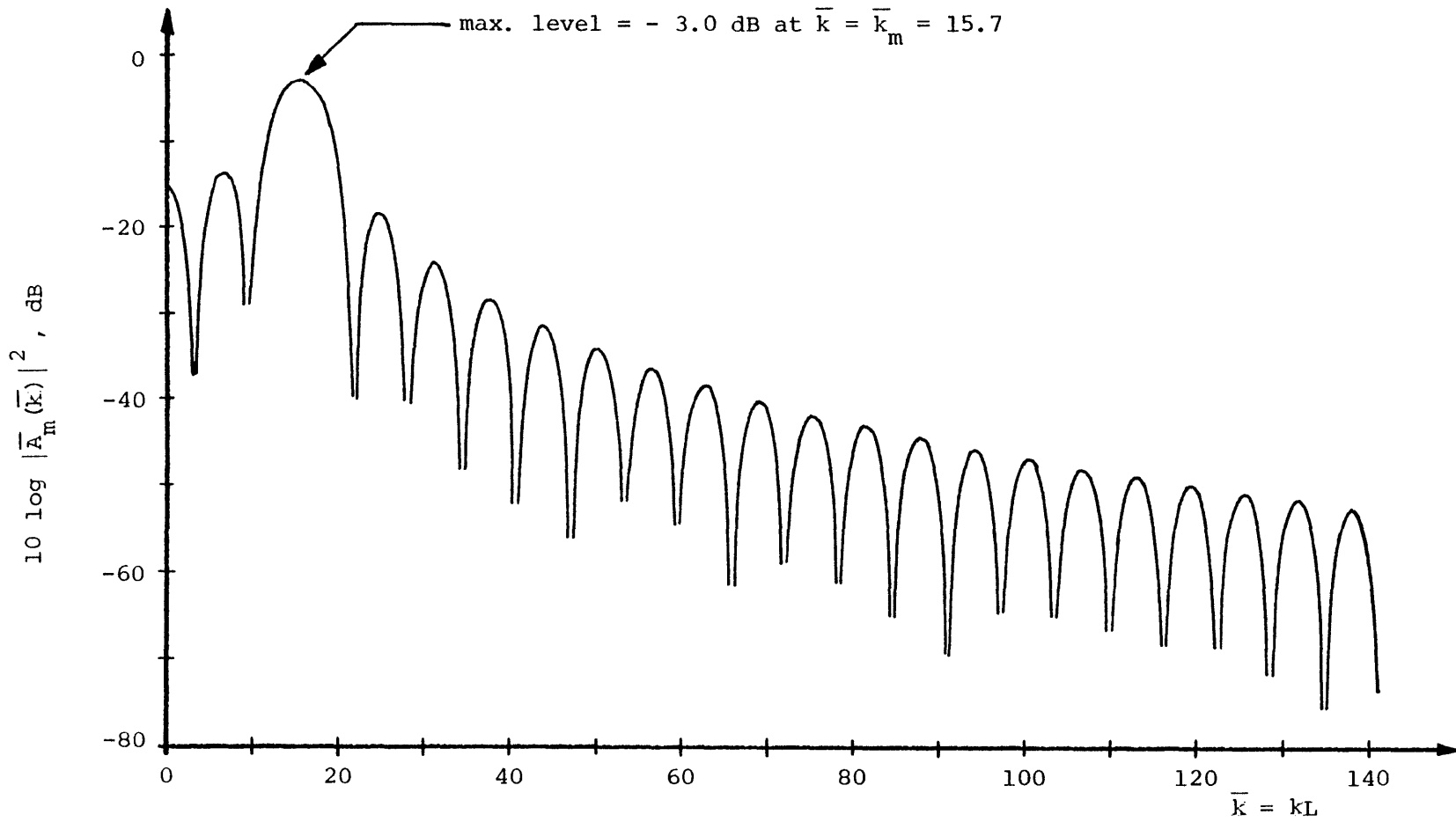


FIGURE 3.5 Wavenumber Filter Shape for a Simply Supported Beam ( $m = 5$ )

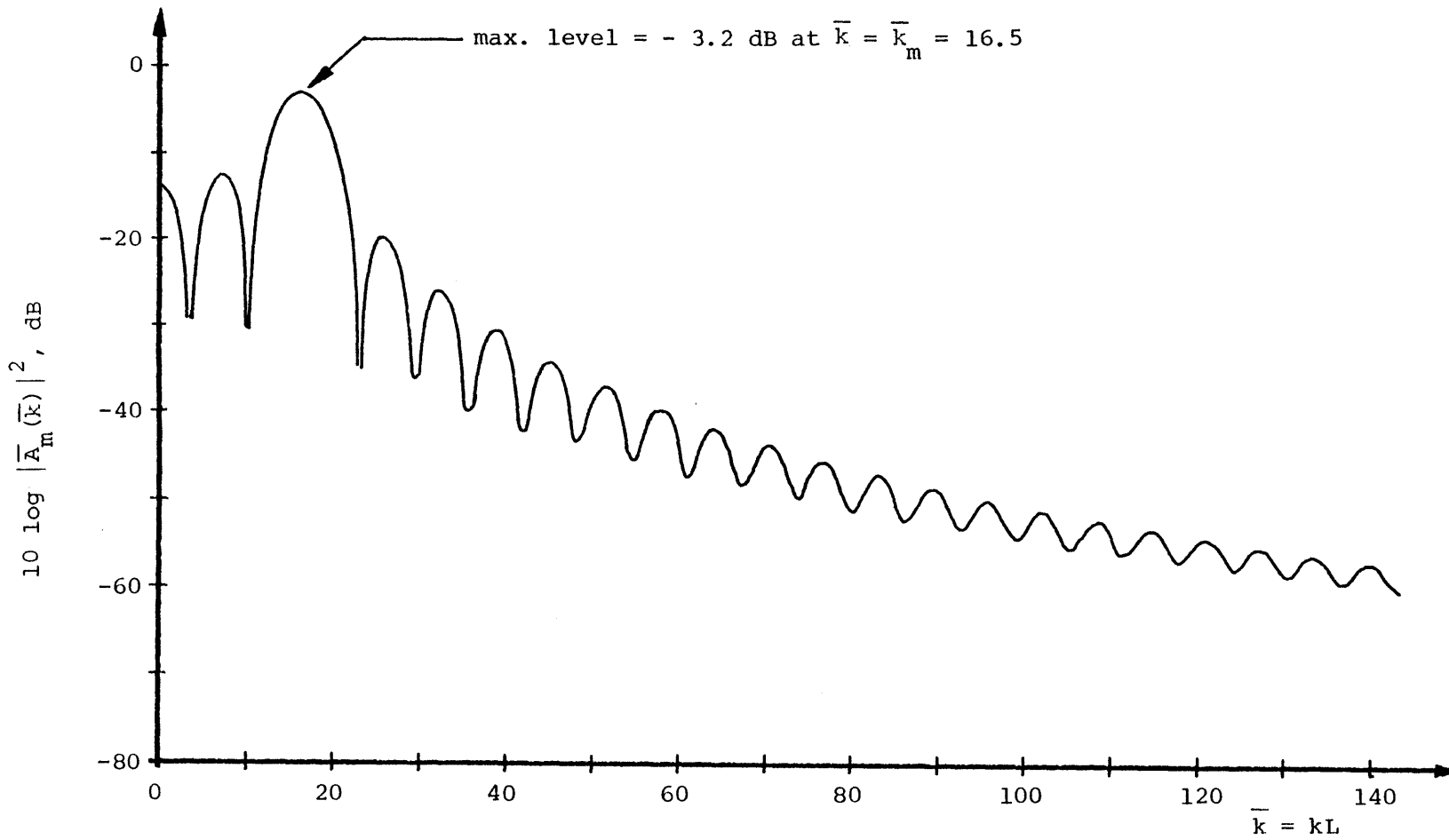


FIGURE 3.6 Wavenumber Filter Shape for a Clamped-Simple Beam ( $m = 5$ )

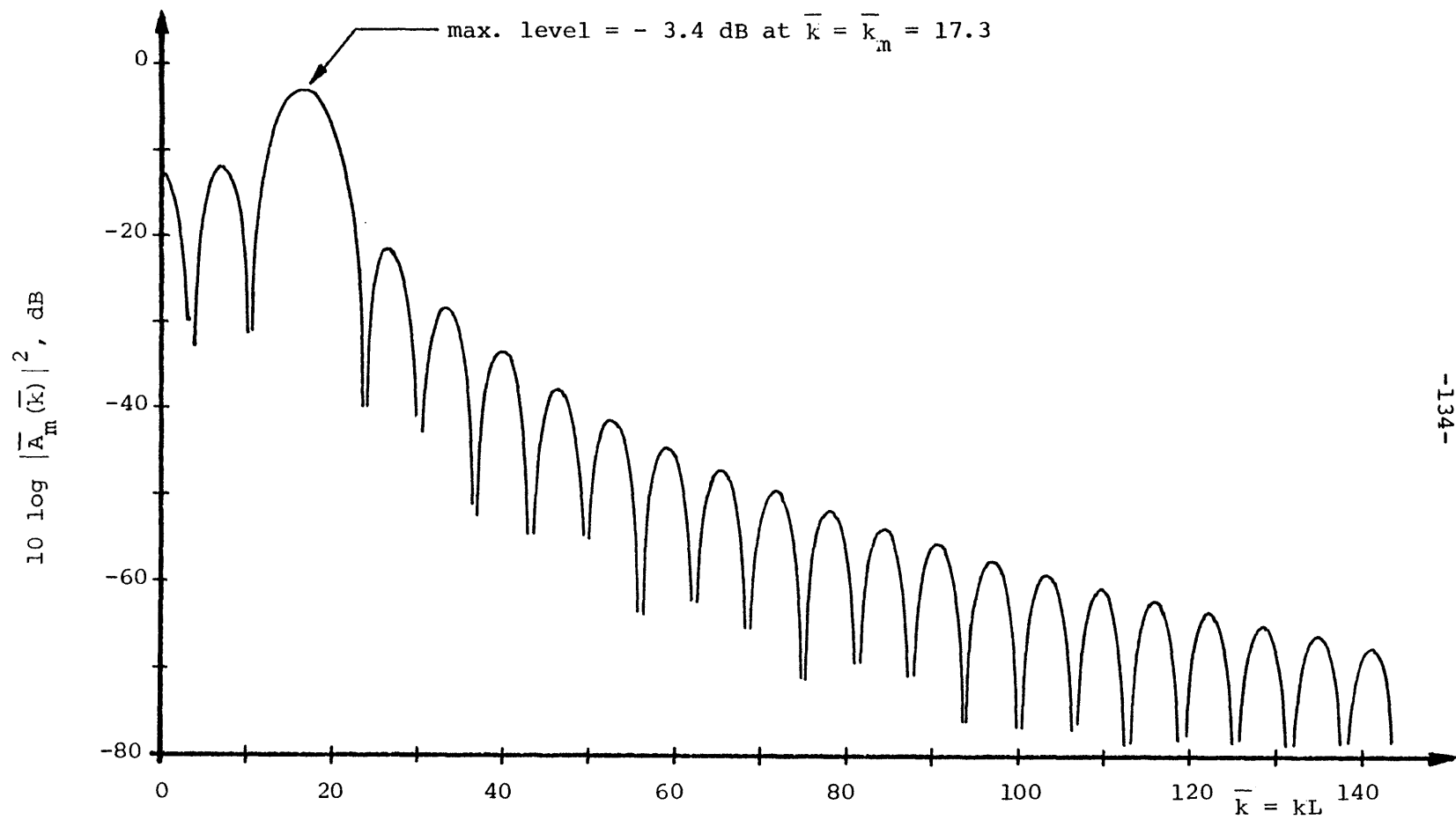


FIGURE 3.7 Wavenumber Filter Shape for a Clamped Beam ( $m = 5$ )

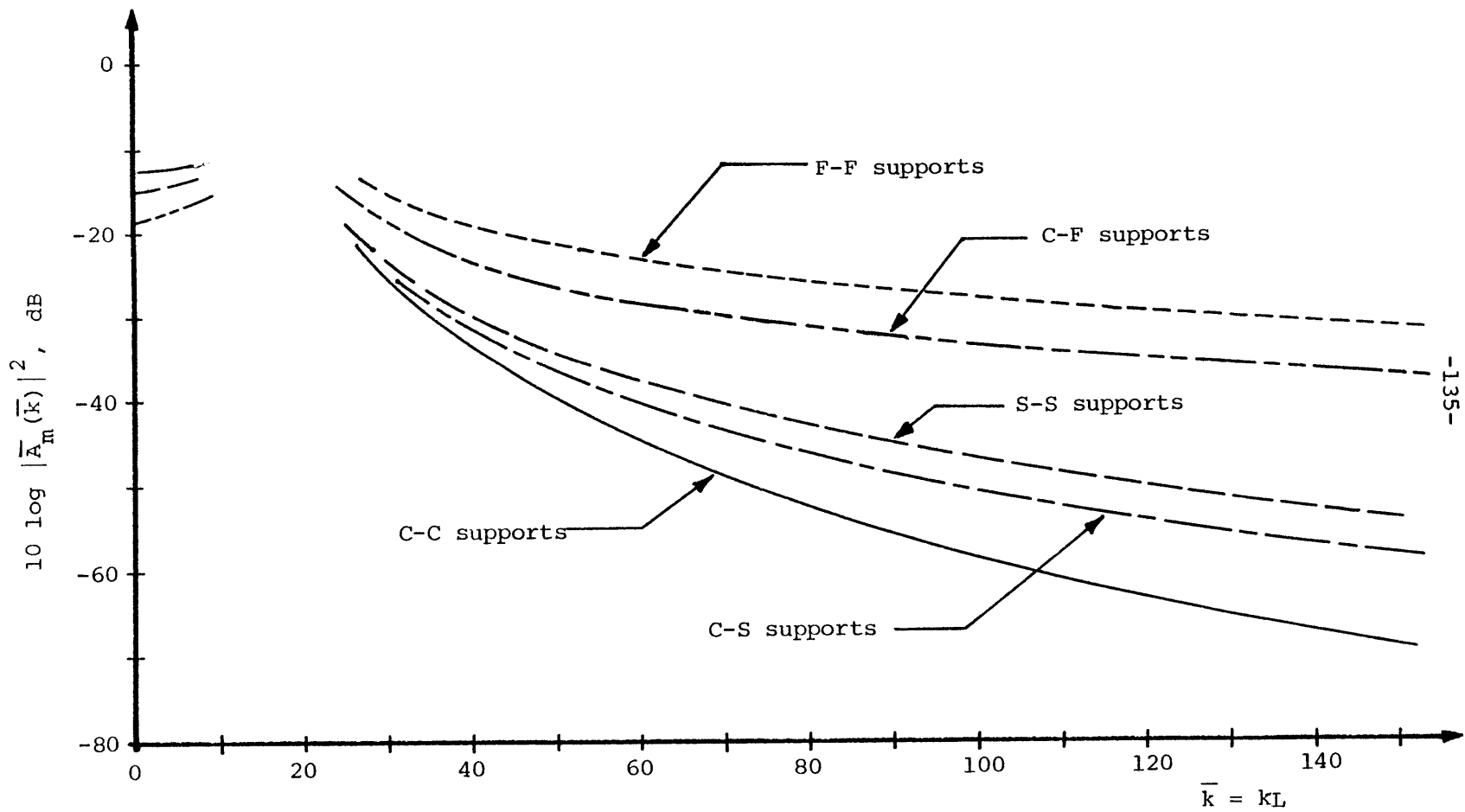


FIGURE 3.8 A Comparison of the Decay of Side Lobe Peak Levels for Beams With Various End Supports ( $m = 5$ )



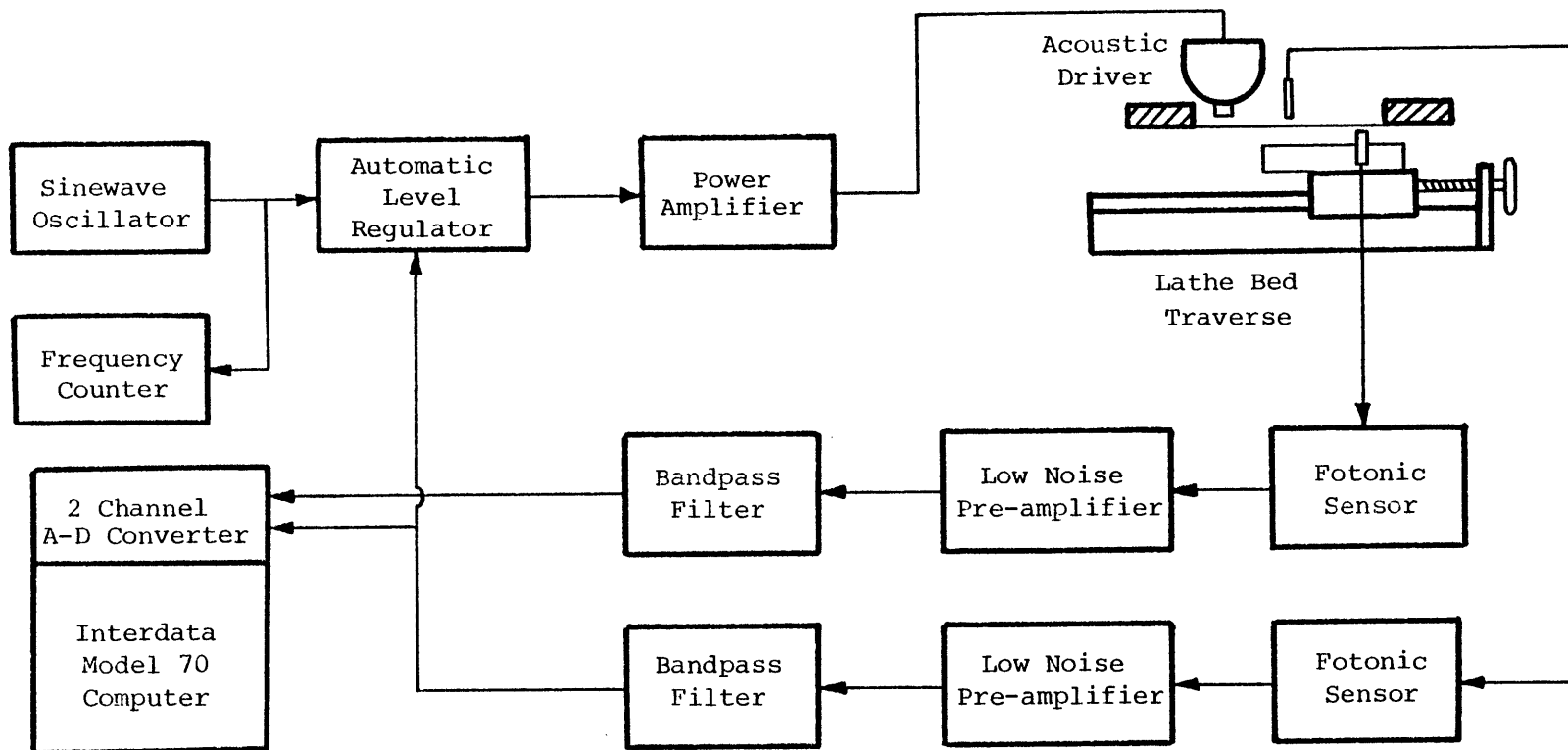
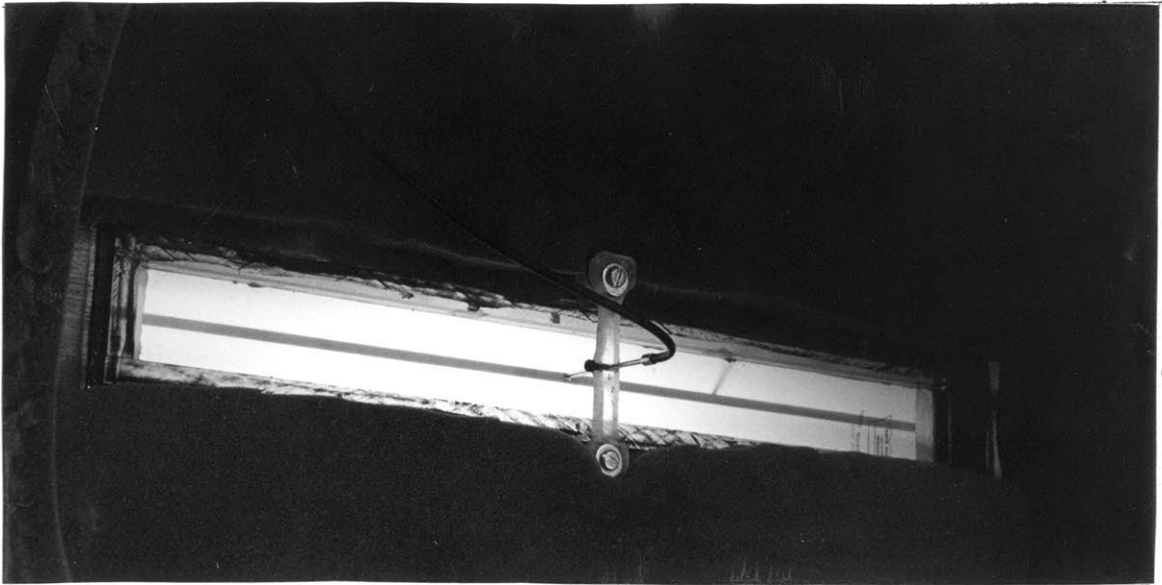
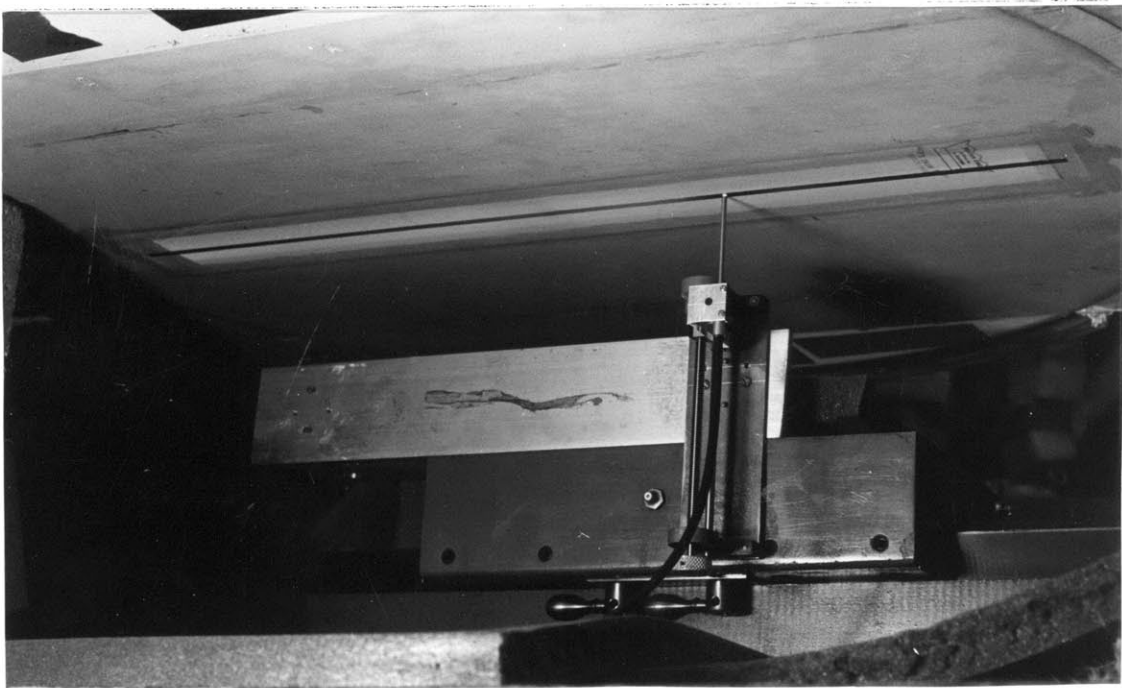


FIGURE 4.1 Experimental Setup for Mode Shape Measurements

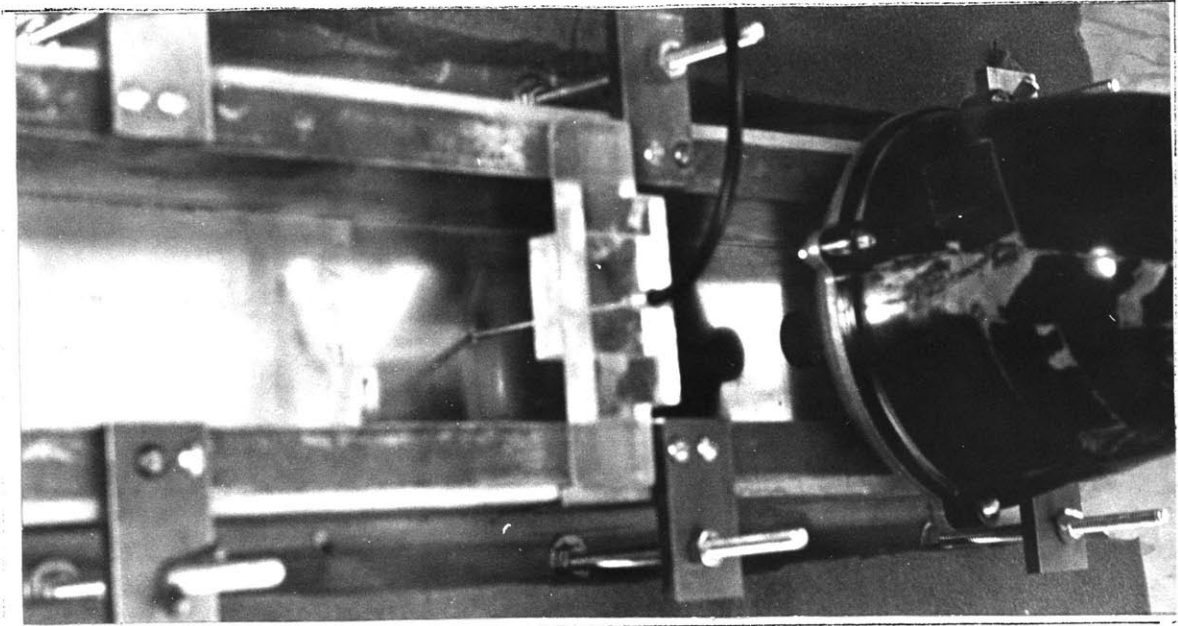


a. Fixed Sensor at Membrane Center

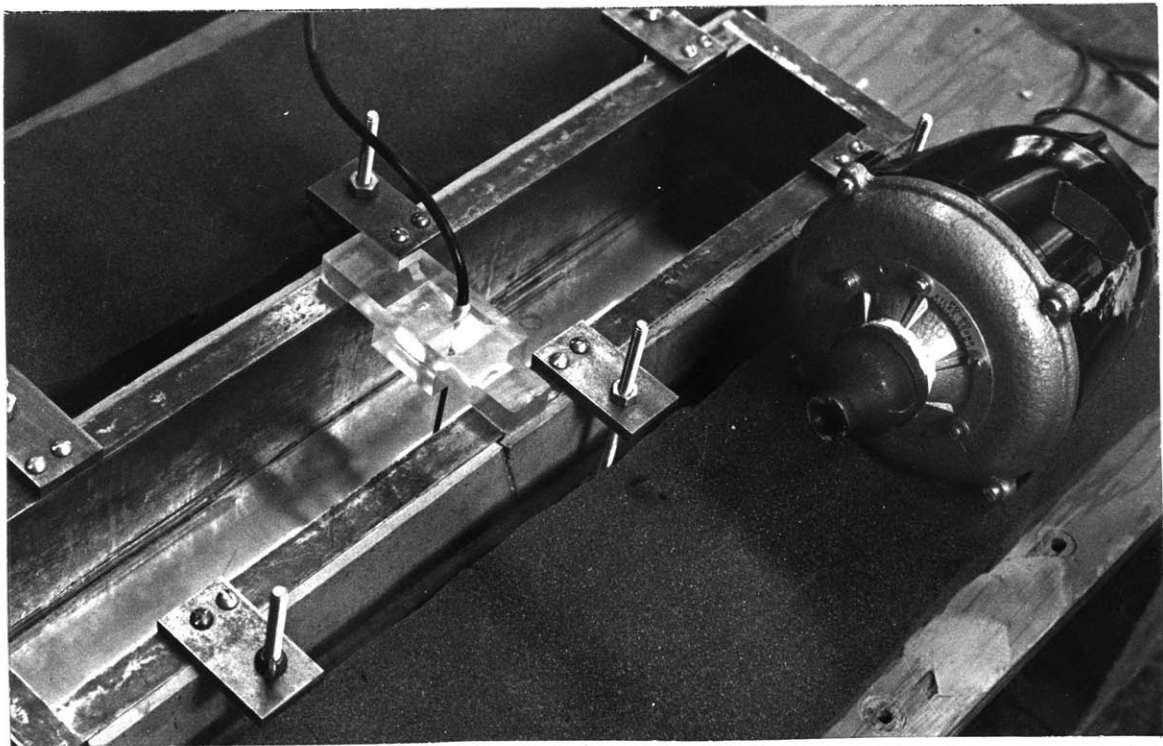


b. Traversing Sensor

FIGURE 4.2 Apparatus for Mode Shape Measurement



a. Driver Positioned at Antinode of (9,1) Mode for Clamped Plate



b. View of Pipe Fitting Used to Reduce the Drive Area

FIGURE 4.3 The Small Area Acoustic Drive

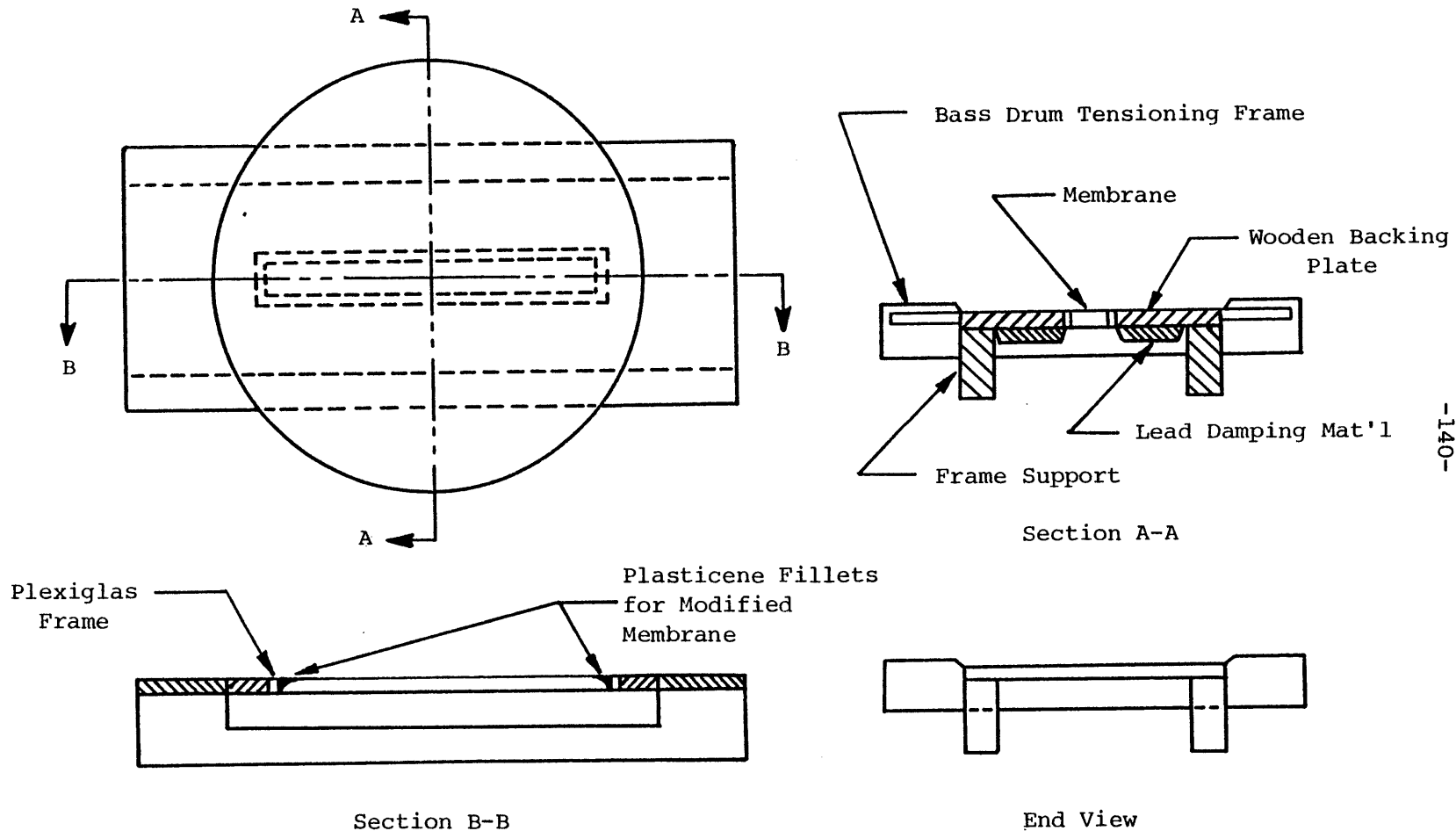


FIGURE 4.4 Membrane Construction Details

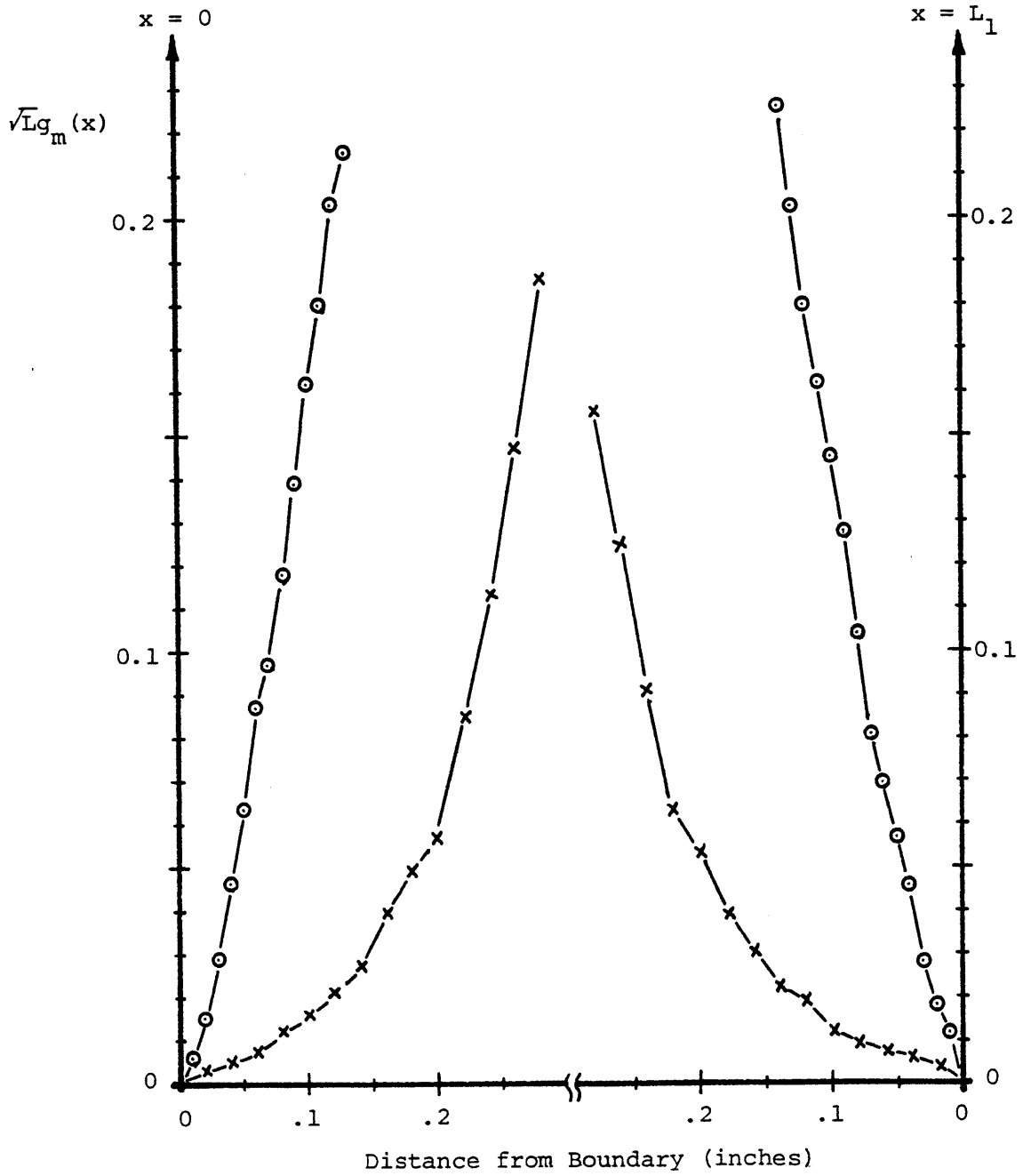
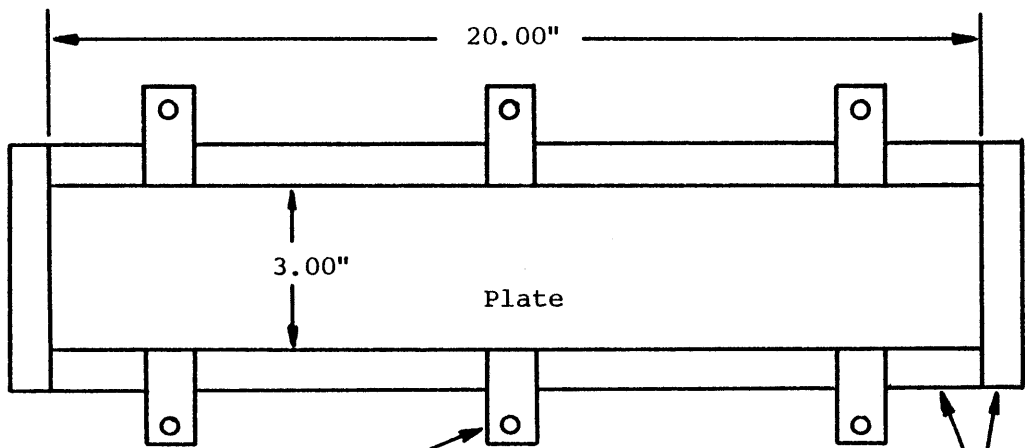
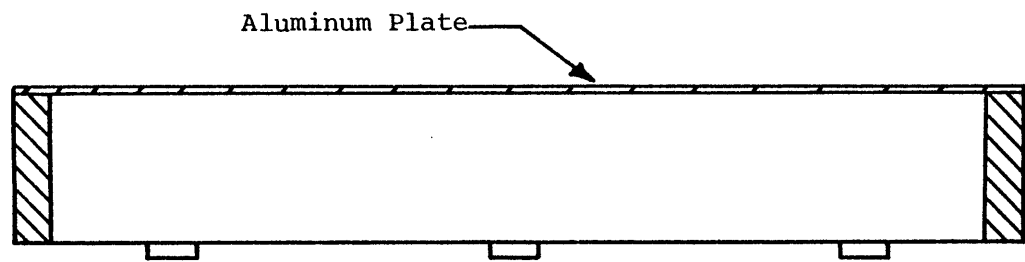


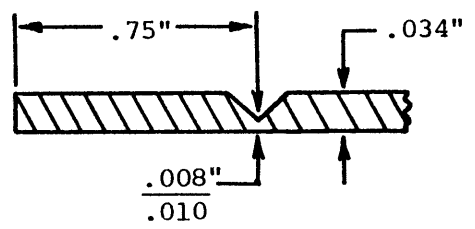
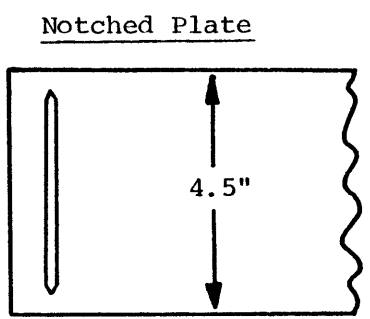
FIGURE 4.5 Detailed Membrane Mode Shapes Near The Boundaries: (11,1) Mode; x-x Modified Membrane, o-o Standard Membrane



Bottom View



Cut-Away Side View



Detail of Notch

FIGURE 4.6 Plate Construction Details

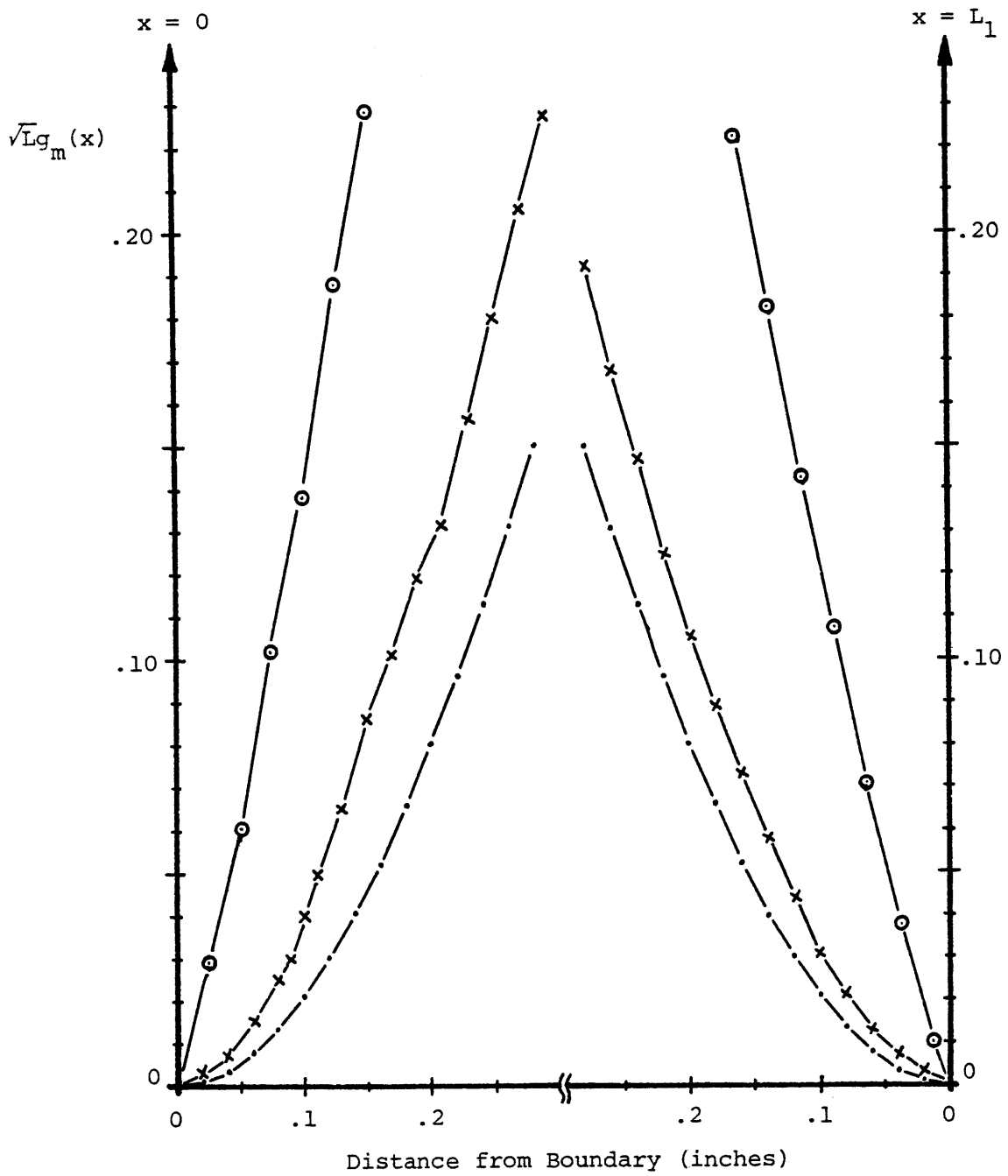


FIGURE 4.7 Detailed Plate Mode Shapes Near the Boundaries, (9,1) Mode, x-x Clamped Plate, O-O S-C-S-C Plate, ·-· Idealized Clamped Beam.

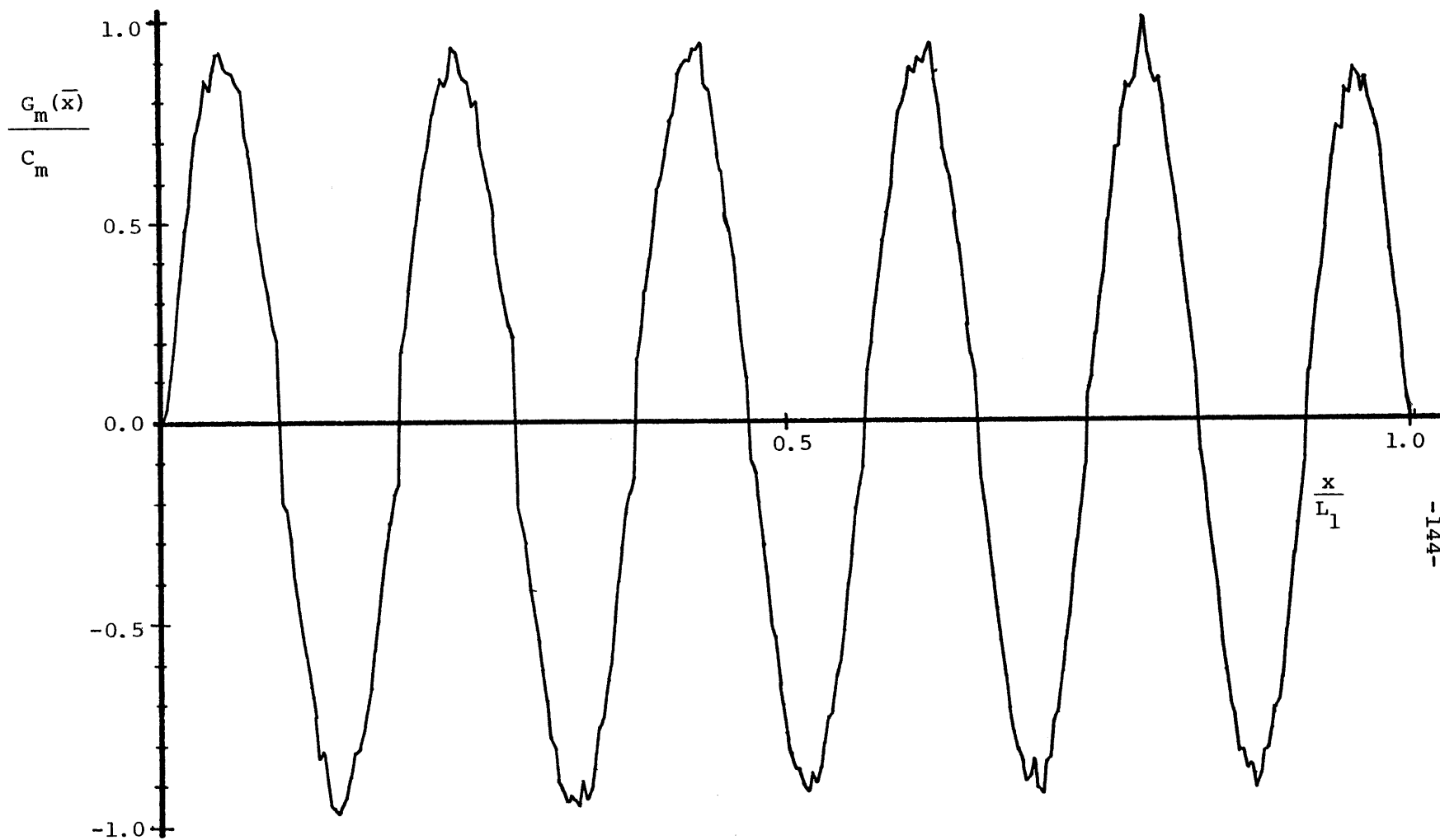


FIGURE 4.8 Measured Mode Shape: (11,1) Mode of Standard Membrane



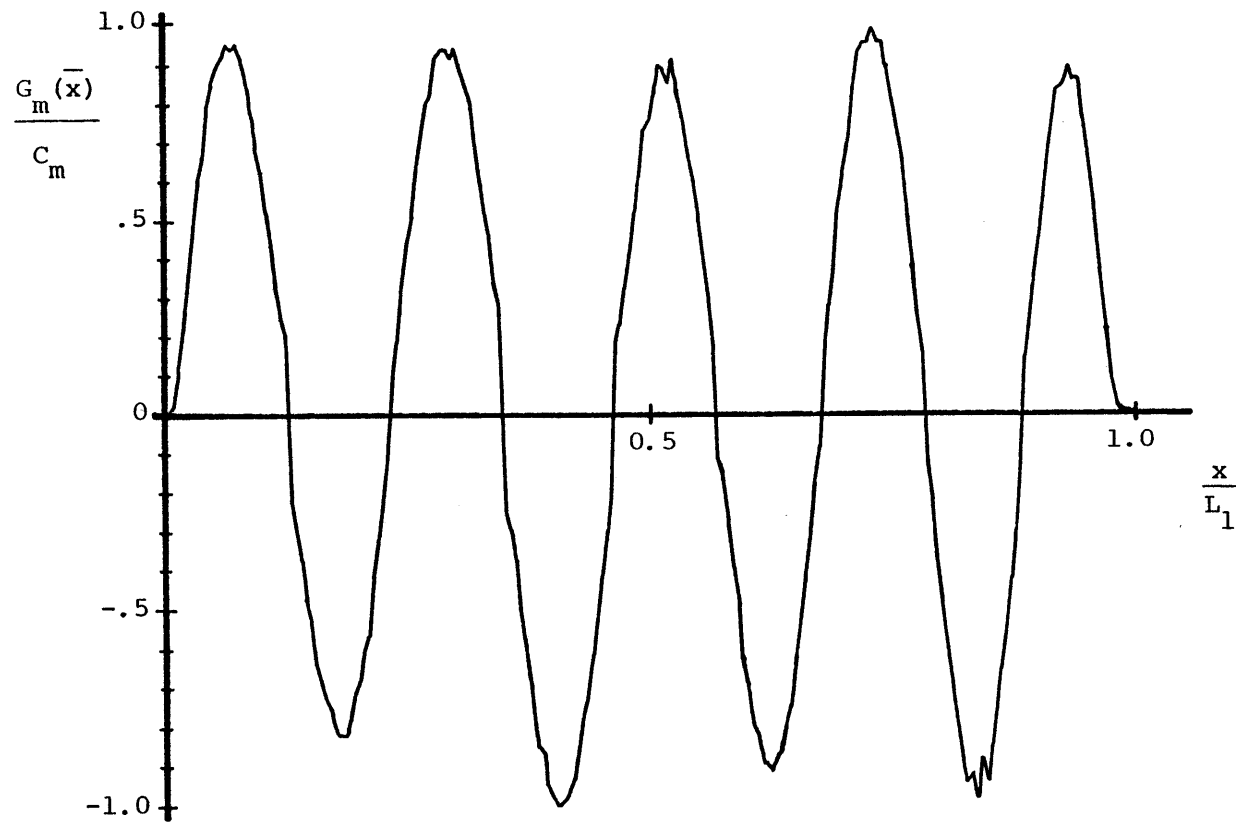


FIGURE 4.9 Measured Mode Shape: (9,1) Mode of Modified Membrane

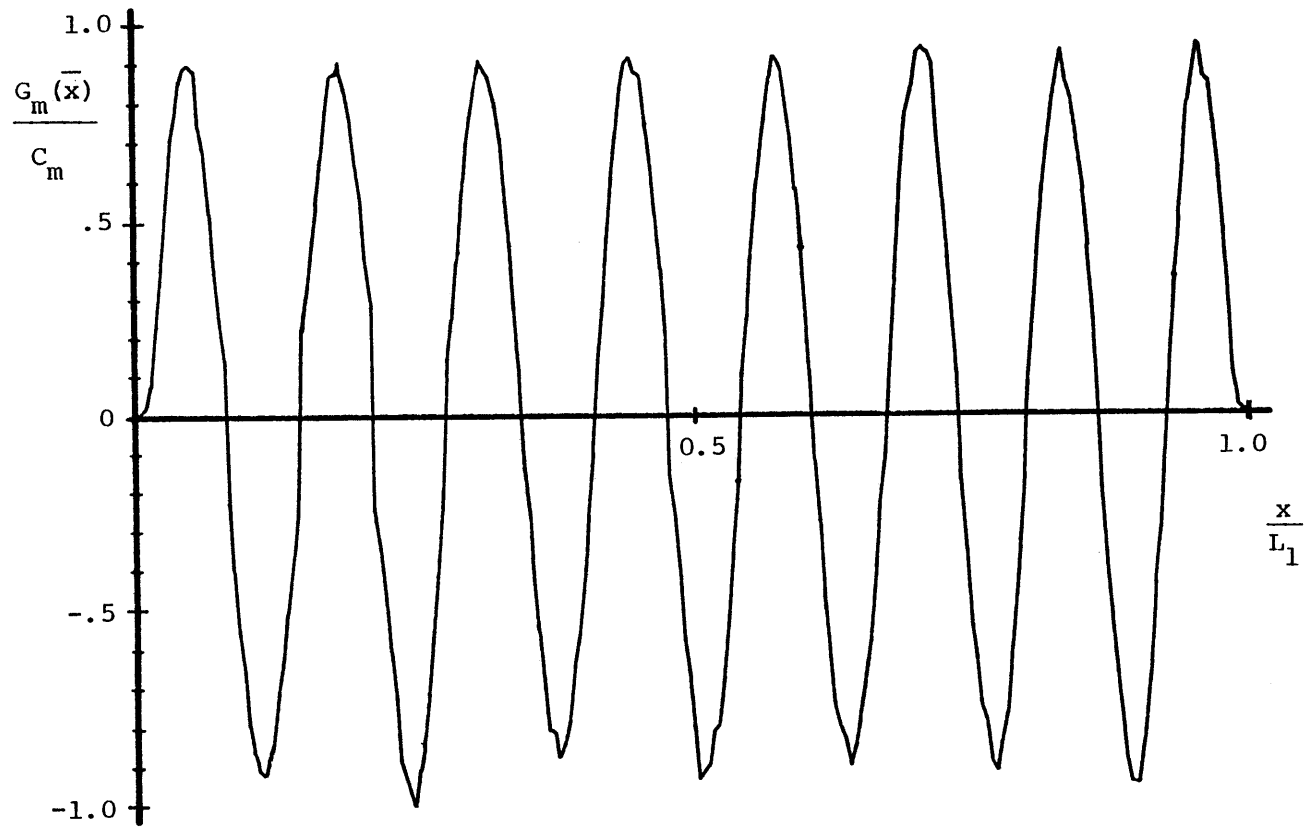


FIGURE 4.10 Measured Mode Shape: (15,1) Mode of Modified Membrane

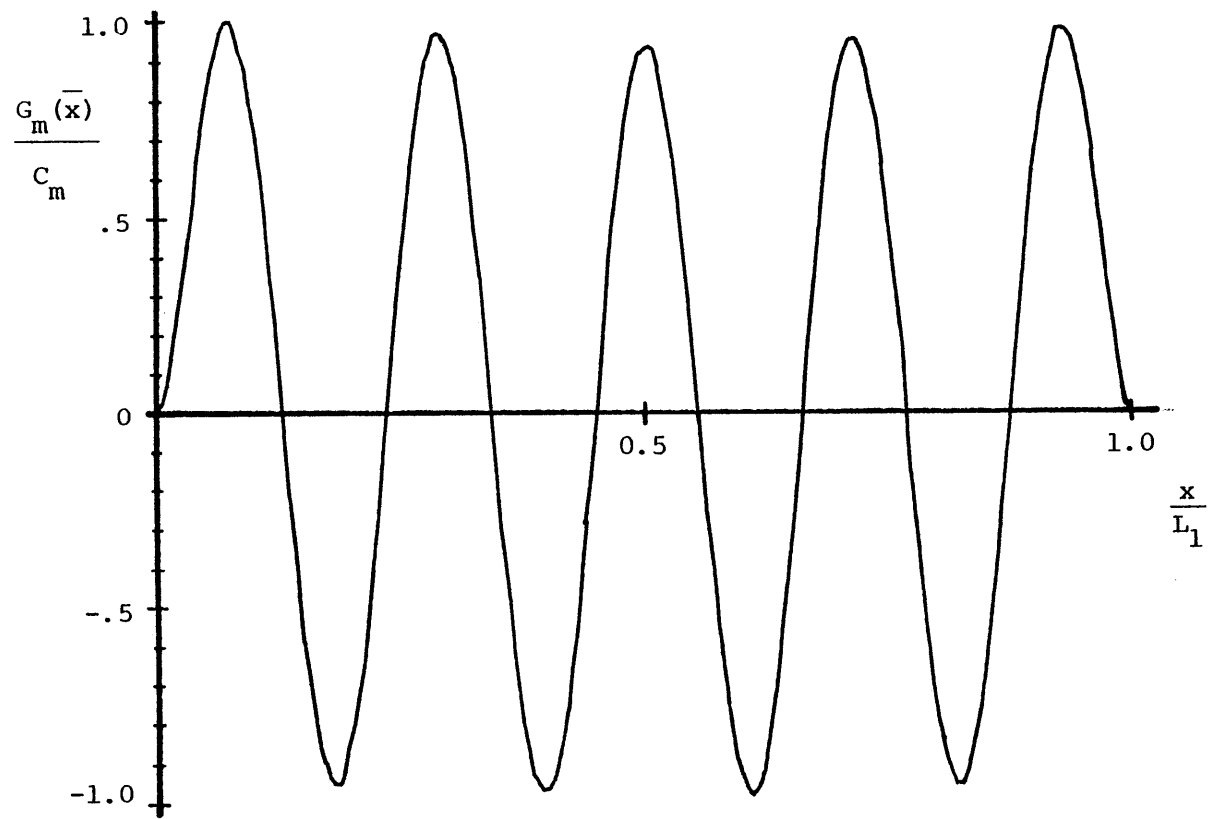


FIGURE 4.11 Measured Mode Shape: (9,1) Mode of Clamped Plate

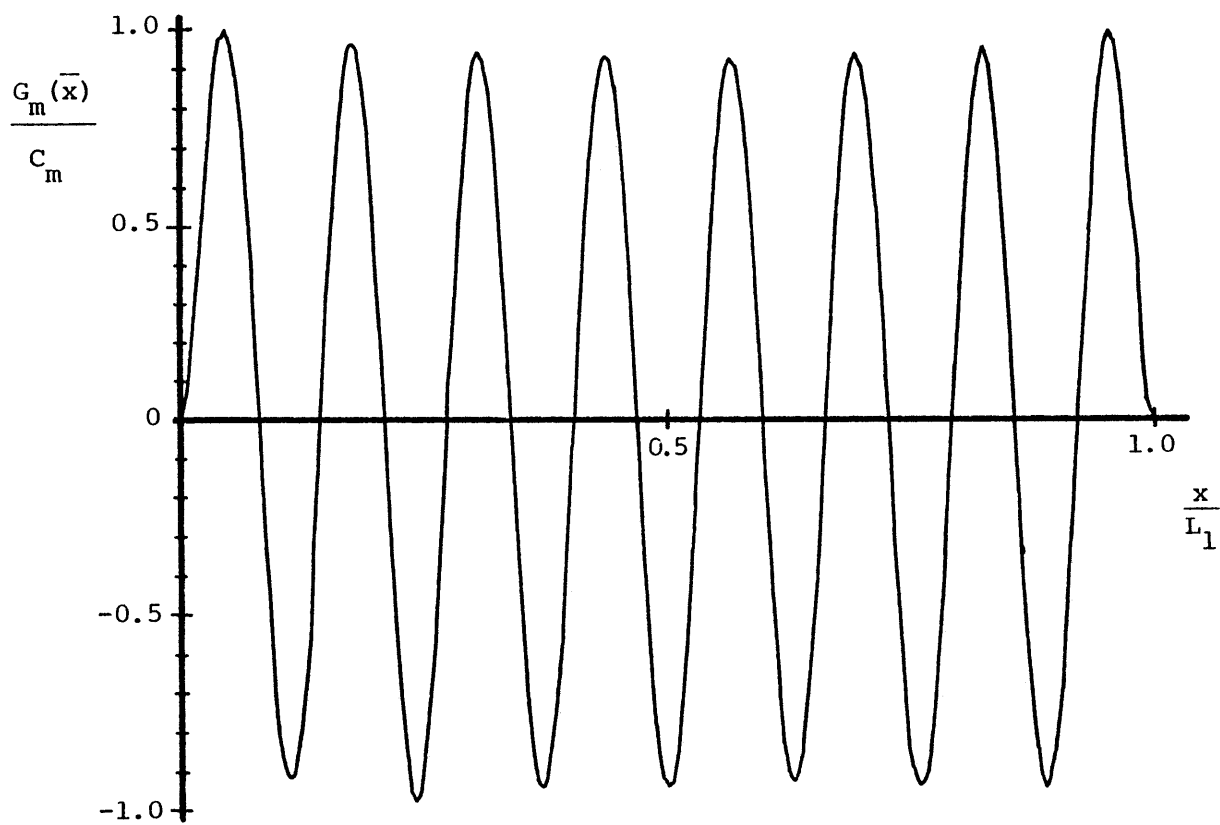


FIGURE 4.12 Measured Mode Shape: (15,1) Mode of Clamped Plate

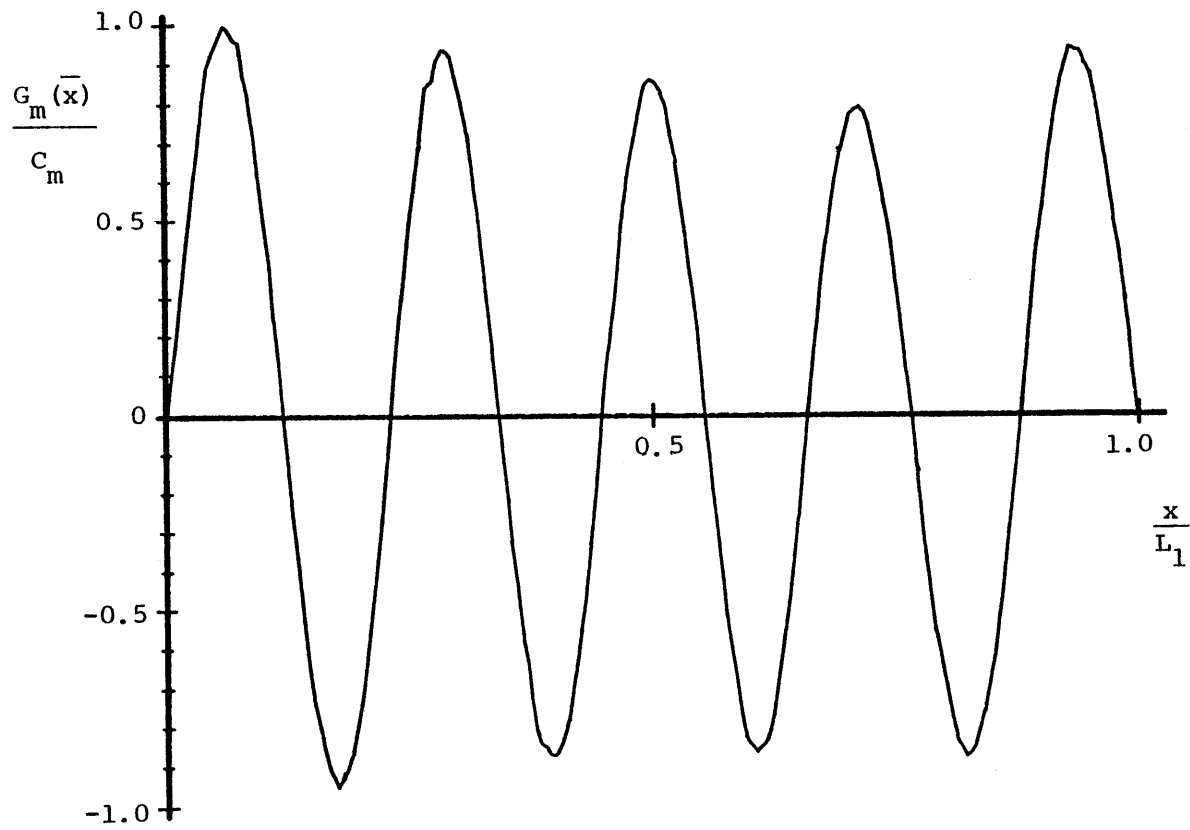


FIGURE 4.13 Measured Mode Shape: (9,1) Mode of S-C-S-C Plate

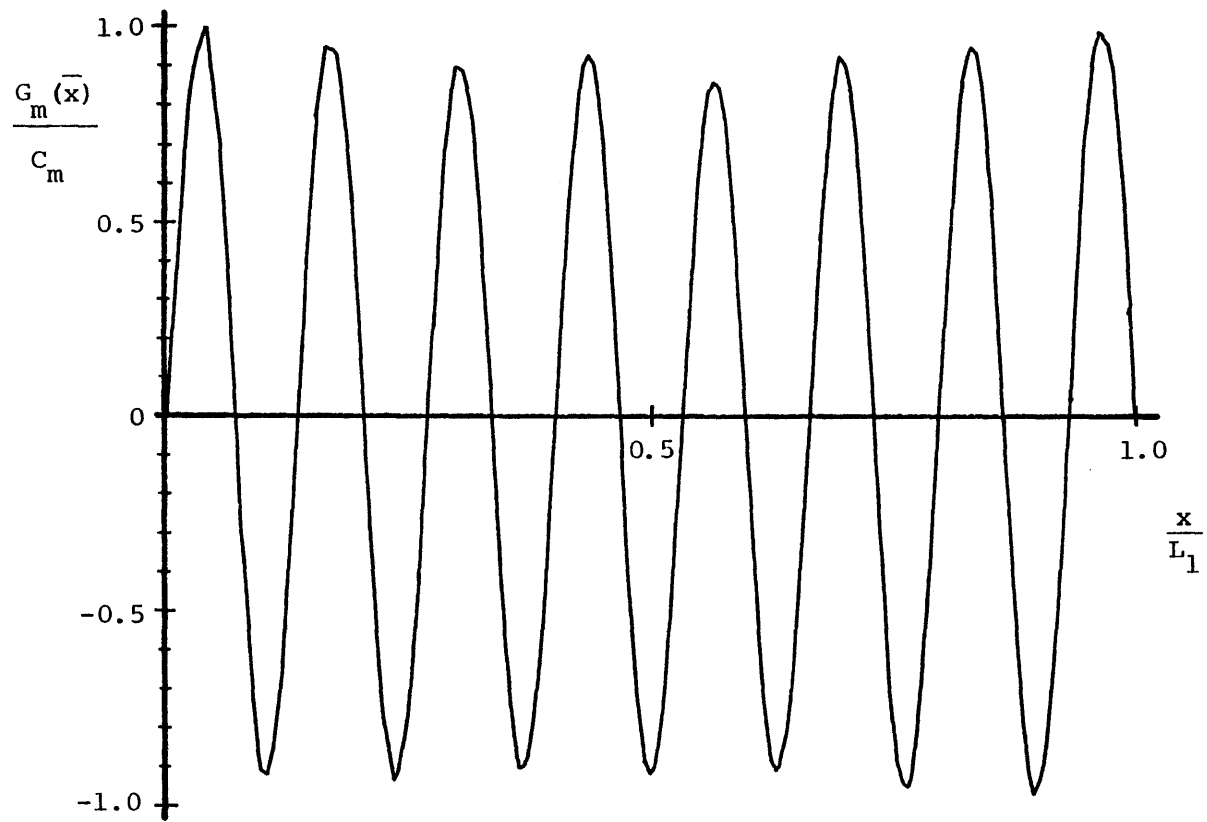


FIGURE 4.14 Measured Mode Shape: (15,1) Mode of S-C-S-C Plate

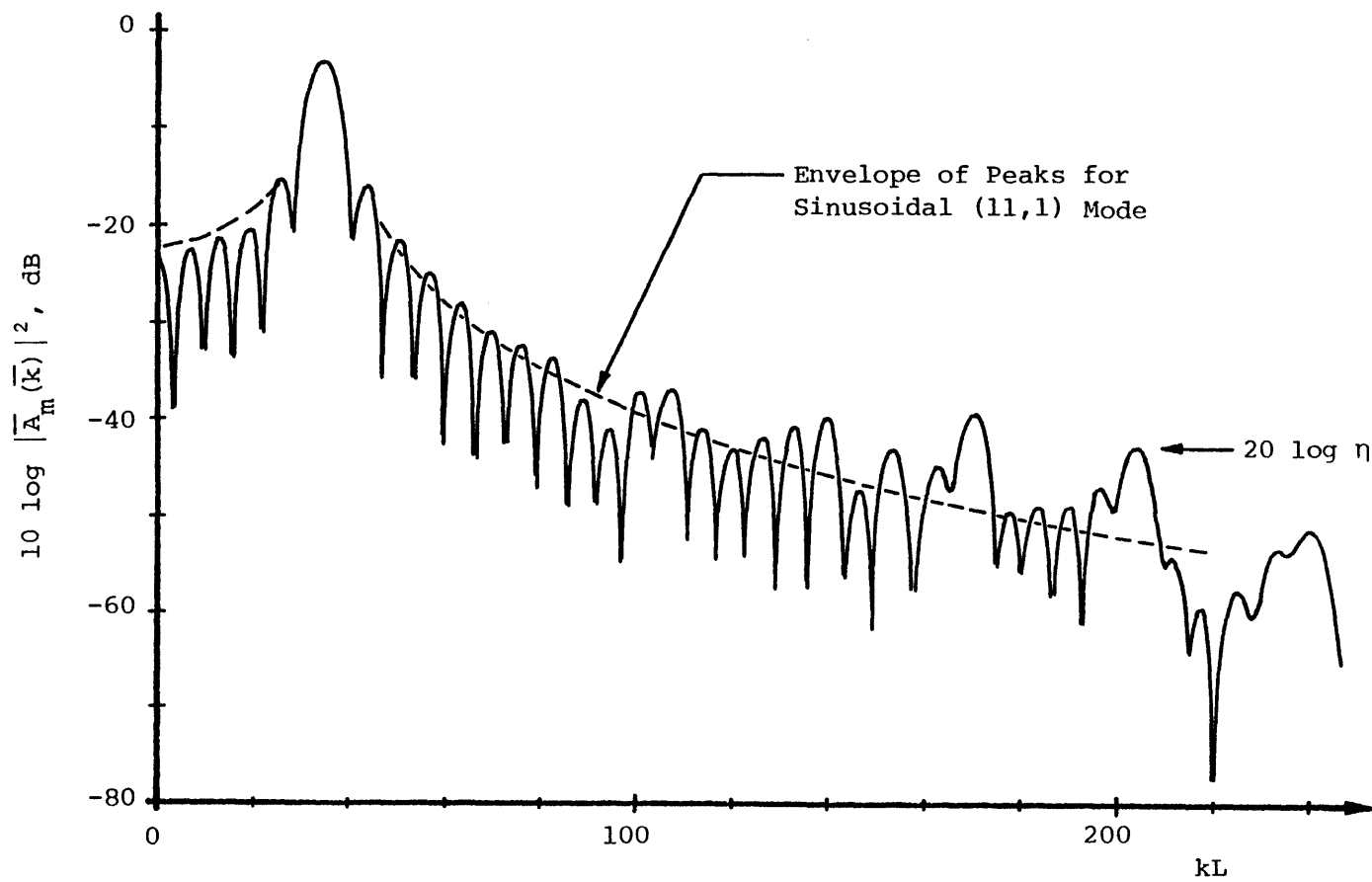


FIGURE 4.15 Measured  $|\bar{A}_m(\bar{k})|^2$ : (11,1) Mode of Standard Membrane

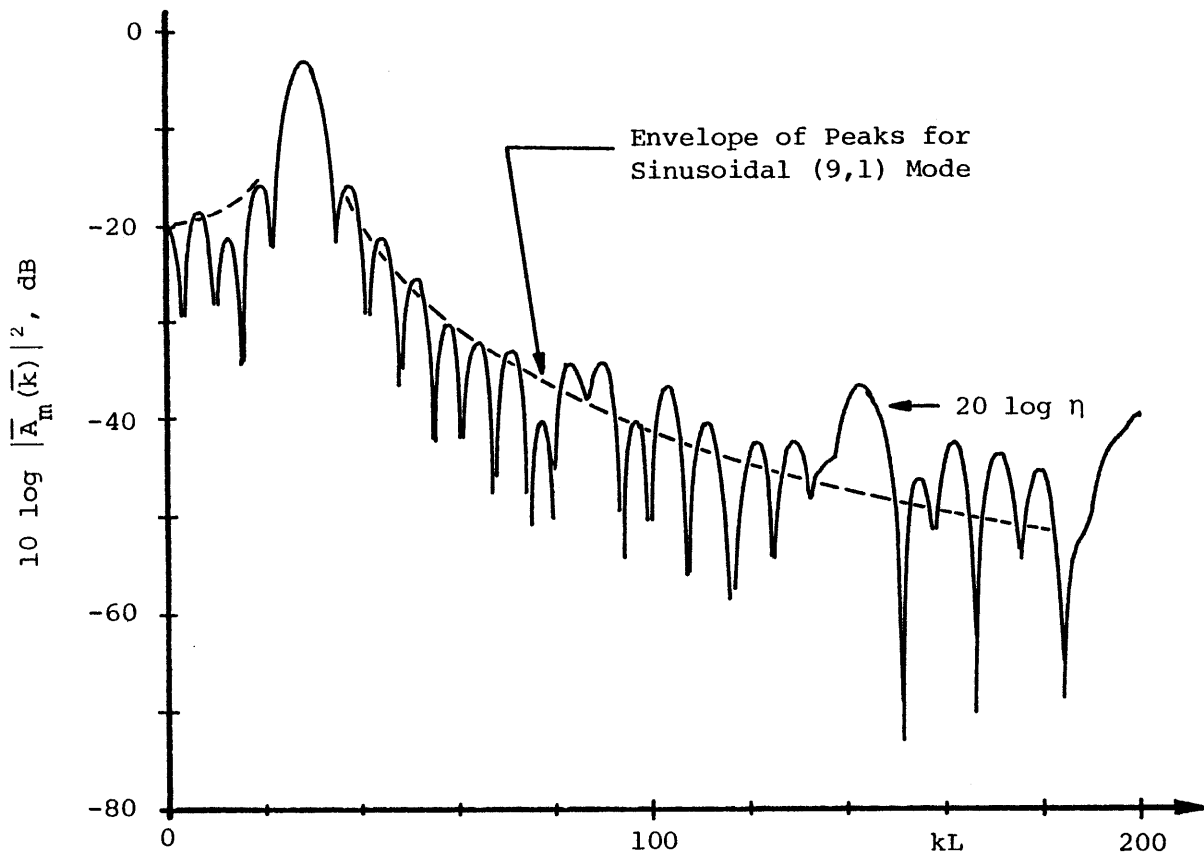


FIGURE 4.16 Measured  $|\bar{A}_m(\bar{k})|^2$ : (9,1) Mode of Modified Membrane



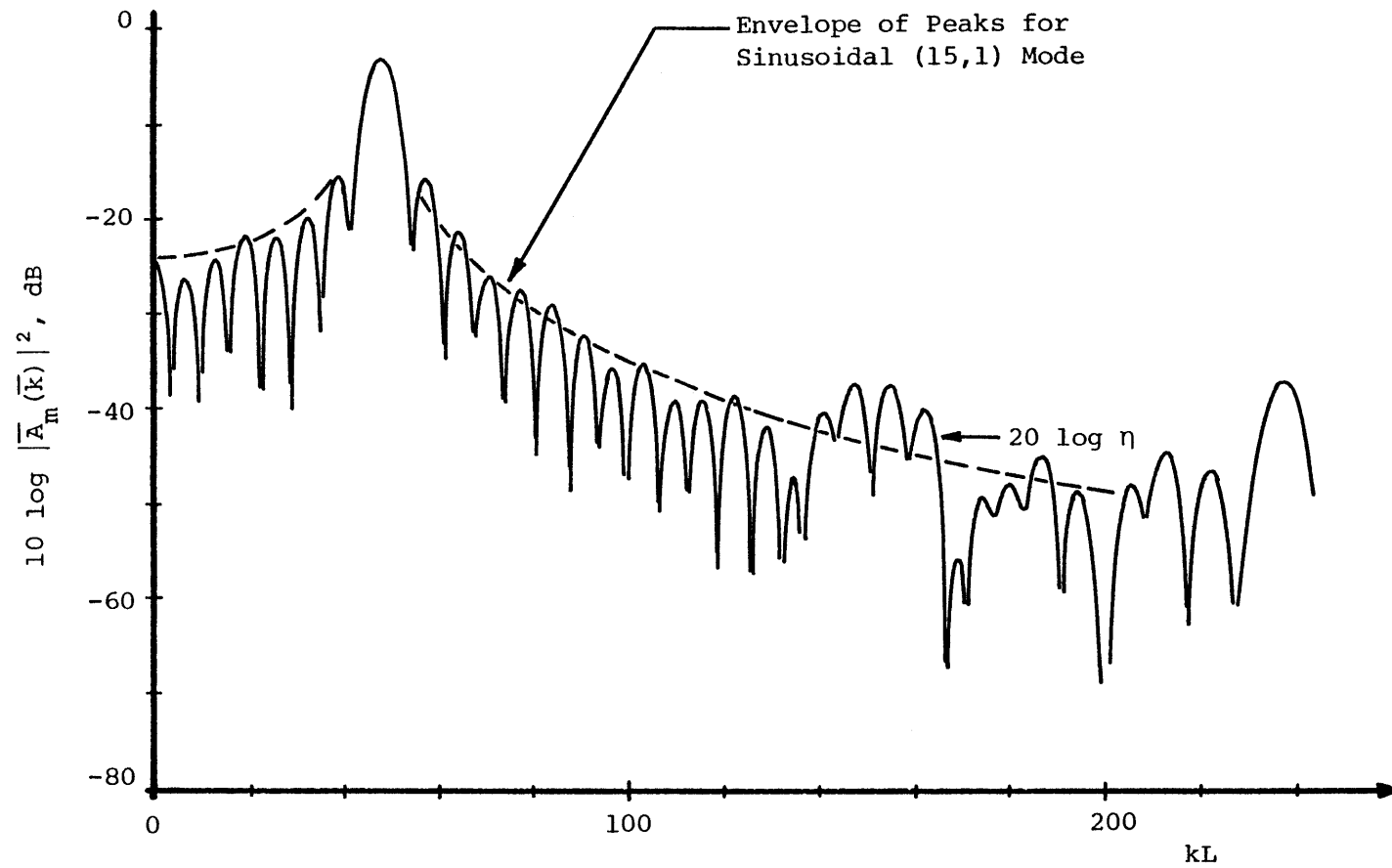
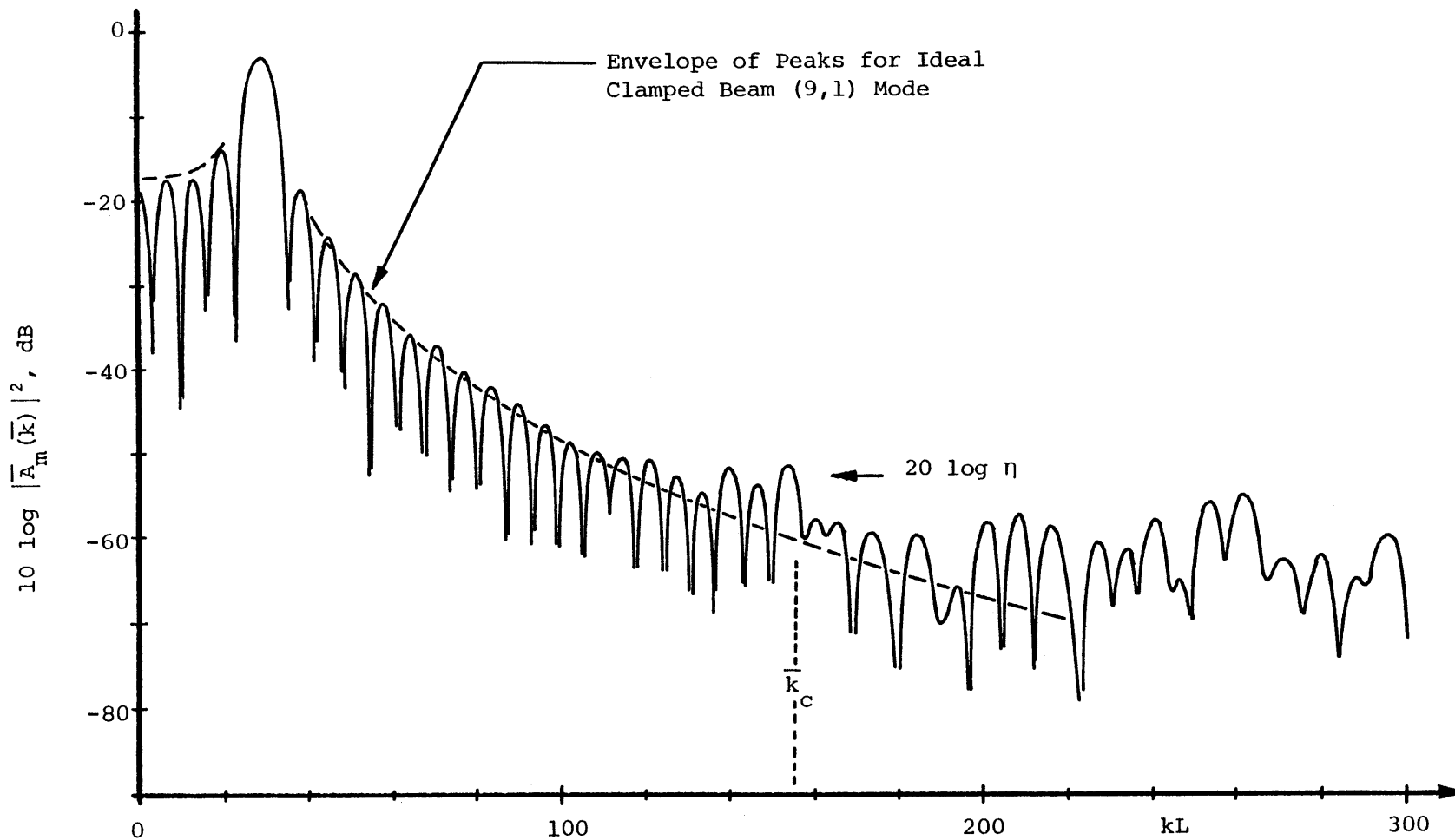
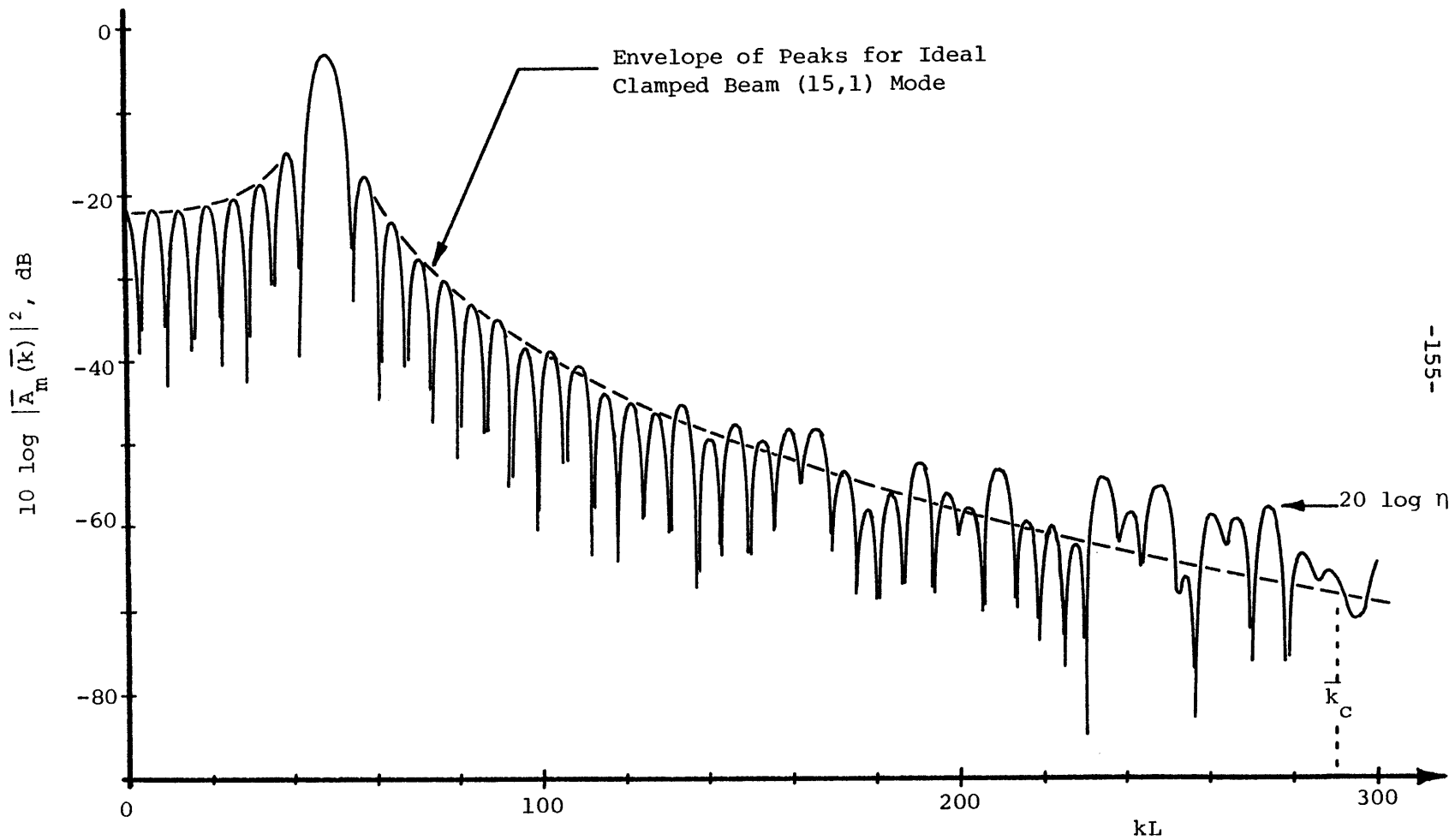


FIGURE 4.17 Measured  $|\bar{A}_m(\bar{k})|^2$ : (15,1) Mode of Modified Membrane



-154-

FIGURE 4.18 Measured  $|\bar{A}_m(\bar{k})|^2$ : (9,1) Mode of the Clamped Plate  
 $\bar{k}_c$  = Typical Convective Wavenumber ( $U_\infty = 40$  m/sec)



-155-

FIGURE 4.19 Measured  $|\bar{A}_m(\bar{k})|^2$ : (15,1) Mode of the Clamped Plate,  
 $\bar{k}_c$  = Typical Convective Wavenumber ( $U_\infty = 40$  m/sec)

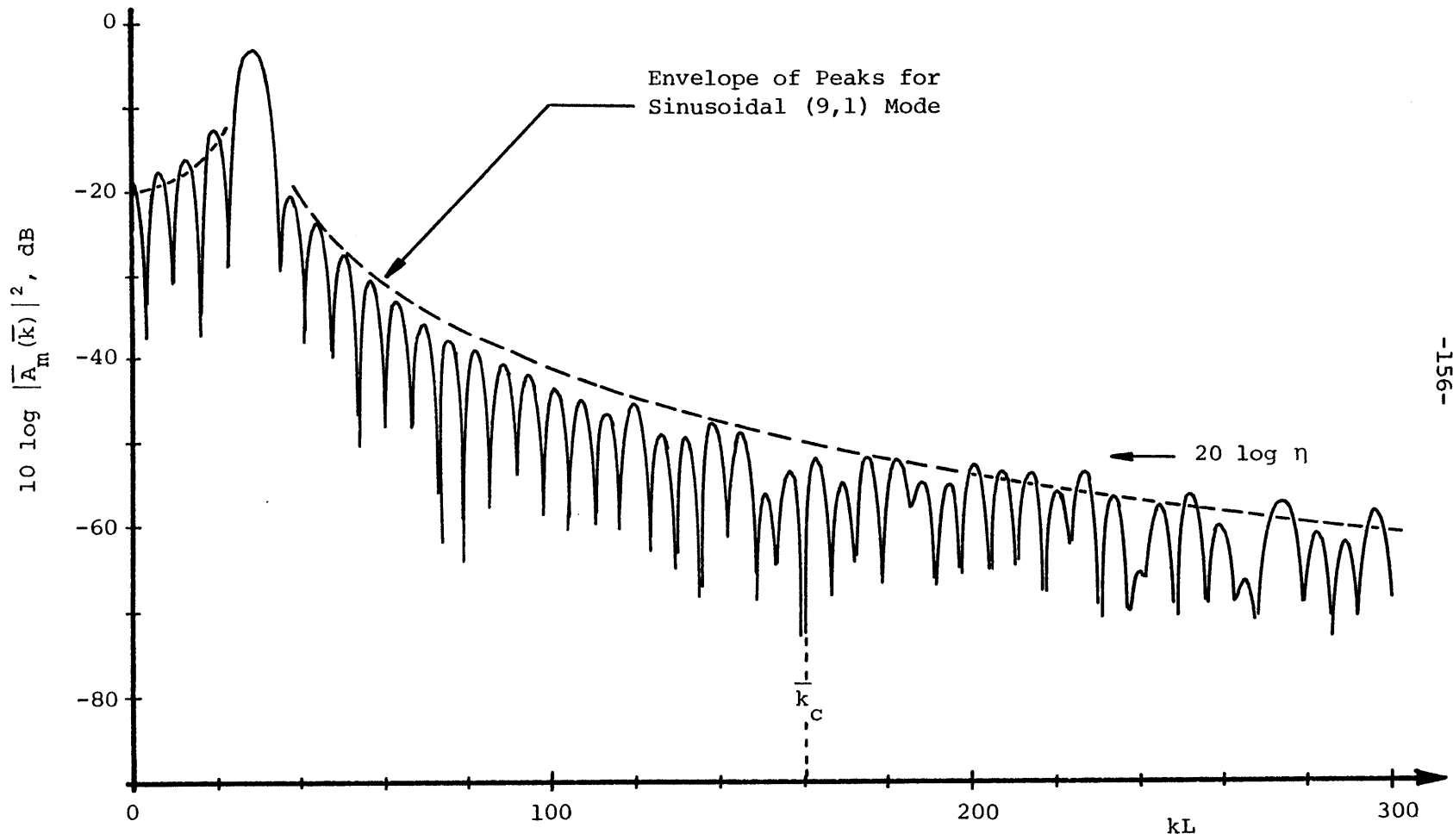


FIGURE 4.20 Measured  $|\bar{A}_m(\bar{k})|^2$ : (9,1) Mode of the S-C-S-C Plate,  
 $\bar{k}_c$  = Typical Convective Wavenumber ( $U_\infty = 40$  m/sec)

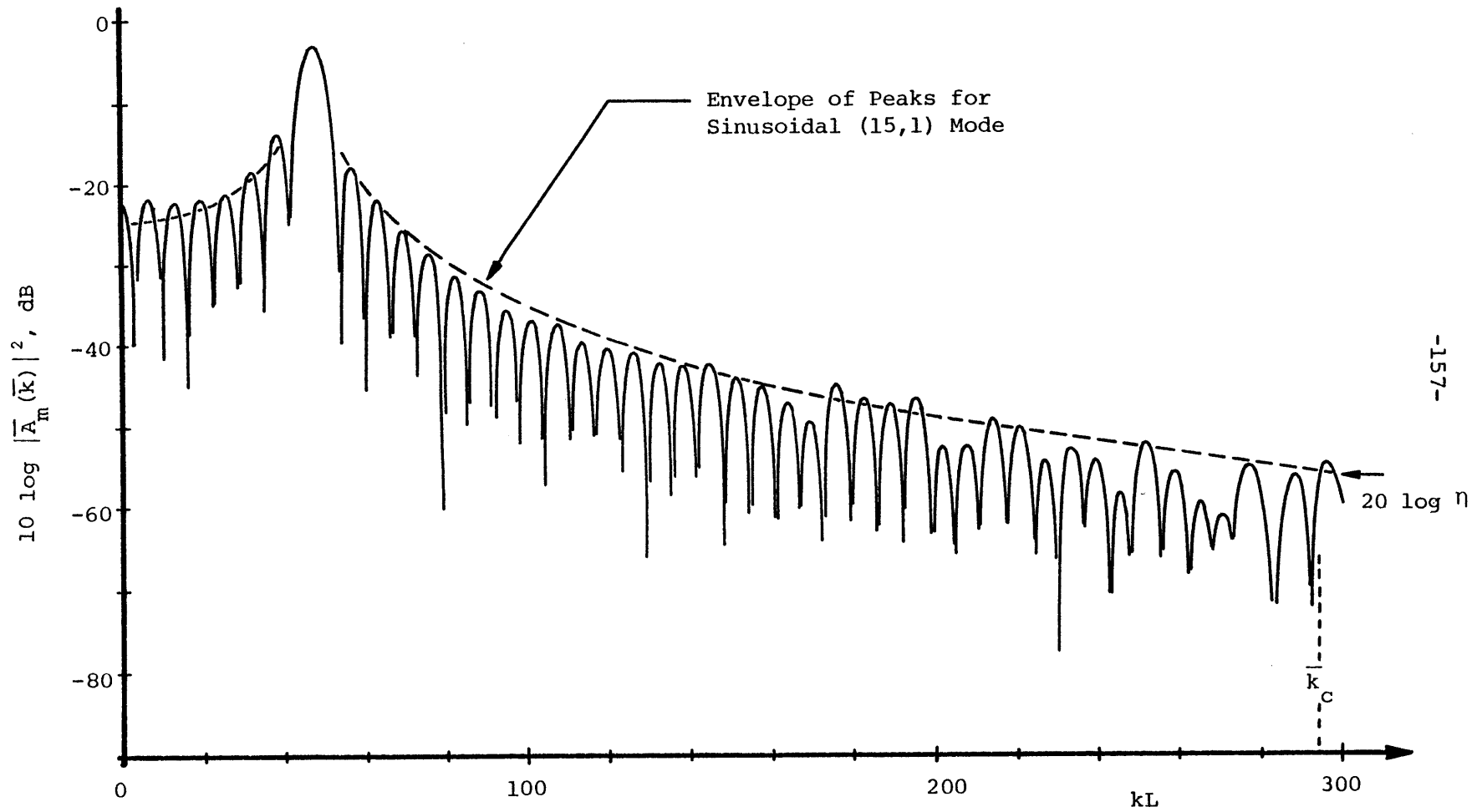


FIGURE 4.21 Measured  $|\bar{A}_m(\bar{k})|^2$ : (15,1) Mode of the S-C-S-C Plate,  
 $k_C$  = Typical Convective Wavenumber ( $U_\infty = 40$  m/sec)

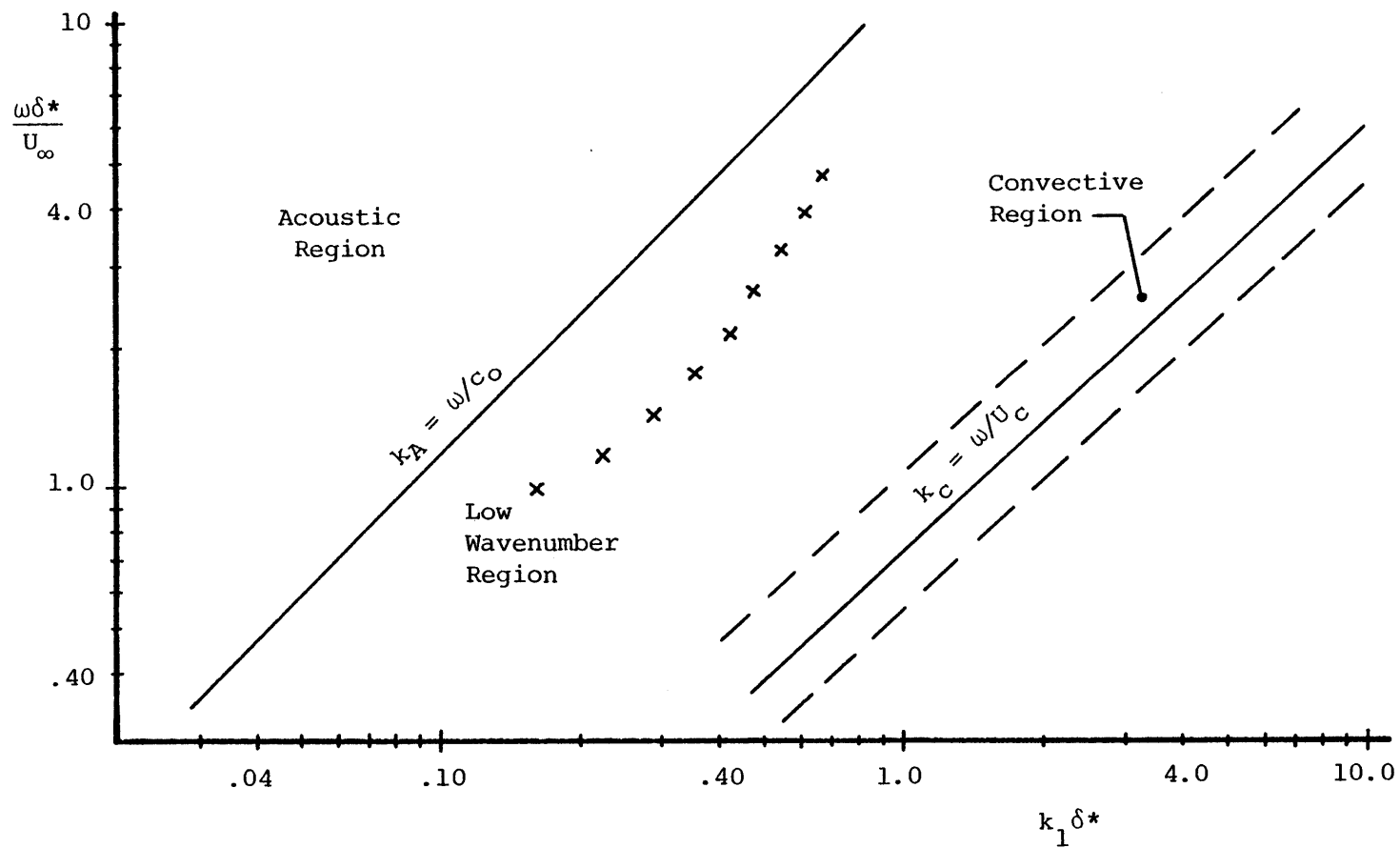


FIGURE 5.1 Wavenumber-Frequency Location of Various Excitations,  $U_\infty = 29$  m/sec,  $c_0 = 343$  m/sec, x = S-C-S-C Plate Mode Locations

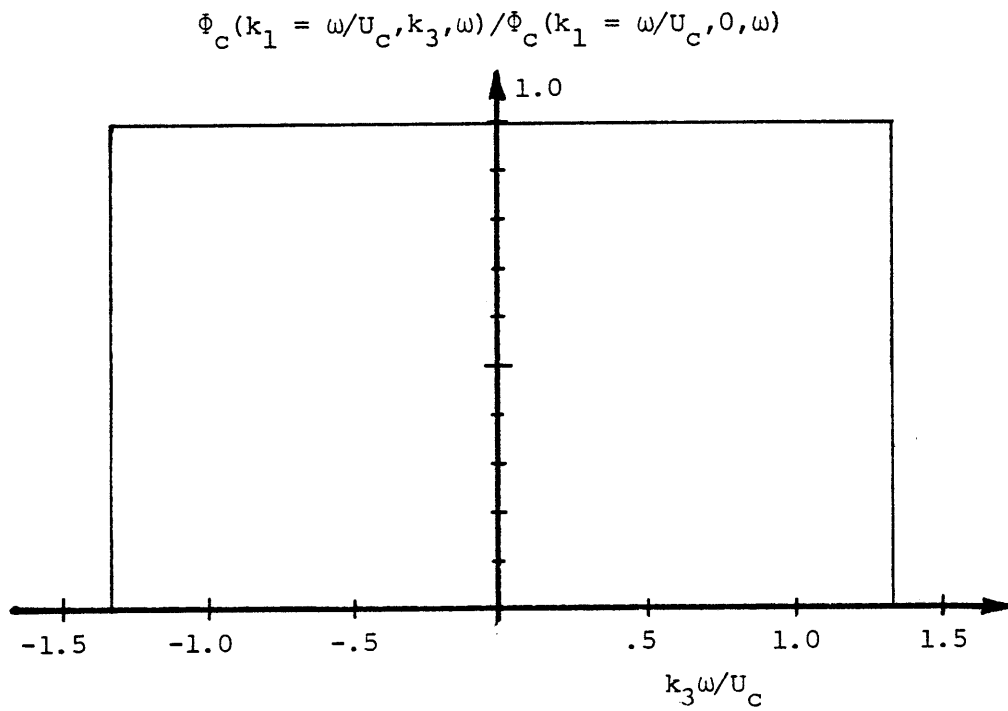
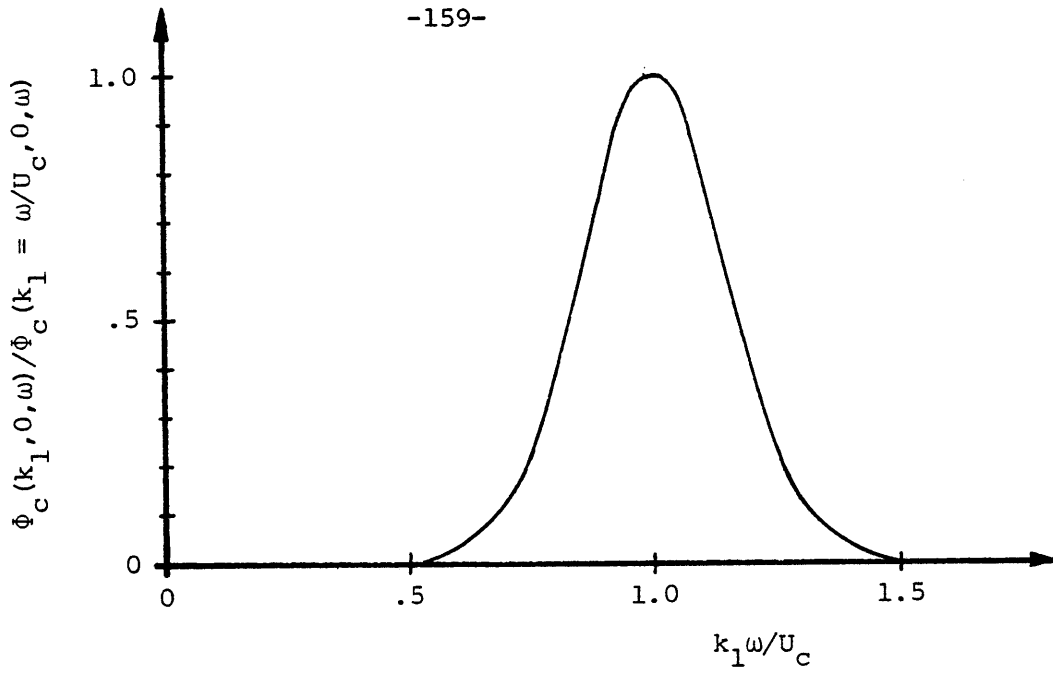


FIGURE 5.2 The Normal Distribution Model of the Convective Spectrum  $\Phi_C(k_1, k_3, \omega)$

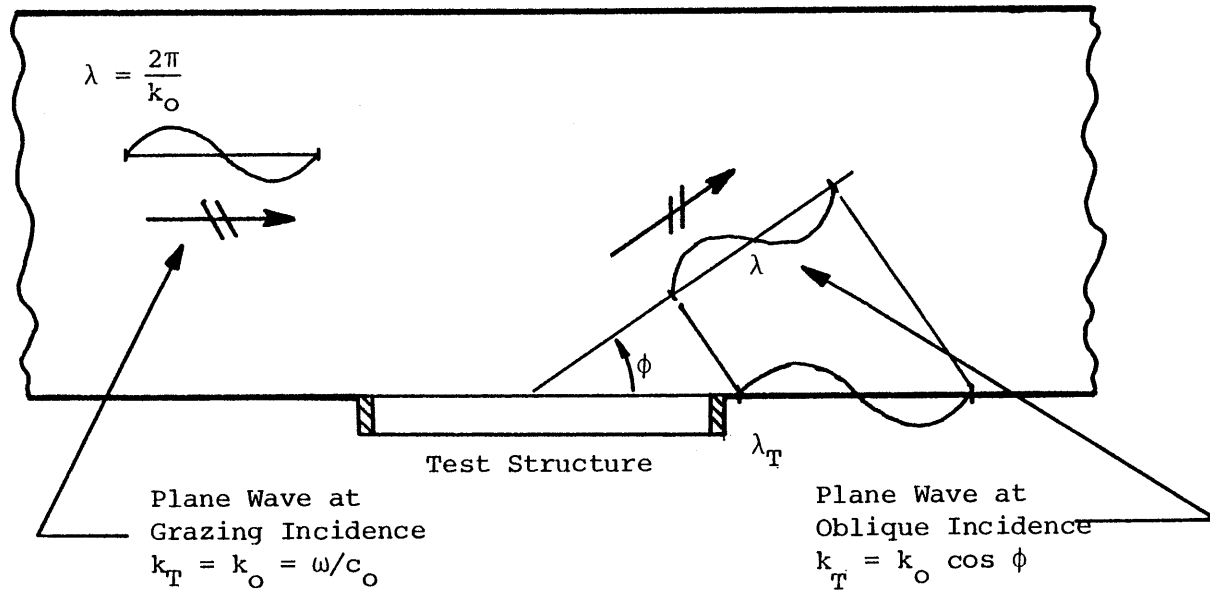


FIGURE 5.3 Geometrical Considerations for Acoustic Response Estimates



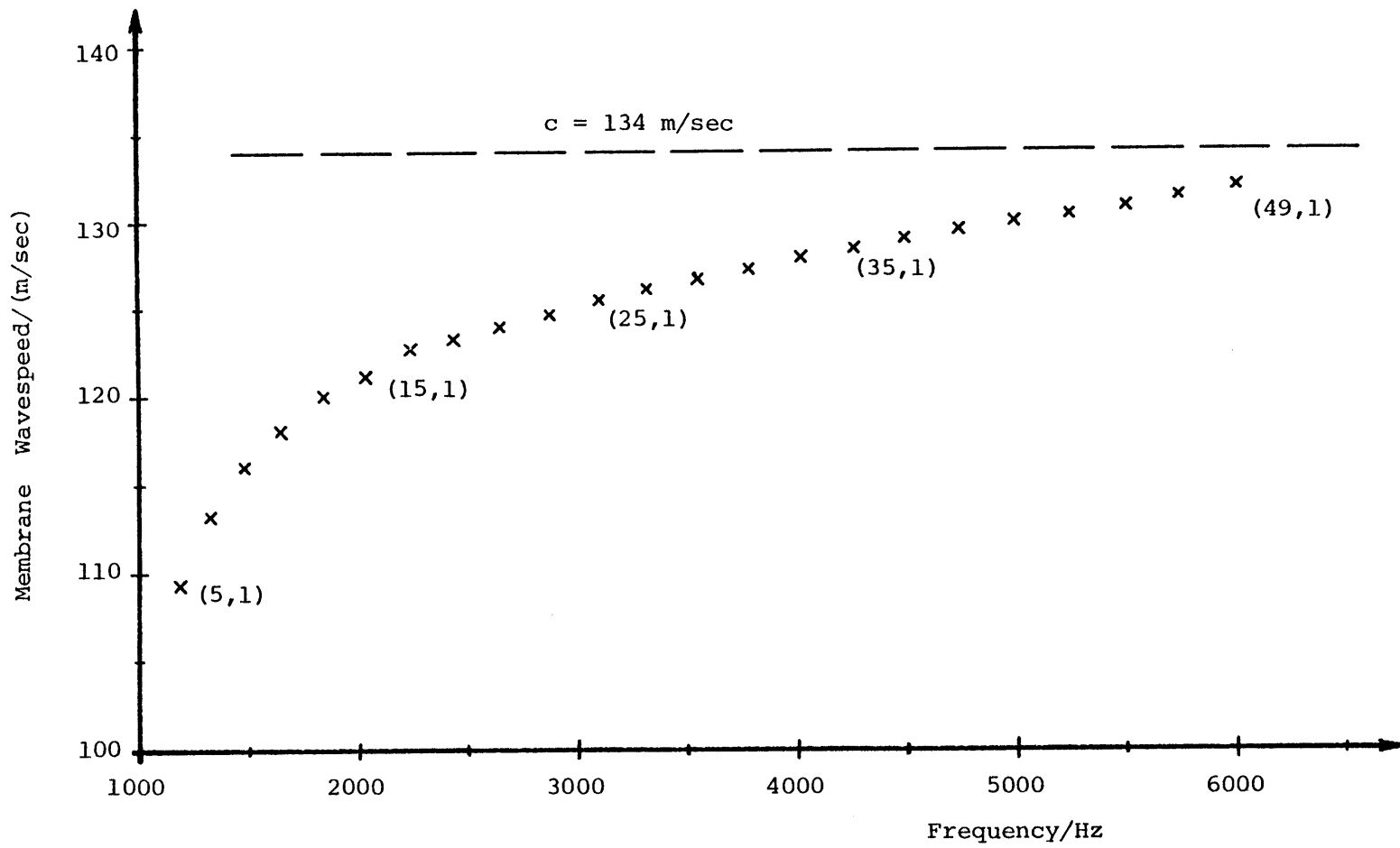


FIGURE 6.1 Membrane Wave Speed Data, Standard Membrane

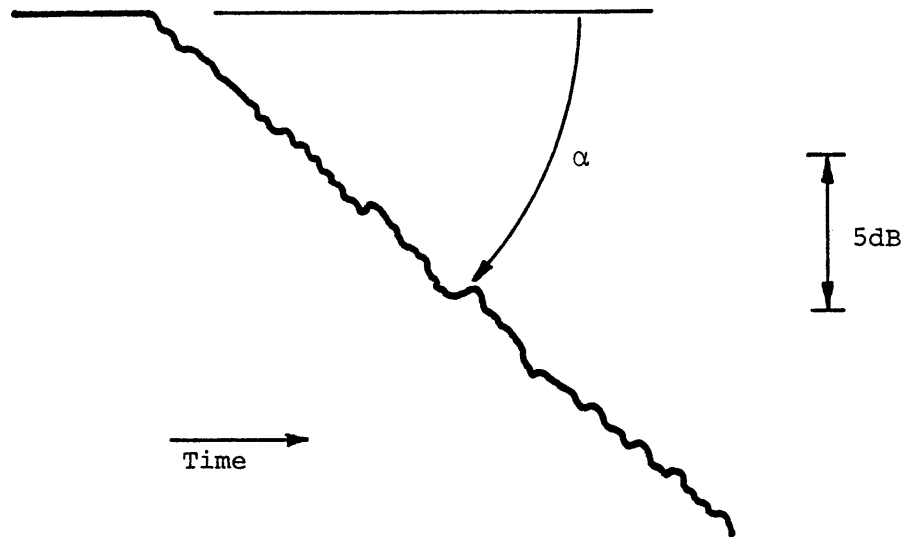
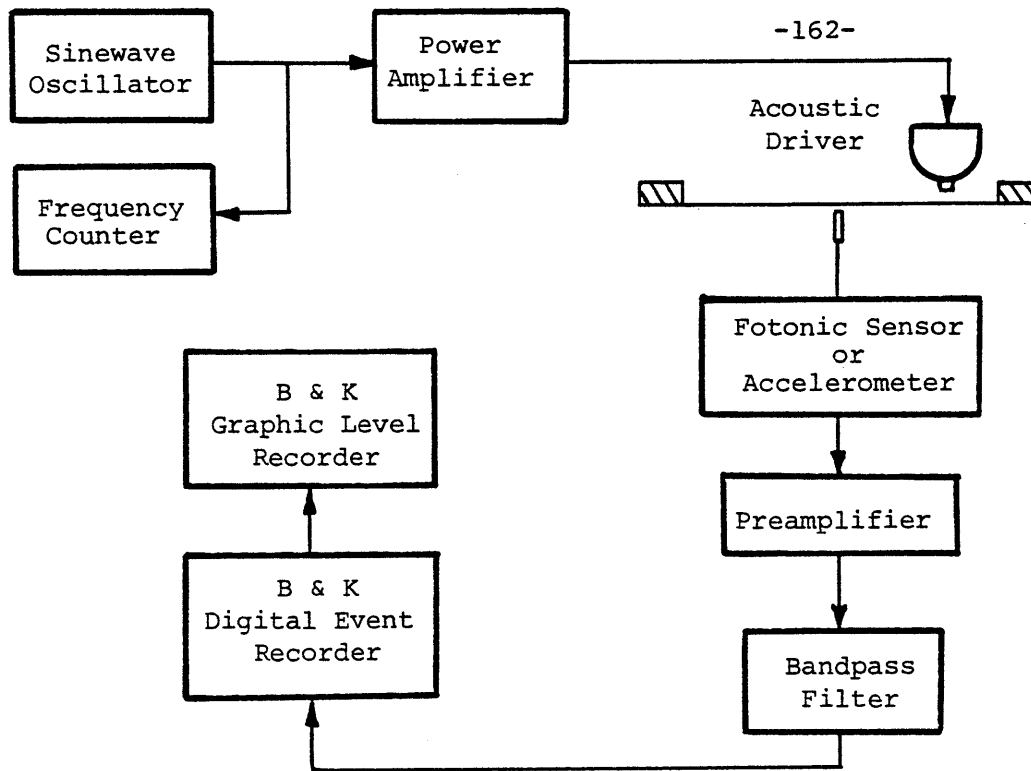


FIGURE 6.2 Experimental Set-Up For Decay Rate Measurements and Typical RMS Decay Record

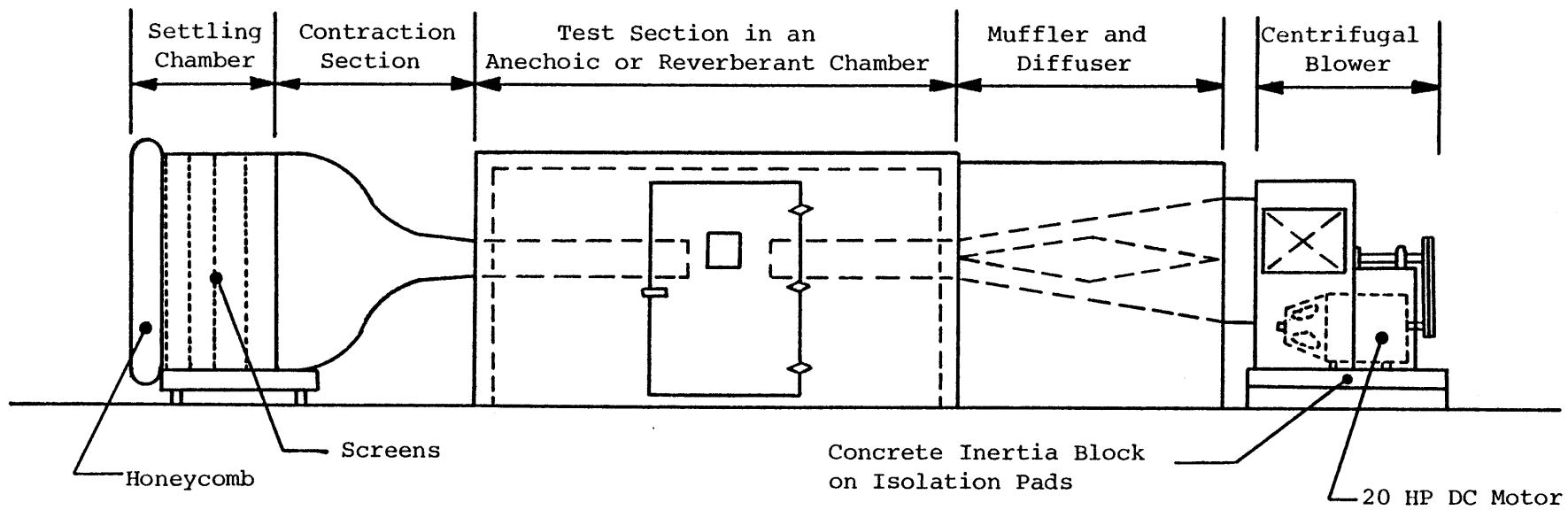


FIGURE 6.3 Low-Noise, Low-Turbulence Wind Tunnel Facility  
 Contraction Ratio, 20:1. Test Section 15" Sq.

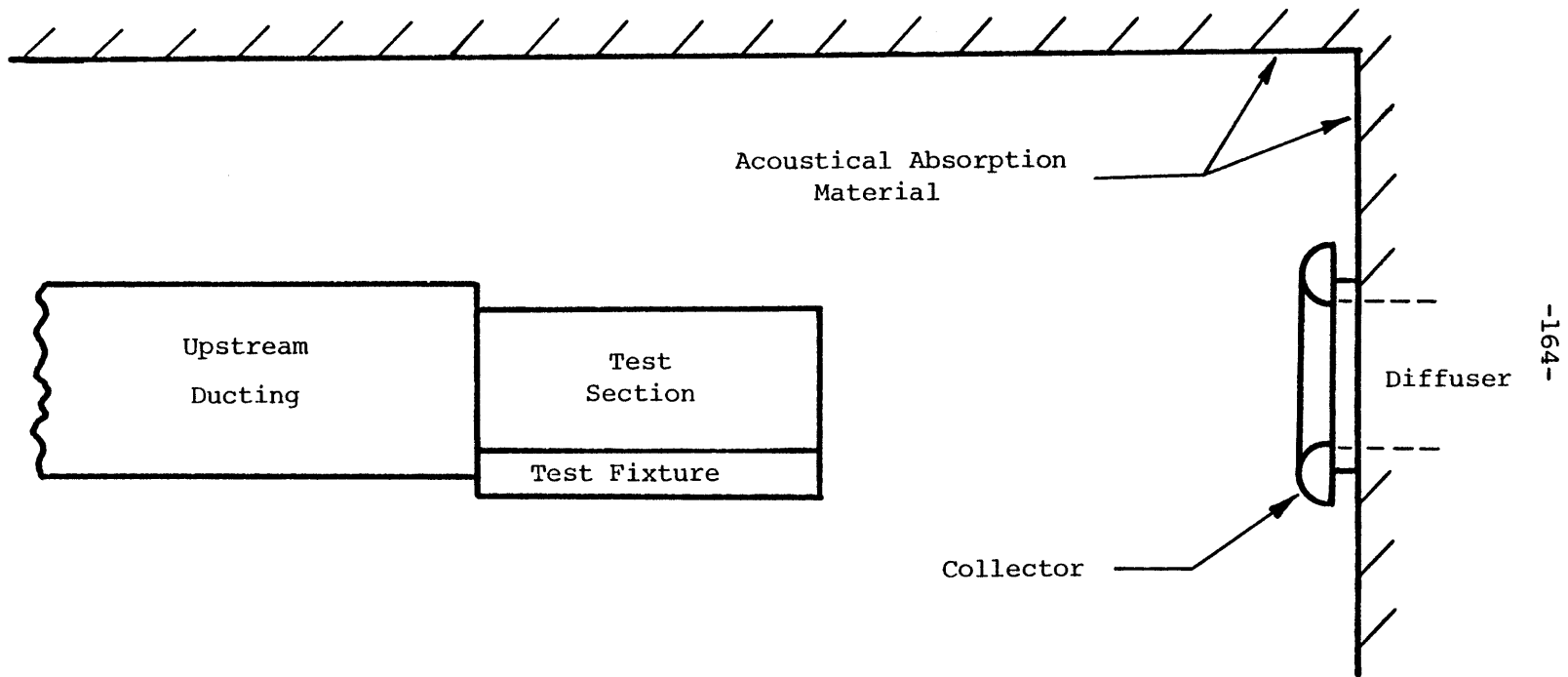


FIGURE 6.4 The Test Section Configuration

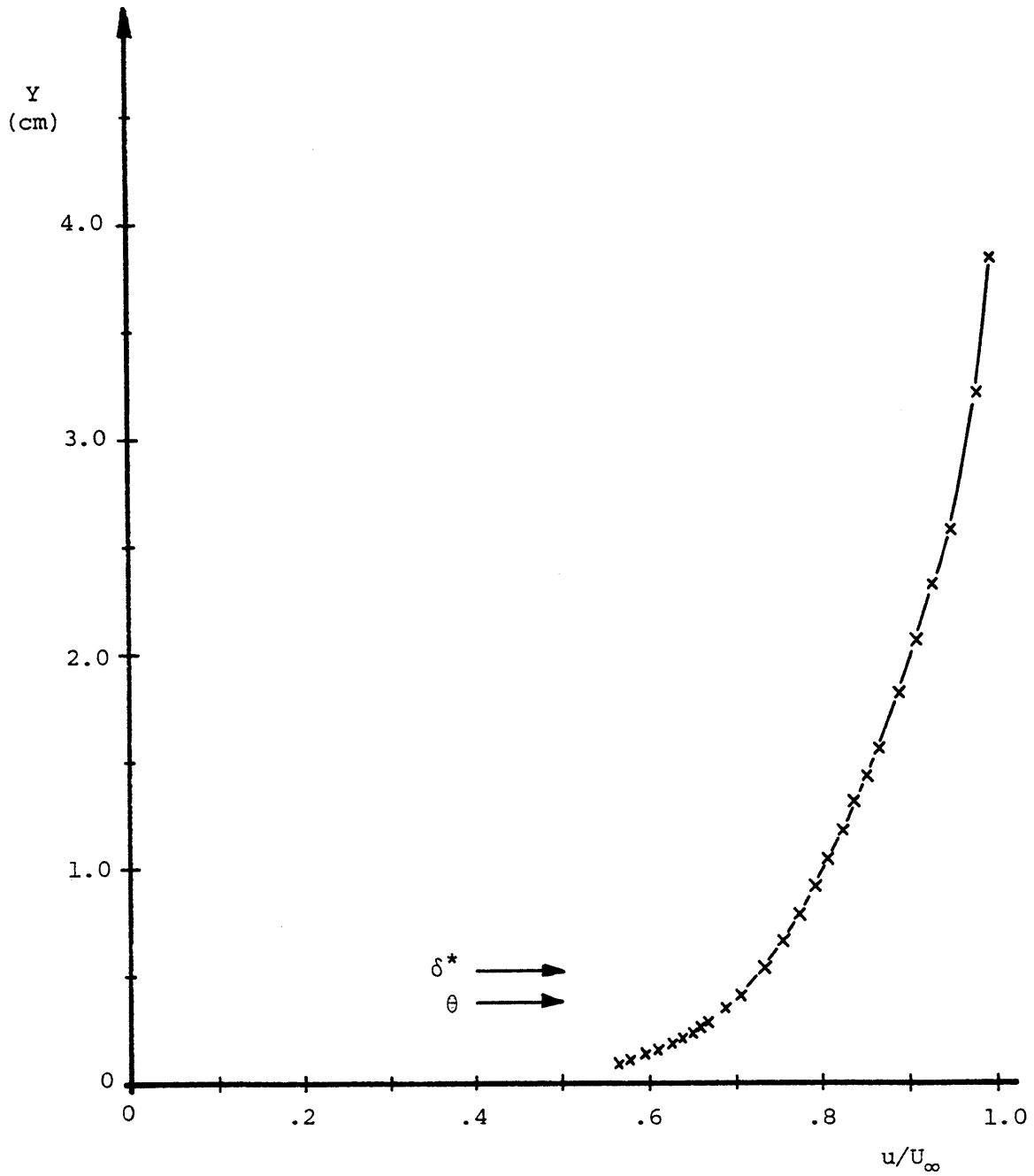


FIGURE 6.5 Typical Mean Velocity Profile,  
 $U_\infty = 29$  m/sec

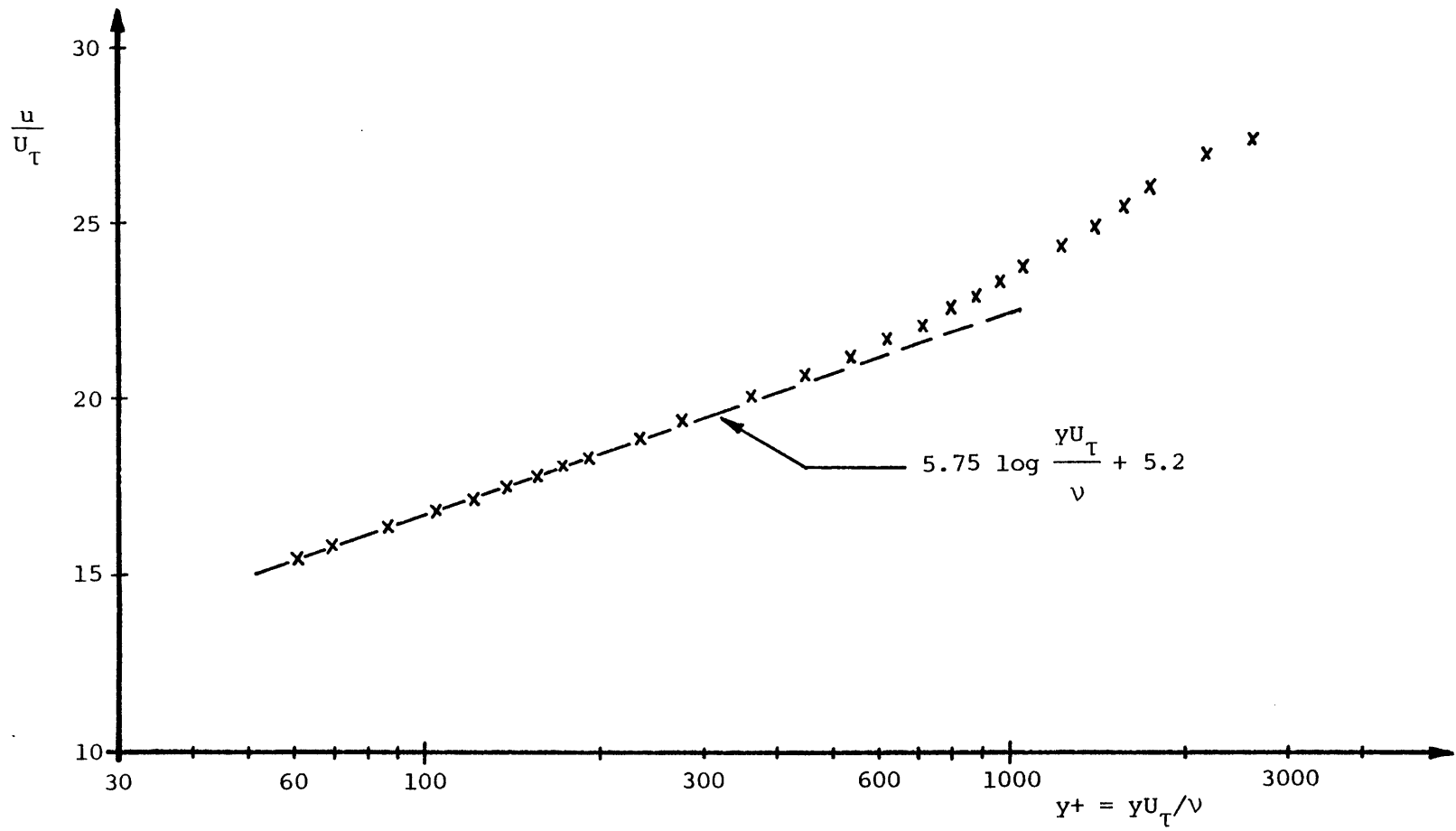


FIGURE 6.6 The Law of the Wall:  $U_\infty = 29$  m/sec

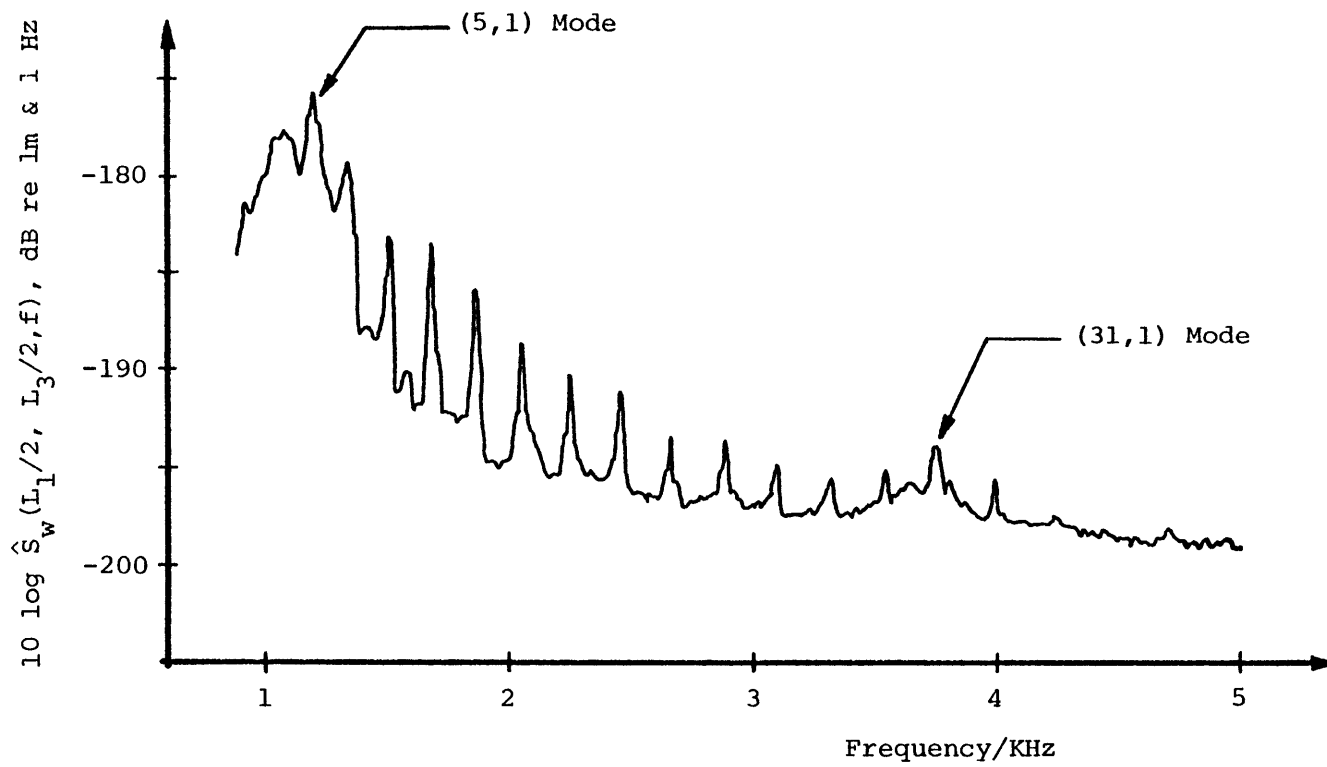


FIGURE 6.7 Standard Membrane Displacement Spectrum,  $U_\infty = 40 \text{ m/sec}$

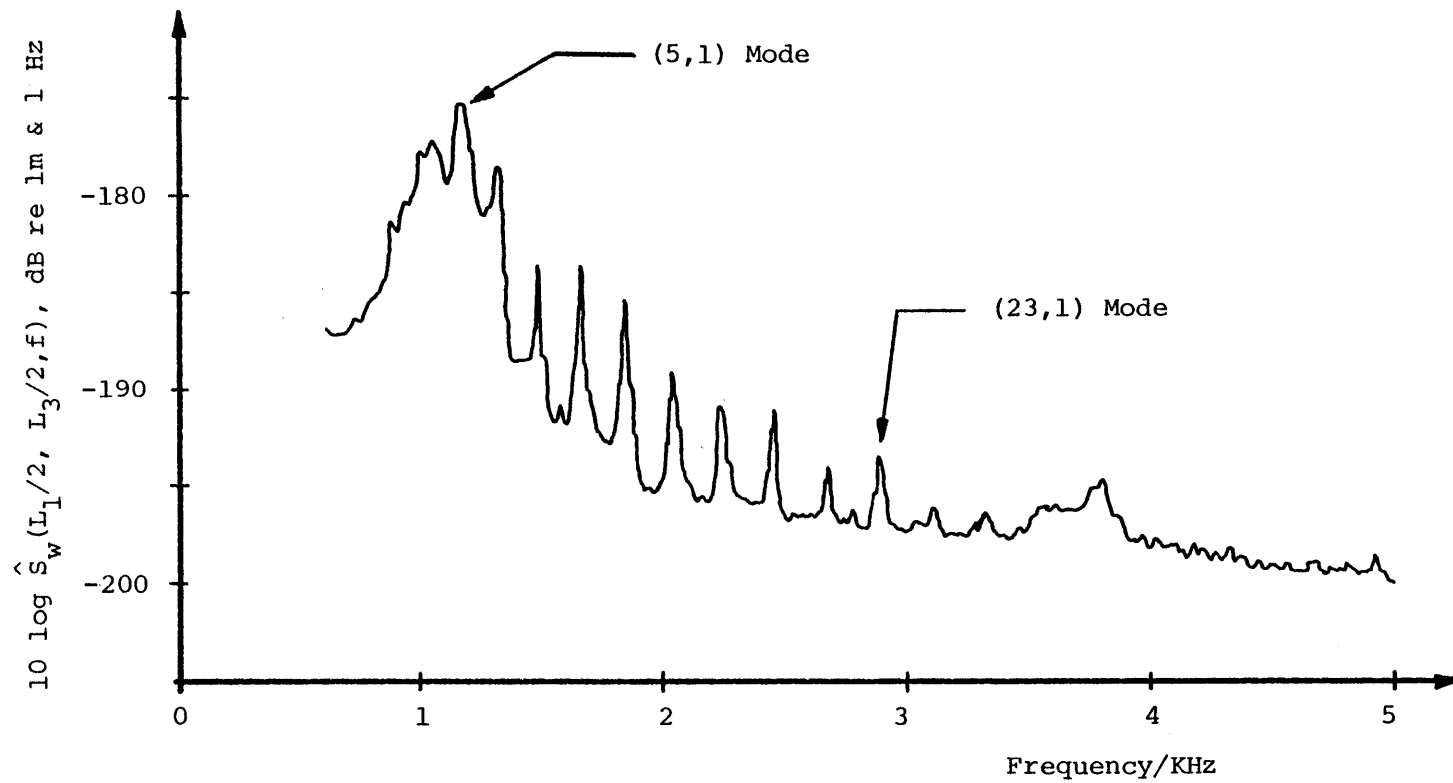


FIGURE 6.8 Modified Membrane Displacement Spectrum,  $U_\infty = 40 \text{ m/sec}$



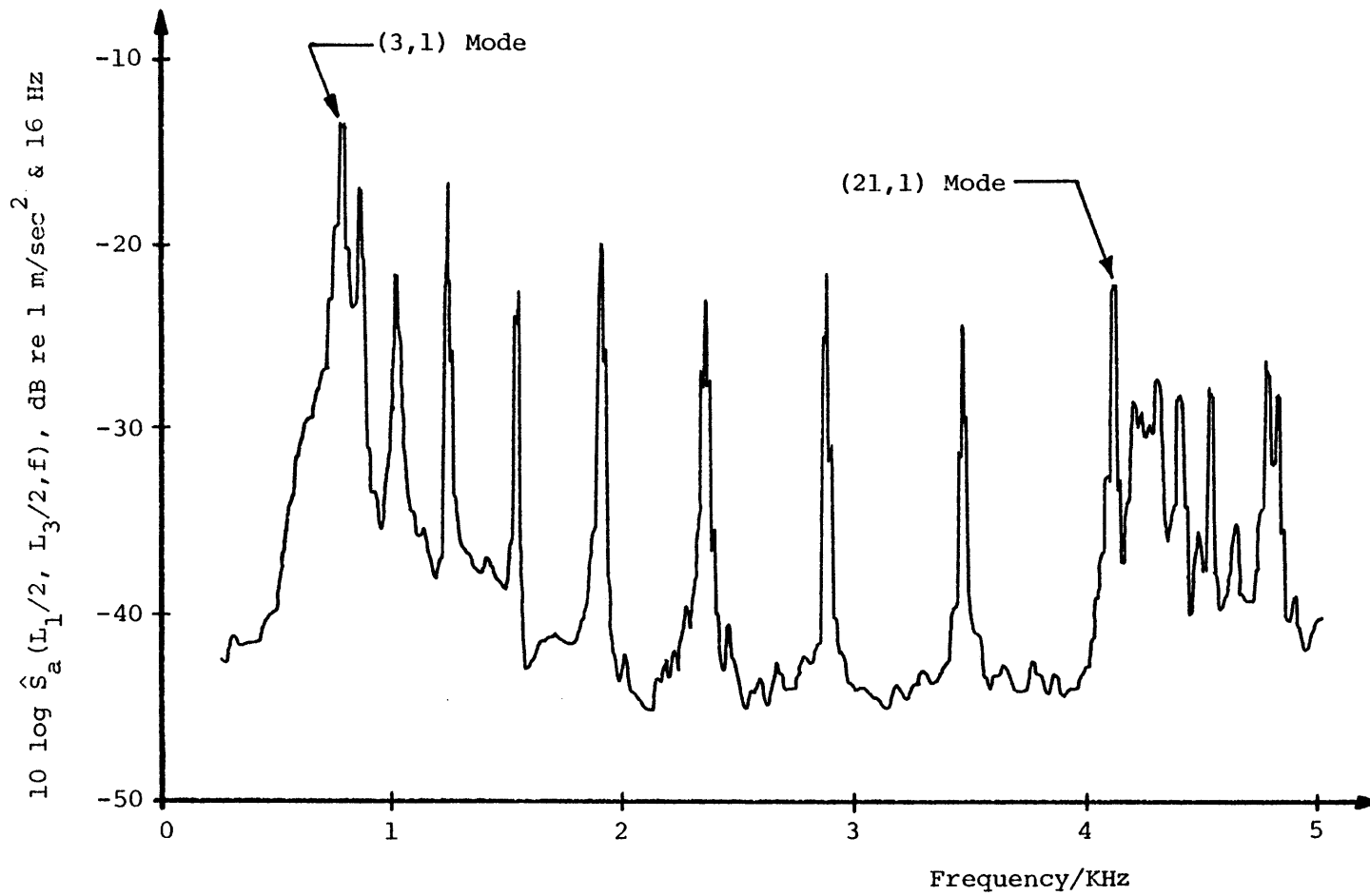


FIGURE 6.9 Clamped Plate Acceleration Spectrum,  $U_\infty = 40 \text{ m/sec}$ ,  
Levels Are Not Corrected For Bandwidth

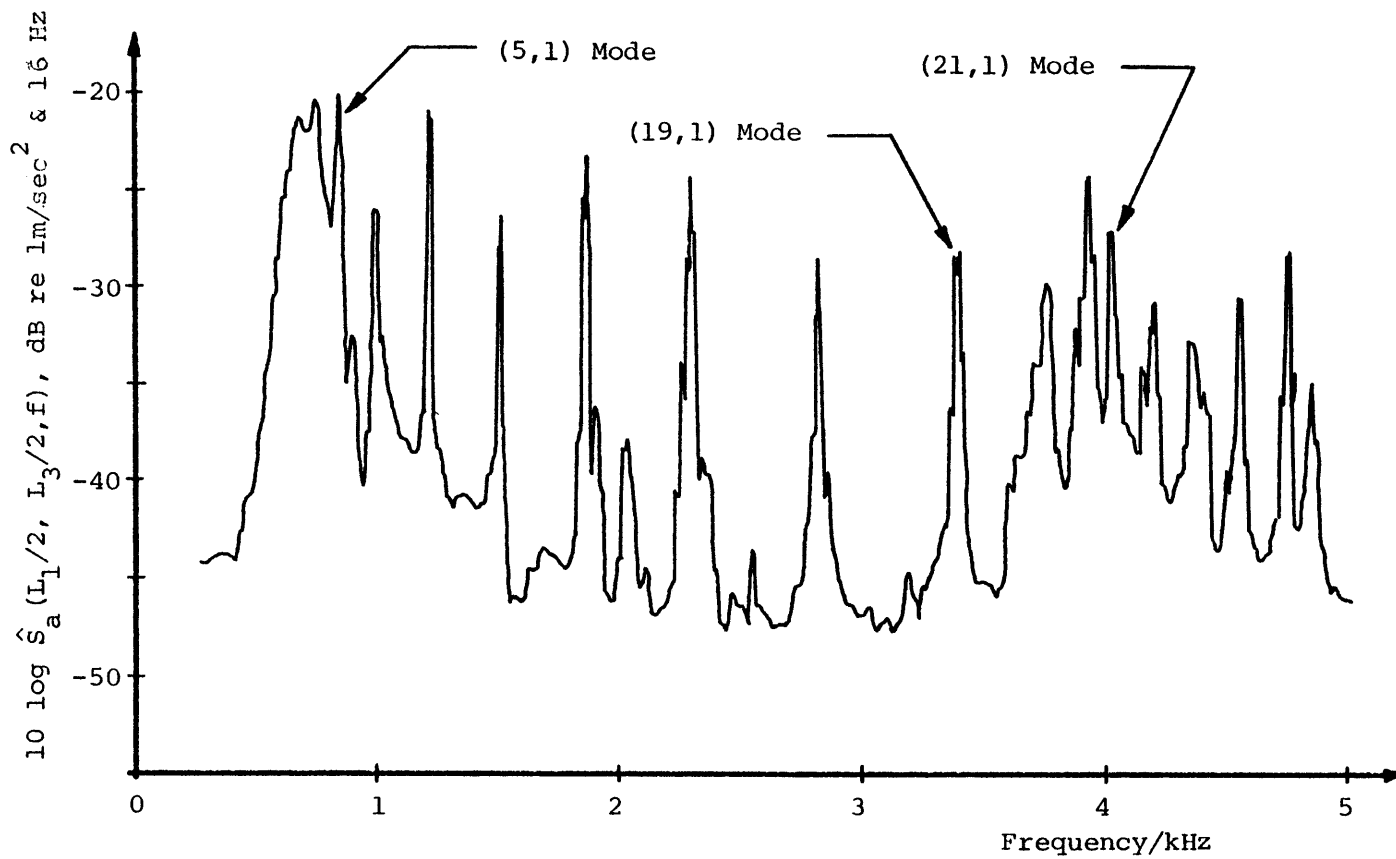


FIGURE 6.10 S-C-S-C Plate Acceleration Spectrum,  $U_{\infty} = 40$  m/sec,  
Levels Are Not Corrected For Bandwidth

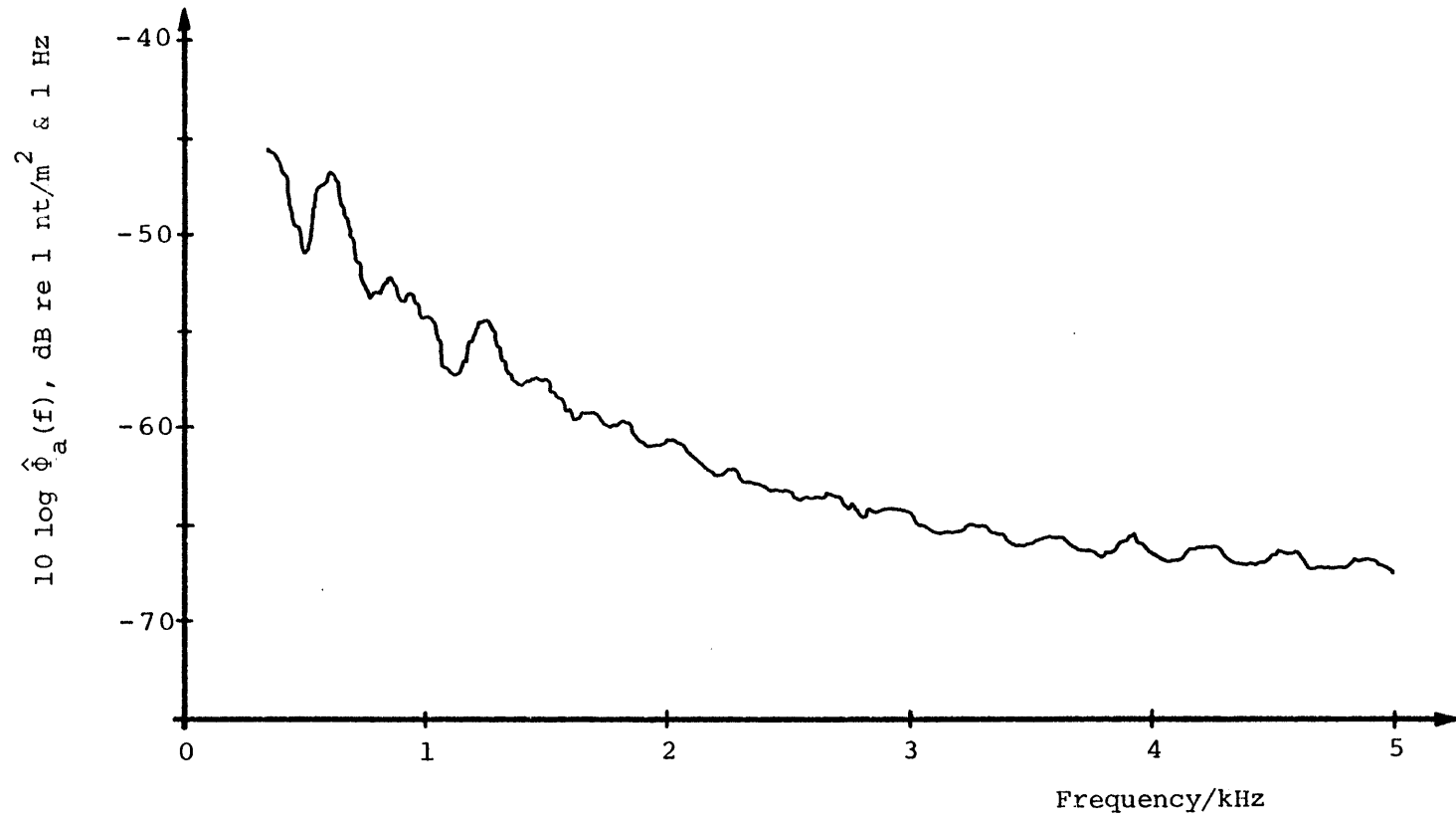


FIGURE 7.1 Typical Acoustic Background Spectrum,  $U_\infty = 40 \text{ m/sec}$

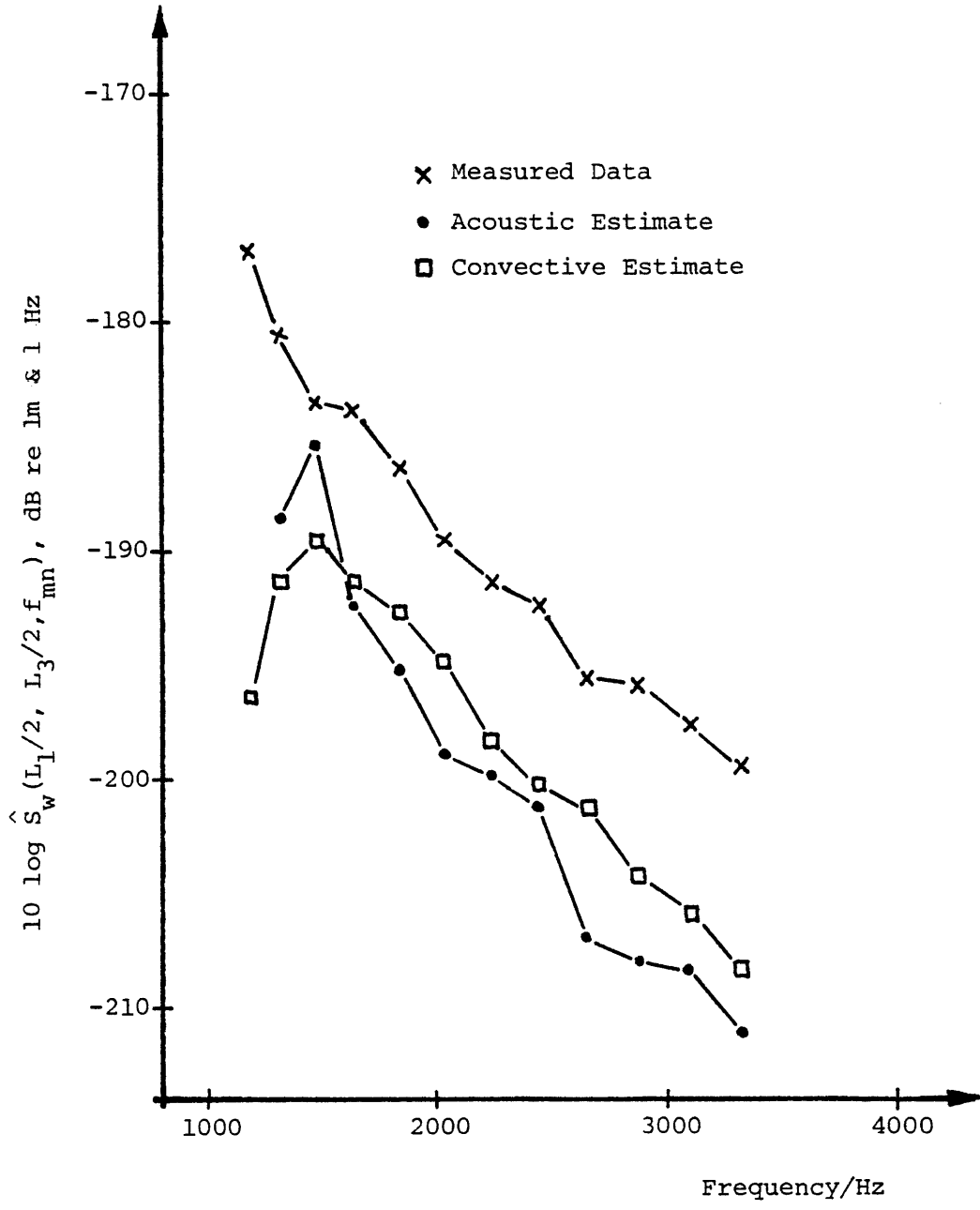


FIGURE 7.2 Comparison of Measured Membrane Response with Predicted Acoustic and Convective Responses, Standard Membrane,  $U_\infty = 40\text{m/sec}$ .

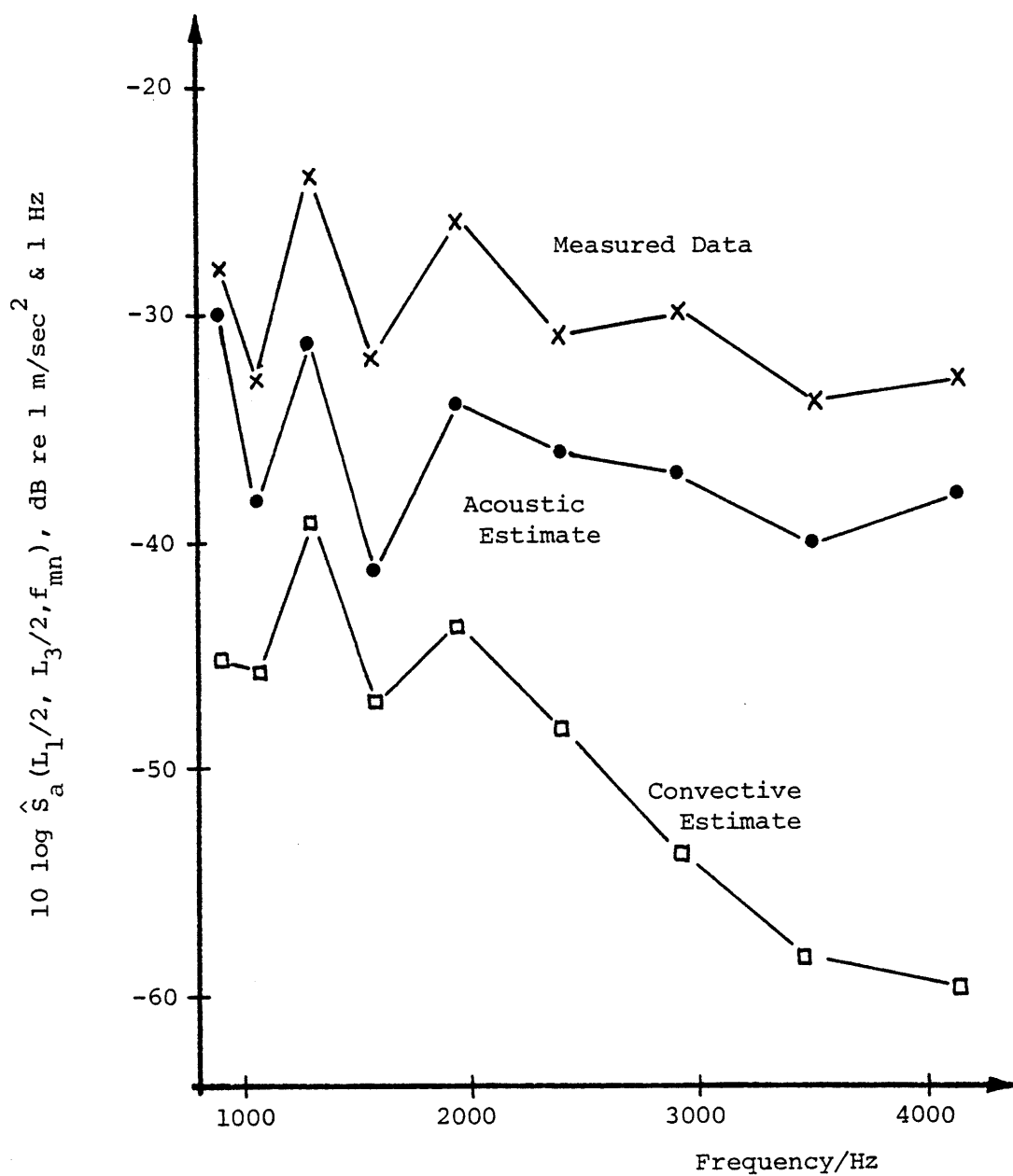


FIGURE 7.3 Comparison of Measured Clamped Plate Response With Predicted Acoustic and Convective Responses,  $U_\infty = 40 \text{ m/sec}$

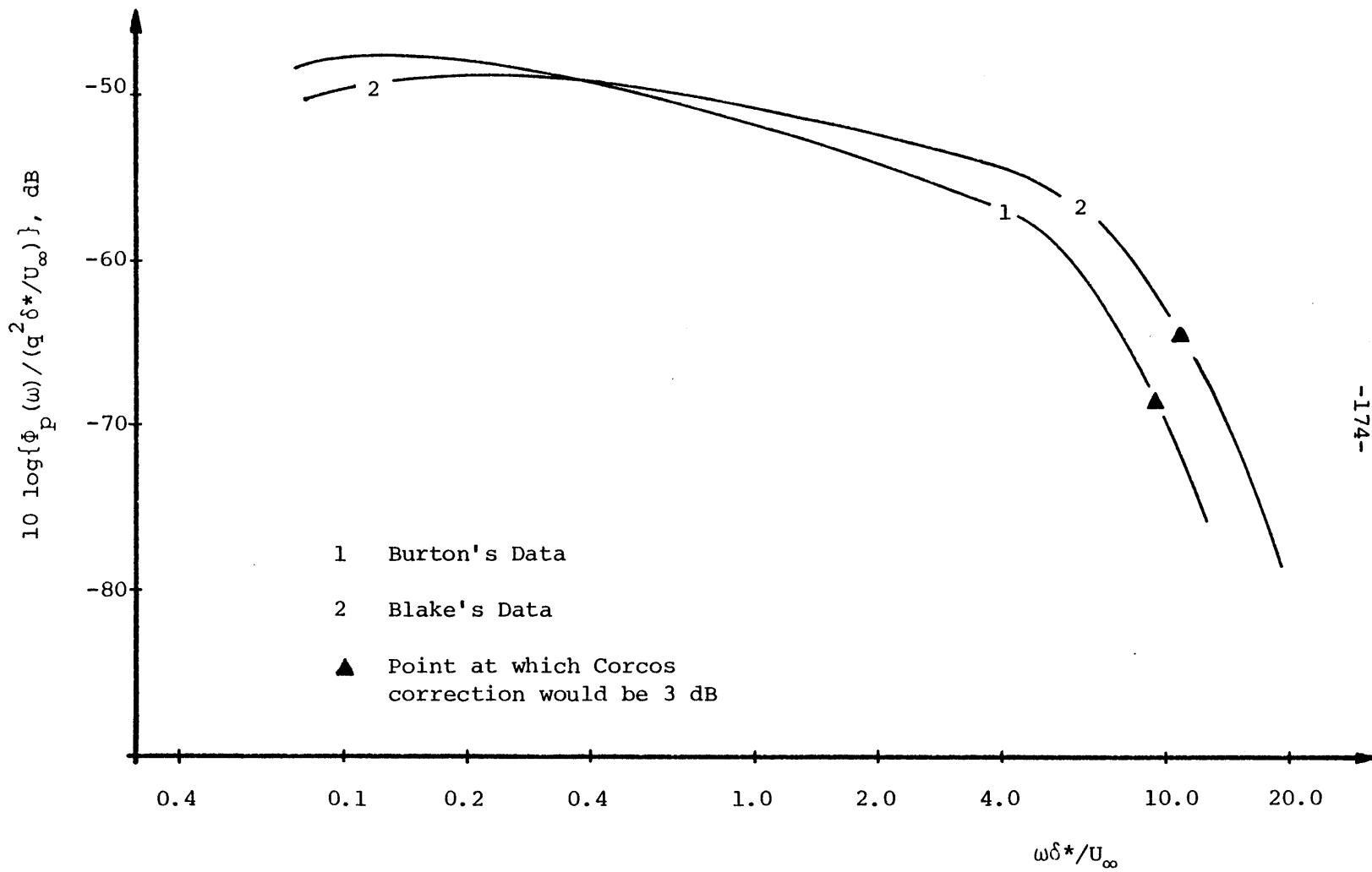


FIGURE 7.4 Wall Pressure Spectra, Data Not Corrected For Transducer Size Effects

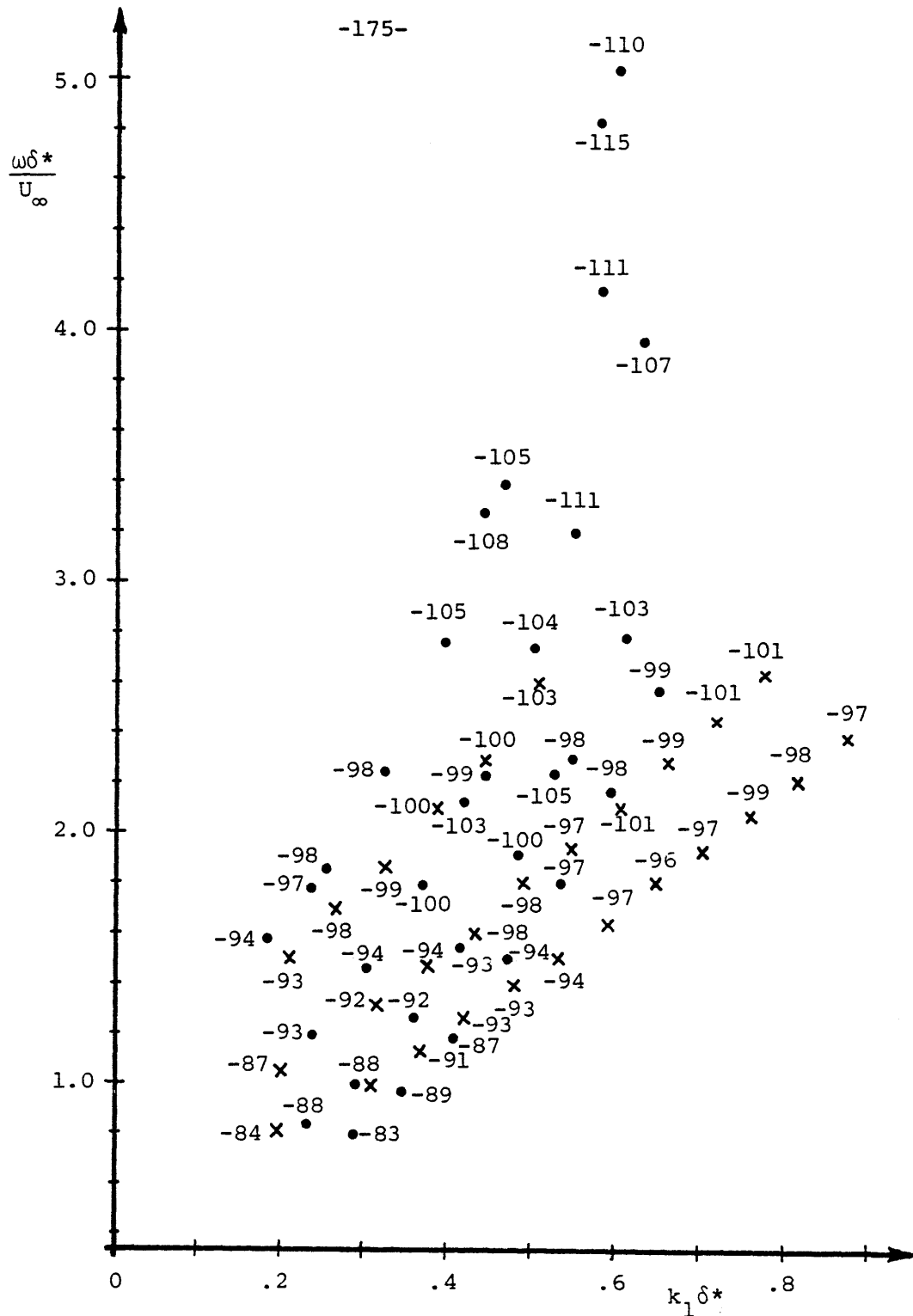


FIGURE 7.5 Location of Low Wavenumber Data in Wavenumber-Frequency Space  
 o-Plate Data, X-Membrane Data, Numbers Indicate Levels of  
 $10 \log\{P(k_1, 0, \omega)/q^2\delta^{*3}/U_\infty\}$ , dB.

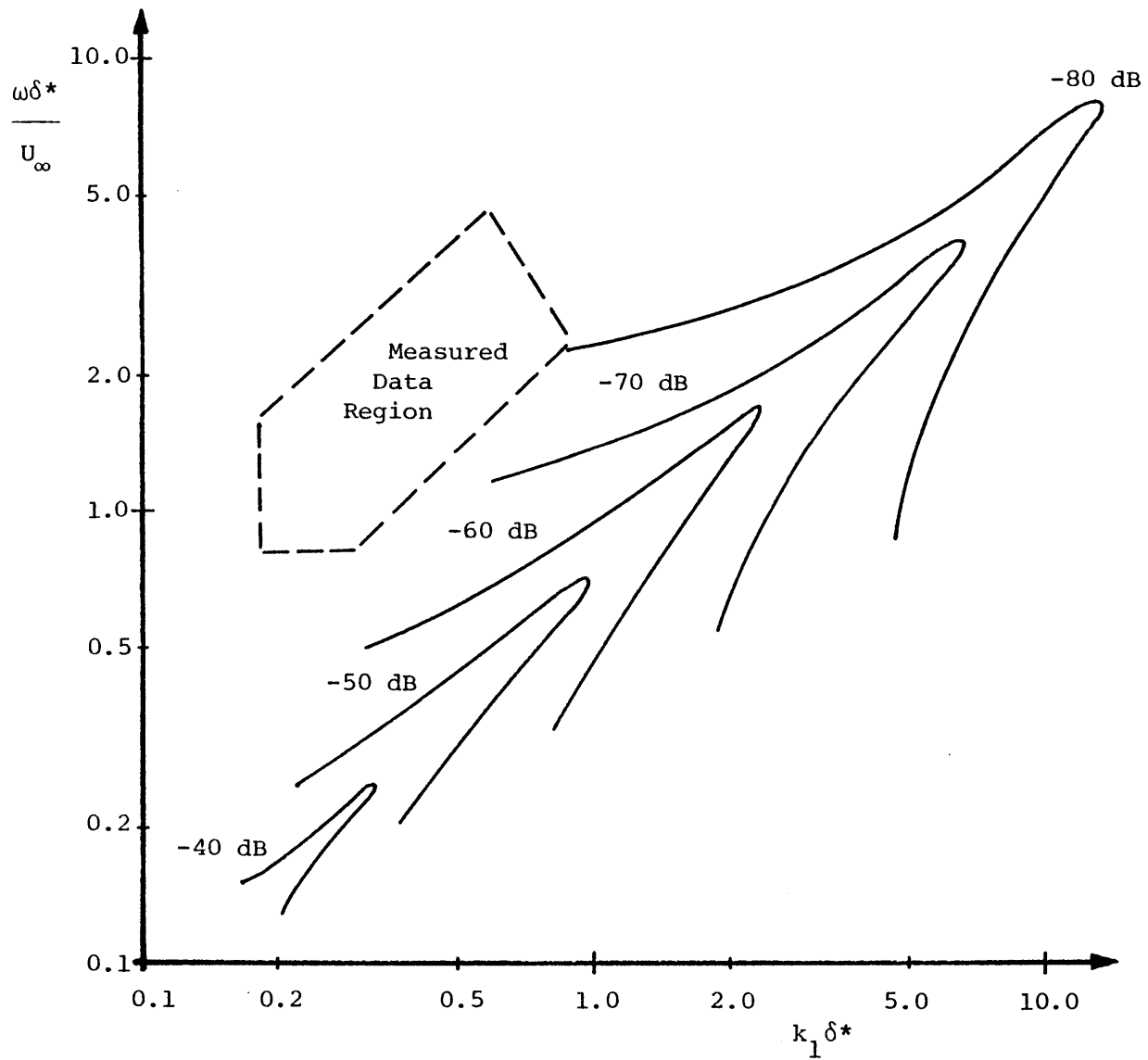


FIGURE 7.6 Contours of  $10 \log \left\{ \frac{\Phi_p(k_1^*, 0, \omega^*)}{(q^2 \delta^{*3} / U_\infty)} \right\}$  Obtained by Transforming Blake's Data



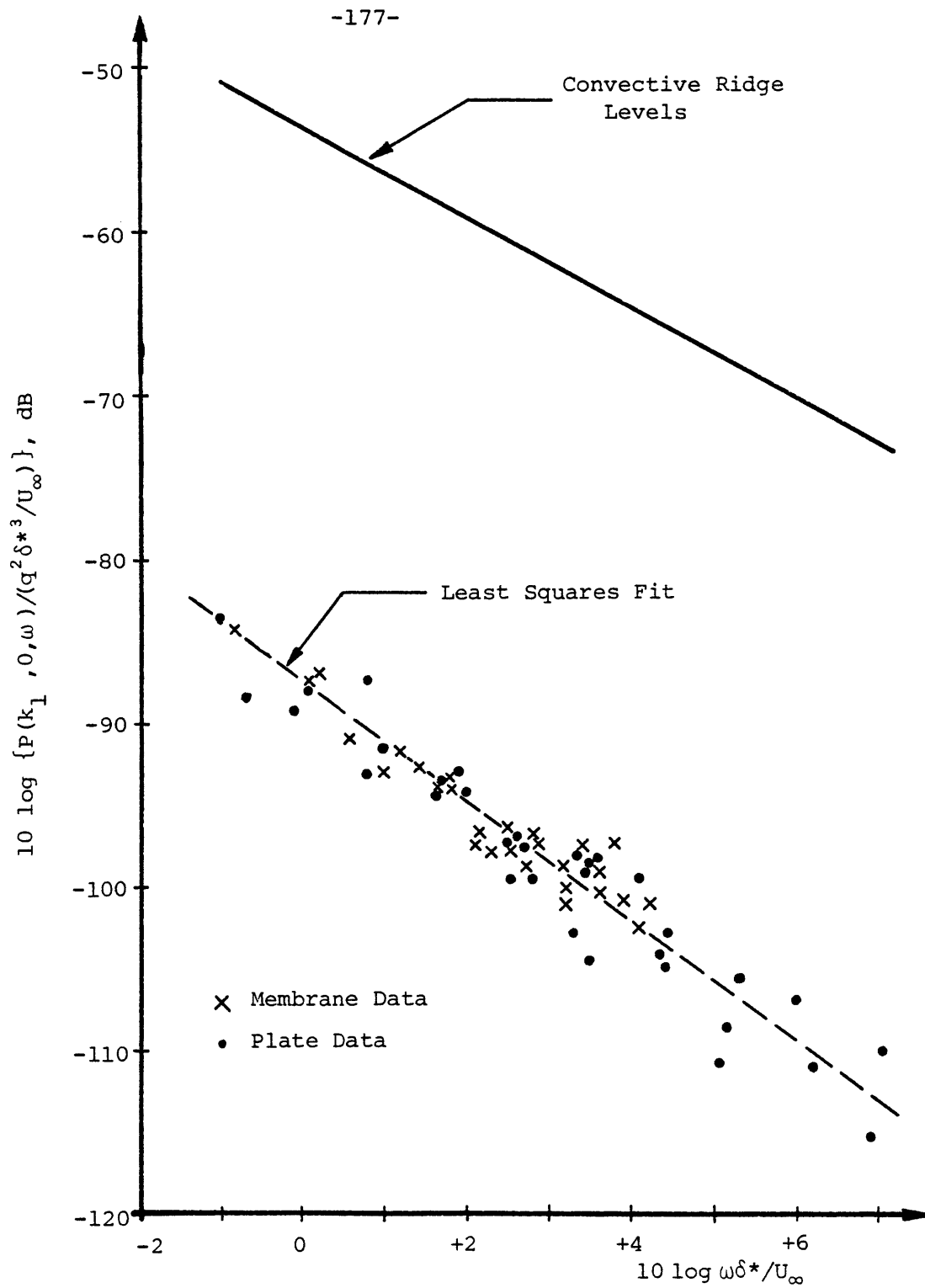


FIGURE 7.7 Comparison of Convective and Measured Low Wavenumber Levels of  $\Phi_p(k_1, 0, \omega)$

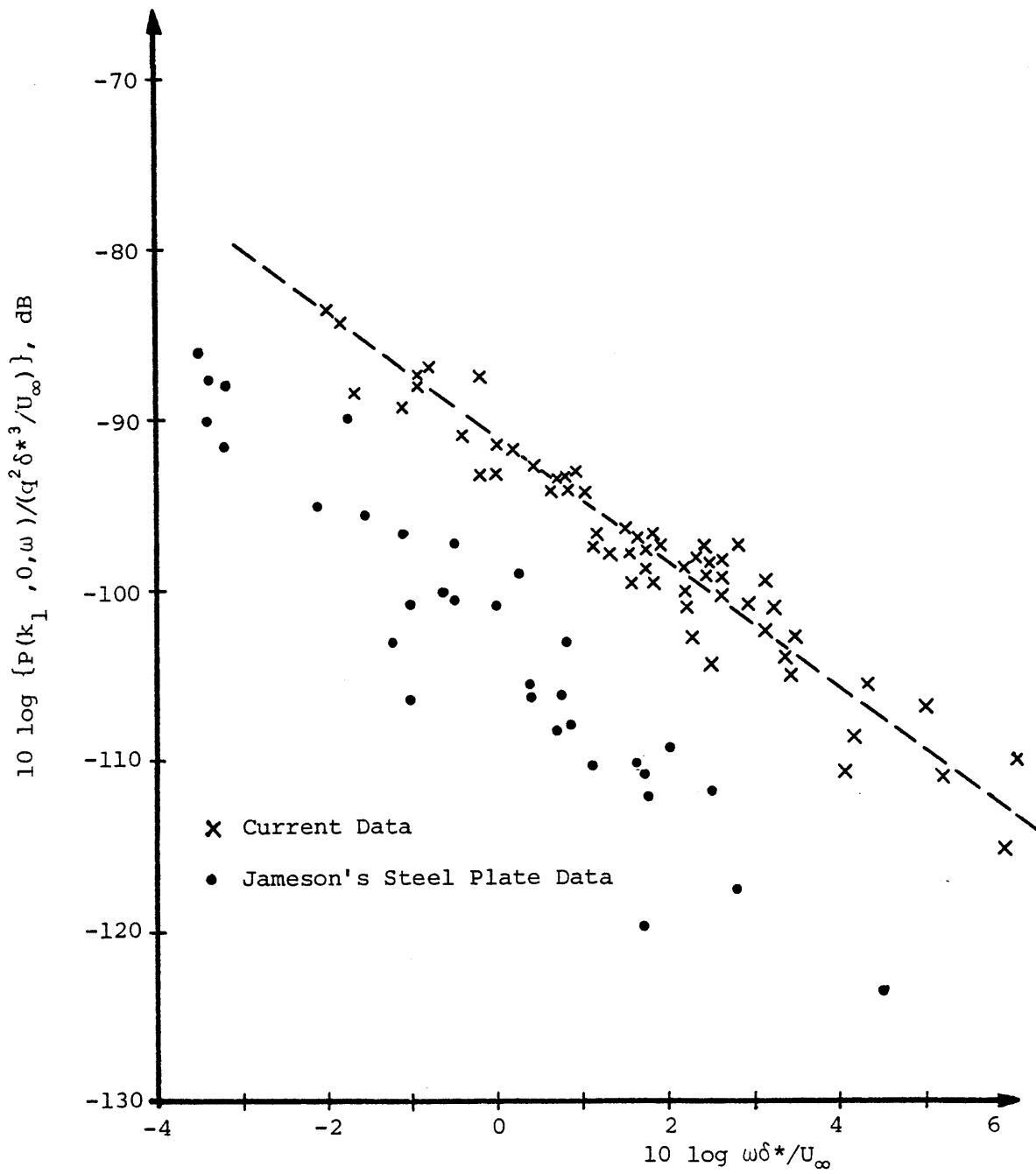


FIGURE 7.8 Comparison of the Measured Low Wavenumber Spectra with Jameson's Data

REFERENCES

1. Blake, W. K., "Turbulent-Boundary-Layer Wall-Pressure Fluctuations on Smooth and Rough Walls", J. Fluid Mech., 44, pp. 637-660, (1970).
2. Burton, T. E., "Wall Pressure Fluctuations at Smooth and Rough Surfaces Under Turbulent Boundary Layers with Favorable and Adverse Pressure Gradients", M.I.T. Acoustics and Vibration Laboratory Report No. 70208-9, (1973).
3. Maidanik, G., and Jorgensen, D. W., "Boundary Wave-Vector Filters for the Study of the Pressure Field in a Turbulent Boundary Layer", J.A.S.A., 42, pp. 494-501, (1967).
4. Blake, W. K., and Chase, D. M., "Wavenumber-Frequency Spectra of Turbulent-Boundary-Layer Pressure Measured by Microphone Arrays", J.A.S.A., 49, pp. 862-877, (1971).
5. Jameson, P. W., "Measurement of Low-Wavenumber Component of Turbulent Boundary Layer Wall Pressure Spectrum", Bolt Beranek and Newman Report No. 1937, (1970).
6. Aupperle, F. A. and Lambert, R. F., "On the Utilization of a Flexible Beam as a Spatial Filter", J. Sound Vib., 24, pp. 259-267, (1972).
7. Aupperle, F. A. and Lambert, R. F., "Acoustic Radiation from Plates Excited by Flow Noise", J. Sound Vib., 26, pp. 223-245, (1973).
8. Jameson, P. W., "Measurement of the Low Wavenumber Component of Turbulent Boundary Layer Pressure Spectral Density", 4th Symposium on Turbulence in Liquids, Univ. of Missouri-Rolla, September 1975, (Proceedings to be published).
9. Chase, D. M., "Turbulent-Boundary-Layer Pressure Fluctuations and Wavenumber Filtering by Nonuniform Spatial Averaging", J.A.S.A., 46, pp. 1350-1365, (1969).
10. Dyer, I., "Sound Radiation Into a Closed Space from Boundary Layer Turbulence", Second Symposium on Naval Hydrodynamics, (1958).
11. Leissa, A. W., "Vibration of Plates", NASA SP-160, (1969).

12. Filon, L. N. G., "On a Quadrature Formula for Trigonometric Integrals", Proc. Roy. Soc. Edinburgh, 49, pp 38-47, (1929).
13. Volterra, E. and Zachmanoglou, E. C., Dynamics of Vibrations, Chas. E. Merrill Books, Inc., Columbus, Ohio, 1965.
14. Bendat, J. S. and Piersol, A. G., Measurement and Analysis of Random Data, Wiley, 1966, Chapter 7.
15. Hoppmann, W. H. and Greenspon, J., "An Experimental Device for Obtaining Elastic Rotational Constraints on the Boundary of a Plate", Proc. 2nd. U.S. Natl. Congr. Appl. Mech., 1954, pp. 187-191.
16. Corcos, G. M., "The Resolution of Turbulent Pressures at the Wall of a Boundary Layer", J. Sound Vib., 6, pp 59-70, (1967).
17. Blake, W. K., "Turbulent Boundary Layer Wall Pressure Fluctuations on Smooth and Rough Walls", M.I.T. Acoustics and Vibration Laboratory Report No. 70208-1, (1969).
18. Wills, J. A. B., "Measurements of the Wavenumber/Phase Velocity Spectrum of Wall Pressure Beneath a Turbulent Boundary Layer", J. Fluid Mech., 45, pp. 65-90, (1971).
19. Hanson, C. E., "The Design and Construction of a Low-Noise Low-Turbulence Wind Tunnel", M.I.T. Acoustics and Vibration Laboratory Report No. 79611-1, (1969).
20. Cramer, H. and Leadbetter, M. R., Stationary and Related Stochastic Processes, Wiley, 1967, Chapter 7.

APPENDIX A

Mode Shapes and Eigenvalues for Beams with Various Boundary Conditions

The mode shapes listed here are normalized according to equation (2.20) and are given in terms of the non-dimensional spatial variables  $\bar{x} = x/L$  and  $\bar{k} = kL$ .

Free-Free Beam

The boundary conditions are  $g_m''(0) = g_m'''(0) = g_m''(1) = g_m'''(1) = 0$ , and the resulting normalized mode shape is

$$G_m(\bar{x}) = \left[ \cosh \bar{k}_m \bar{x} + \cos \bar{k}_m \bar{x} - \frac{(\sinh \bar{k}_m + \sin \bar{k}_m)}{(\cosh \bar{k}_m - \cos \bar{k}_m)} (\sinh \bar{k}_m \bar{x} + \sin \bar{k}_m \bar{x}) \right]. \quad (A1)$$

The eigenvalues  $\bar{k}_m$  are determined by the equation

$$\cosh \bar{k}_m \cos \bar{k}_m = 1, \quad (A2)$$

Volterra [13] lists values of  $\bar{k}_m$  (excluding the two  $\bar{k}_m = 0$  modes) of:

m	$\bar{k}_m$	m	$\bar{k}_m$	m	$\bar{k}_m$
1	4.7300408	3	10.9956078	5	17.2787596
2	7.8532046	4	14.1371655	m 5	$(m + 1/2)\pi$

Clamped-Free Beam

The boundary conditions are  $g_m(0) = g_m'(0) = g_m''(1) = g_m'''(1) = 0$ , and the resulting normalized mode shape is

$$G_m(\bar{x}) = \left[ \cosh \bar{k}_m \bar{x} - \cos \bar{k}_m \bar{x} - \frac{(\cosh \bar{k}_m + \cos \bar{k}_m)}{(\sinh \bar{k}_m + \sin \bar{k}_m)} (\sinh \bar{k}_m \bar{x} - \sin \bar{k}_m \bar{x}) \right] \quad (A3)$$

The eigenvalues are determined from

$$\cosh \bar{k}_m \cdot \cos \bar{k}_m = -1. \quad (A4)$$

For this case Leissa [11] gives values of  $\bar{k}_m$  of:

m	$k_m$	m	$k_m$	m	$k_m$
1	1.8751041	3	7.8547574	5	14.1371684
2	4.6940911	4	10.9955407	m 5	(m - 1/2)π

Simply-Supported Beam

The boundary conditions are  $g_m(0) = g_m''(0) = g_m(1) = g_m''(1) = 0$ , and the resulting normalized mode shape is

$$G_m(\bar{x}) = \sqrt{2} \sin \bar{k}_m \bar{x}, \quad (A5)$$

where the eigenvalues  $\bar{k}_m$  are given by  $\bar{k}_m = m\pi$ ,  $m = 1, 2, 3, \dots$

Clamped-Simple Beam

The boundary conditions are  $g_m(0) = g_m'(0) = g_m(1) = g_m''(1) = 0$ , and the resulting normalized mode shape is

$$G_m(\bar{x}) = \left[ \cosh \bar{k}_m \bar{x} - \cos \bar{k}_m \bar{x} - \frac{1}{\tanh \bar{k}_m} (\sinh \bar{k}_m \bar{x} - \sin \bar{k}_m \bar{x}) \right]. \quad (A6)$$

The eigenvalues  $\bar{k}_m$  are determined by the equation

$$\tanh \bar{k}_m = \tan \bar{k}_m. \quad (A7)$$

Volterra [13] gives the eigenvalues  $\bar{k}_m$  as:

$m$	$\bar{k}_m$	$m$	$\bar{k}_m$	$m$	$\bar{k}_m$
1	3.9266023	3	10.2101761	6	16.4933614
2	7.0685827	4	13.3517688	$m > 5$	$(m + 1/4)\pi$

Clamped-Clamped Beam

The boundary conditions are  $g_m(0) = g'_m(0) = g_m(1) = g'_m(1) = 0$ , and the resulting normalized mode shape is (A8)

$$G_m(\bar{x}) = \left[ \cosh \bar{k}_m \bar{x} - \cos \bar{k}_m \bar{x} - \frac{(\cosh \bar{k}_m - \cos \bar{k}_m)}{(\sinh \bar{k}_m - \sin \bar{k}_m)} (\sinh \bar{k}_m \bar{x} - \sin \bar{k}_m \bar{x}) \right].$$

The determining equation for the eigenvalues  $\bar{k}_m$  is identical with equation (A2) so that the eigenvalues listed for the free-free beam apply to the clamped beam case as well.

APPENDIX B

A Convective Ridge Model of the Wavenumber-Frequency Spectrum of Wall Pressure

There are two reasons for seeking a reliable estimate of the levels of the wavenumber-frequency spectrum of wall pressure  $\Phi_p(\vec{k}, \omega)$  at convective wavenumbers. First, it is helpful to have a reference with which to compare the low wavenumber measurements. Secondly, a convective estimate of  $\Phi_p(\vec{k}, \omega)$  is needed for purposes of estimating the possible degree of convective contamination in the measured response.

Measurements of single point spectra and cross-spectral densities of wall pressure are both dominated by convective effects. It should, therefore, be possible to manipulate such data to obtain an estimate of  $\Phi_p(\vec{k}, \omega)$  which is valid at convective wavenumbers (i.e.:  $k_1 \approx \omega/U_c$ ). Blake [17] had previously obtained two point wall pressure data in the same wind tunnel facility that was used for the low wavenumber measurements. Some of Blake's data was presented in the form of cross-spectral density functions  $\Phi_p(r_1, r_3, \omega)$ . By fitting exponential curves to his cross-spectral density data Blake obtained [17]

$$\begin{aligned}
 1. \quad & \left| \Phi_p(r_1, 0, \omega) \right| \approx \Phi_p(\omega) e^{-0.116(\omega r_1/U_c)}, \\
 2. \quad & \Phi_p(0, r_3, \omega) \approx \Phi_p(\omega) e^{-1.2(\omega r_3/U_\infty)},
 \end{aligned}
 \tag{B1}$$



where  $\Phi_p(\omega)$  is the spectral density of wall pressure.

A similarity form is assumed for  $\Phi_p(r_1, r_3, \omega)$  which differs from that of Corcos [16] only in the argument of the B-function.

That is,

$$\Phi_p(r_1, r_3, \omega) = \Phi_p(\omega) \cdot A \left( \frac{\omega r_1}{U_c} \right) \cdot B \left( \frac{\omega r_3}{U_\infty} \right) \cdot e^{-i\omega r_1 / U_c}. \quad (B2)$$

By using Blake's data from equation (B1), equation (B2) becomes

$$\Phi_p(r_1, r_3, \omega) = \Phi_p(\omega) e^{-.116|\omega r_1|/U_c} e^{-1.2|\omega r_3|/U_\infty} e^{-i\omega r_1 / U_c}. \quad (B3)$$

The wavenumber-frequency spectrum  $\Phi_p(\vec{k}, \omega)$  is related to the cross-spectral density  $\Phi_p(\vec{r}, \omega)$  by the following transform relationship:

$$\Phi_p(k_1, k_3, \omega) = \frac{1}{(2\pi)^2} \iint_{-\infty}^{\infty} \Phi_p(r_1, r_3, \omega) e^{i(k_1 r_1 + k_3 r_3)} dr_1 dr_3. \quad (B4)$$

If the similarity form of equation (B3) is substituted into equation (B4), the required integrations can be performed analytically to yield

$$\Phi_p(k_1, k_3, \omega) = \Phi_p(\omega) \left\{ \frac{.139 \omega^2 / \pi^2 U_c U_\infty}{\left[ \left( \frac{1.2\omega}{U_\infty} \right)^2 + k_3^2 \right] \left[ \left( \frac{.116\omega}{U_c} \right)^2 + \left( k_1 - \frac{\omega}{U_c} \right)^2 \right]} \right\} \quad (B5)$$

The form of equation (B5) indicates that  $\Phi_p(k_1, k_3, \omega)$  has its largest values at  $(k_3 = 0, k_1 = \omega/U_c)$  thus exhibiting a convective ridge.

Equation (B5) can be non-dimensionalized on outer variables to obtain

$$\Phi'_P(k_1^*, k_3^*, \omega^*) = \Phi'_P(\omega^*) \frac{.139 \alpha \omega^{*2} / \pi^2}{[(1.2\omega^*)^2 + k_3^{*2}] [(.116\omega^*)^2 + (\alpha k_1^* - \omega^*)^2]} \quad (B6)$$

where the non-dimensional variables are defined by

$$\omega^* = \omega \delta^* / U_\infty, \quad \alpha = \alpha(\omega^*) = U_c(\omega^*) / U_\infty, \quad k_i^* = k_i \delta^* \text{ for } i = 1, 3 \quad (B7)$$

$$\Phi'_P(\omega^*) = \Phi_P(\omega) / (q^2 \delta^* / U_\infty), \quad \Phi'_P(k_1^*, k_3^*, \omega^*) = \Phi_P(k_1, k_3, \omega) / (q^2 \delta^{*3} / U_\infty).$$

To obtain convective ridge values for comparison with the measured low wavenumber levels, equation (B6) is used with  $k_3^* = 0$  and  $k_1^* = \omega^* / \alpha$  to give

$$\Phi'_P(k_1^* = \omega^* / \alpha, 0, \omega^*) = \frac{.728\alpha}{\omega^{*2}} \Phi'_P(\omega^*). \quad (B8)$$

-187-  
BIOGRAPHICAL NOTES

The author was born on January 8, 1945 and was raised in Anderson, Indiana. He received his undergraduate education at General Motors Institute in Flint, Michigan where he majored in electrical engineering. While enrolled in this cooperative engineering education program from 1963 to 1967 he was sponsored by Delco-Remy Division, G.M.C., and his work assignments were with that division. In 1967 he came to M.I.T. on a General Motors Fellowship in conjunction with the Bachelor-Masters program at G.M.I. While at M.I.T. he studied applied mechanics in the Mechanical Engineering Department, and his masters thesis under Professor Stephen H. Crandall was concerned with fatigue failure due to random vibration. After receiving the Master of Science Degree in February, 1969, he was awarded the Bachelor of Electrical Engineering Degree by G.M.I. in July 1969. From 1969 through 1972 the author was employed by Delco-Remy Division, G.M.C. first as an instrumentation engineer and then as a senior research engineer in the Advanced Engineering Department. In January 1973 he reentered M.I.T. to work on his Ph.D. in Mechanical Engineering. During this period he was employed as a research assistant for Professor Patrick Leehey.